

-

DIRECTED ENERGY DEPOSITION PROCESSING OF ALPHA-BETA, NEAR-
ALPHA, AND BETA TITANIUM ALLOYS

by

Nicholas Gosse

Submitted in partial fulfilment of the requirements
for the degree of Master of Applied Science

at

Dalhousie University
Halifax, Nova Scotia
May 2022

© Copyright by Nicholas Gosse, 2022

TABLE OF CONTENTS

TABLE OF CONTENTS	ii
LIST OF TABLES	iv
LIST OF FIGURES	v
Acknowledgements	ix
1 INTRODUCTION	1
1.1 Laser Technology and Applications.....	1
1.1.1 <i>Rapid Solidification</i>	3
1.1.2 <i>Laser Welding</i>	4
1.1.3 <i>Laser Cladding</i>	10
1.2 Additive Manufacturing	11
1.2.1 <i>Directed Energy Deposition</i>	12
1.2.2 <i>Laser Powder-Fed DED Equipment</i>	14
1.2.3 <i>Process Concerns</i>	18
1.2.4 <i>Influence of Process Parameters</i>	19
1.3 Titanium Alloys and Titanium DED	25
1.3.1 <i>Classification and Properties of Titanium Alloys</i>	27
1.3.2 <i>Titanium Alloys in AM</i>	34
2 RESEARCH OBJECTIVE	39
3 INTER-VENDOR STUDY OF DIRECTED ENERGY DEPOSITION BUILD QUALITY USING A COMMERCIAL TI-64 POWDER	40
3.1 Introduction	41
3.2 Materials and Methodology.....	42
3.3 Results and Discussion	47
3.3.1 <i>Dimensional Accuracy</i>	47
3.3.2 <i>Density and Hardness</i>	51
3.3.3 <i>Microstructure</i>	52
3.3.4 <i>Differential Scanning Calorimetry</i>	57
3.4 Conclusions.....	59
Acknowledgements.....	60
4 DIRECTED ENERGY DEPOSITION PROCESSING OF NEAR-ALPHA AND BETA TITANIUM ALLOYS TI-6242 AND BETA-21S	61
4.1 Introduction	62

4.2	Materials and Methodology	64
4.2.1	Materials.....	64
4.3	Methodology.....	68
4.3.1	DED Processing	68
4.3.2	Statistical Investigation of DED Processing Parameters.....	69
4.3.3	Material Characterization.....	70
4.4	Results and Discussion	72
4.4.1	Beta 21s.....	72
4.4.2	Ti-6242	87
4.4.3	DED Processing of Ti-6242 vs. Beta-21s.....	98
4.5	Conclusions.....	99
4.6	Acknowledgements	99
5	SUMMARY AND CONCLUSIONS	100
5.1	Inter-vendor variation of DED processed Ti-64.....	100
5.2	Feasibility of Ti-6242 and Beta-21s for DED processing	101
5.3	Future Works	102
	REFERENCES	104

LIST OF TABLES

Table 1: Flow rate and apparent density of starting Ti-64 powder.....	42
Table 2: Impurity contents of the starting Ti-64 powder.....	43
Table 3: Measured concentrations of alloying elements and impurities in the starting Ti-64 powder.....	43
Table 4: Average hardness from tensile bars fabricated by each vendor	51
Table 5: Average density from tensile bars fabricated by each vendor.....	52
Table 6: Assays for the raw powders utilized relative to wrought specifications (weight %)......	66
Table 7: Trace impurity analyses of raw powders (weight %).	67
Table 8: Apparent density and hall flow rate.....	67
Table 9: Average particle diameters (D10, D50 and D90) for Ti-6242 and Beta-21s.....	68
Table 10: Process parameter ranges utilized in the development of DOE1.	70
Table 11: Process parameter ranges utilized in the development of DOE2.	70
Table 12: Heat treatments applied to DED specimen.	72
Table 13: Tensile properties of Beta 21S bars fabricated in accordance with high density build parameters (DOE2) and select post-build heat treatments. Typical data for the wrought counterpart shown for comparison purposes [134-136]......	86
Table 14: Tensile properties of Ti-6242 bars fabricated in accordance with high density build parameters (DOE2) and select post-build heat treatments. Typical data for wrought counterpart shown for comparison purposes [138, 139].....	96

LIST OF FIGURES

Figure 1: Graphical representation of photon emission phenomena [3].....	1
Figure 2: Power output of CW vs. PW laser [12].....	3
Figure 3: Basic laser welding apparatus of a butt joint [14].....	5
Figure 4: Weld pool depth of a variety of welding processes [17].....	6
Figure 5: CO ₂ laser welding apparatus [17].....	7
Figure 6: Nd: YAG laser welding apparatus [17].....	8
Figure 7: Conduction welding melt pool diagram [21].	9
Figure 8: Keyhole generation in laser welding [22]	9
Figure 9: Laser cladding apparatus [23]	10
Figure 10: Comparison of common DED thermal energy sources [35]	13
Figure 11: Trunnion capable of 5-axis movement [37].	14
Figure 12: (a) Individual powder feeder and (b) Auger feed system.....	15
Figure 13: Deposition head components [42].....	16
Figure 14: Glovebox and Antechamber.....	17
Figure 15: Gas-induced pore.....	18
Figure 16: Process-induced pore.....	19
Figure 17: Various Scan Strategies (a) single track one-way, (b) single track zigzag, (c) bi-directional and (d) inward spiral [51].....	21
Figure 18: Closed atmosphere DED unit [56]	23
Figure 19: Open atmosphere DED unit [57].....	24
Figure 20: Hall Flow Meter [60].....	25
Figure 21: Simplified diagrams of common crystal lattices [64]	26
Figure 22: Common titanium alloys on a pseudobinary phase diagram indicating dominant phase throughout range of temperatures [65].	28
Figure 23: (a) Equiaxed alpha, (b) equiaxed alpha+beta, (c) acicular alpha+beta) and (d) equiaxed beta microstructures [66]......	29
Figure 24: (a) Acicular alpha, (b) equiaxed alpha and intergranular beta, and (c) fine alpha-beta structure [66].	30
Figure 25: Microstructural possibilities in a alpha-beta titanium alloy. (b) acicular α with prior β grain boundaries, (c) martensitic α' matrix with β and prior β grains, (d) grains of primary α in matrix of transformed β containing acicular α (e) equiaxed primary α in a matrix of martensitic α' [66].....	31

Figure 26: Formation of Widmannstätten microstructure upon rapid cooling from above the beta-transus temperature [68].....	32
Figure 27: Traditional cylindrical stock (left) compared to near-net-shape additively manufactured stock (right) and the resultant machined part (center) [78].....	35
Figure 28: Spinal implant combining solid and porous structures, imitating calceous bone [80].....	36
Figure 29: (a) original, (b) damaged, and (c) repaired turbine blade [92]	36
Figure 30: Deposited near-net-shape stock (left) and final machined part (right) [93]....	37
Figure 31: Additively manufactured titanium implant (left) and render of placement (right) [95].....	38
Figure 32: (a) Particle Size Distribution and (b) Powder Morphology of the as-received Ti-64 powder.....	44
Figure 33: 3D model distributed to vendors consisting of test geometry and tensile specimens.....	44
Figure 34: As-received builds produced by vendor A, B and C.....	45
Figure 35: Difference in angle from 3D model, the black bar indicates the desired angle	48
Figure 36: Comparison of angled column 4 for (a) Vendor A, (b) Vendor B, and (c) Vendor C.....	48
Figure 37: Thickness of Rings (% difference from CAD model).....	49
Figure 38: Height of Rings (% difference from CAD model).....	50
Figure 39: Surface roughness maps of (a) Vendor C and (b) Vendor A	50
Figure 40: Unetched (top row) and Etched (bottom row) microstructures observed transverse to the build direction of z-direction built samples of (a) Vendor A, (b) Vendor B, and (c) Vendor C, showing the variation in porosity.	53
Figure 41: Unetched (top row) and Etched (bottom row) microstructures observed transverse to the build direction of x-direction built samples of (a) Vendor A, (b) Vendor B, and (c) Vendor C, showing the variation in porosity.	54
Figure 42: Ultimate Tensile strength of vendor-built samples.	55
Figure 43: Yield strength of vendor-built samples.	56
Figure 44: Percent elongation of vendor-built samples.	56
Figure 45: Fracture surfaces of (a) Vendor A and (b) Vendor C z-direction built samples	57
Figure 46: Heating and cooling curves for x-direction built DED samples from each vendor.	58
Figure 47: Heating and cooling curves for an x-direction built sample undergoing reheating.....	59

Figure 48: Ti-6242 turbine blade repaired using DED and post-process machining [122].	63
Figure 49: Powder morphology of (a) AncorTi Beta-21s and (b) AncorTi 6242.....	65
Figure 50: Cumulative % finer for the as-received Ti-6242 and Beta 21s powders.....	68
Figure 51: As-built DOE1 Beta 21s samples on Ti-64 substrate.....	73
Figure 52: Density vs. VED for Beta 21s specimen (DOE1).	74
Figure 53: Interaction plot showing the effects of laser power and traverse rate on averaged densities for Beta 21s samples built in DOE1.	75
Figure 54: Initial layer adhesion issue observed in DOE1 builds of Beta 21S fabricated with a z-offset of 9.53mm. Sample produced with a laser power of 425 watts and a traverse speed of 10.6 mm/s.....	76
Figure 55: Density vs. VED for Beta 21s specimen (DOE2).	77
Figure 56: Main effect plot of Laser power for Beta-21s powder.	78
Figure 57: Main effect plot of traverse rate for Beta-21s powder	79
Figure 58: Main effect plot of layer height for Beta-21s powder	80
Figure 59: Main effect plot of hatch spacing for Beta-21s powder	81
Figure 60: Porosity induced in a build of Beta-21S due to excessive hatch spacing. Sample fabricated with a hatch spacing of 2.67 mm.	81
Figure 61: Main effect plot of powder feed rate for Beta-21s.	82
Figure 62: Example of gas-induced porosity retained in a Beta 21S build.	83
Figure 63: Microstructures of Beta 21S specimen (a) as-built, and after (b) STA1, (c) STA2, and (d) annealing heat treatments.....	87
Figure 64: Density vs. VED for Ti-6242 specimen (DOE1).	88
Figure 65: Interaction plot showing the effect of laser power and traverse rate on mean density for Ti-6242 (DOE1).....	89
Figure 66: Density vs. VED for Ti-6242 specimen (DOE2).	90
Figure 67: Main effect plot of laser power for Ti-6242 powder.....	90
Figure 68: Main effect plot of traverse rate for Ti-6242 powder.....	91
Figure 69: Main effect plot of hatch spacing for Ti-6242 powder.	92
Figure 70: Main effect plot of layer height for Ti-6242 powder.	93
Figure 71: Main effect plot of powder feed rate for the Ti-6242 powder.....	93
Figure 72: Examples of (a) gas-induced porosity and (b) process-induced porosity in Ti- 6242 DOE2.	94
Figure 73: 1500x magnification SEM images of (a) As-built, (b) Annealed (900) (c) STA (970/595), (d) Stress relieved (595) and (e) Stress relieved (705) Ti-6242 samples.....	97

ABSTRACT

Directed energy deposition (DED), or laser powder fed additive manufacturing (LPF-AM) is a process whereby a conical stream of metal powder is concentrated at the focal point of a laser, providing sufficient energy to create a stable melt pool. This melt pool can then be strategically deposited onto a substrate, forming layers. By slicing 3D parts into a series of 2D shapes, these layers can be stacked onto one another, creating the desired geometry. This additive manufacturing (AM) technique offers significant advantages over subtractive machining with regards to limiting material waste and the ability to produce complex geometries not achievable by traditional machining or forming processes. Compared to other fusion-based AM processes, DED offers faster material deposition rates, resulting in faster build times. Additionally, DED allows for functionally graded materials, near net-shape part repair, laser cladding and hybrid additive/subtractive manufacturing.

In the context of titanium alloys, DED has been mainly utilized for processing the industrial workhorse, Ti-6Al-4V. As such, the initial research aimed to compare the manufacturing capabilities of several vendors of DED equipment to determine the resultant variability in mechanical and microstructural properties and establish a baseline for future works. A single lot of AncorTi-64 was sent to several OEMs of DED equipment and their builds were examined on the basis of dimensional accuracy, hardness, density, tensile properties (pulling perpendicular as well as parallel to the build direction), optical micrography, scanning electron microscopy, and differential scanning calorimetry. Ti-64 builds showed considerable variation in dimensional accuracy, density, and mechanical properties between vendors. Tensile samples built horizontally showed near-wrought properties from all vendors, indicating the importance of part-specific build orientation.

Two other industrially relevant titanium alloys were chosen to further understand the feasibility of processing titanium using DED. These were the near-alpha Ti-6242 and the beta alloy Beta-21s. In both instances, process parameters were varied in a statistically driven manner to achieve fully dense samples. The first design of experiments (DOE) varied laser power and traverse rate, measuring density as the dependent variable. Based on the results of this smaller scale experiment, a larger experiment was prepared varying laser power, traverse rate, hatch spacing, layer height and powder feed rate. The optimal process parameters were then used to create tensile bars according to ASTM E-8 and heat treated using industrial heat treatments to obtain mechanical properties. Both Ti-6242 and Beta-21s were successfully processed, achieving >99.9% of theoretical density with appropriate processing parameters. DED specimen of each alloy also exhibited near-wrought mechanical properties as well as heat treatment responses consistent with their underlying fundamental metallurgy.

ACKNOWLEDGEMENTS

I would first like to acknowledge the funding support provided by the Natural Sciences and Engineering Research Council of Canada (NSERC) strategic partnerships grant for networks entitled “NSERC Network for Holistic Innovation in Additive Manufacturing (HI-AM)”.

I would also like to thank Dr. Paul Bishop for the guidance, support, and inspiration he has offered me every step of the way, as well as all my colleagues in the Net Shape Manufacturing Group and graduate student office. I would like to express my sincerest gratitude to Randy Cooke and Dr. Greg Sweet for sharing their immense knowledge and providing assistance throughout this process. Finally, I would like to profoundly thank my family for their unending support and my friends for providing me a comfortable space to relax and enjoy some much needed breaks along the way.

1 INTRODUCTION

1.1 Laser Technology and Applications

Laser is an acronym for “light amplification by stimulated emission of radiation” [1]. The beam of a laser is generated when electrons in a medium are energetically stimulated such that they move from a low energy orbit to a higher energy orbital. Upon returning to their original energy state, photons are emitted [2]. Figure 1 shows a graphical representation of this phenomena.

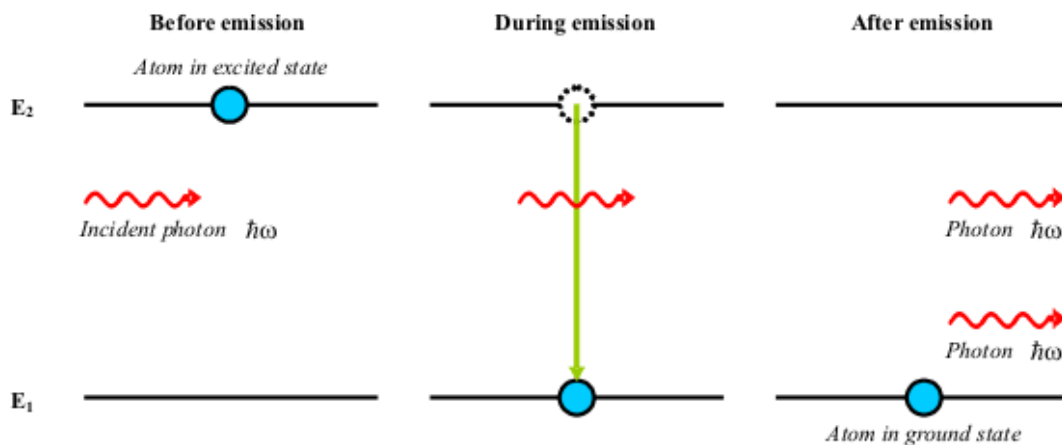


Figure 1: Graphical representation of photon emission phenomena [3]

A solid-state laser is one that uses a solid rather than a liquid as a gain medium. The gain medium provides the optical gain within the laser, which provides the necessary lasing power. The transmission of electrons from a low energy orbit to a higher energy orbit occurs within the solid gain medium [4]. Generally, this solid is composed of a primarily glass host material containing a dopant to tune the optical and vibrational properties of the material. There are a variety of common dopants including Ytterbium, Boron, Arsenic, Phosphorous and Antimony. Dopants are selected for their incoherency between excited ions and the thermal vibrations of their crystal lattices, as well as compatibility with the bulk glass material [5]. This means that their operational states can be reached with very little laser pumping.

Laser pumping is the act of imposing energy from an external source into the gain medium in order to excite atoms and produce photons [6]. The power of the laser pump is defined by the lasing threshold of the laser. The lasing threshold is the lowest level of excitation where the emissions will be controlled by stimulation rather than spontaneous emission.

Laser processing refer to technologies that use a laser as the primary energy source to heat or melt a metal feedstock. These processes serve a wide array of purposes ranging from material post-processing to near net shape part production. In the context of metallurgy, lasers have been utilized to impart beneficial residual stresses in materials through laser peening [7], to harden the outer layers of a part such as a shaft through laser surface hardening [8], and recently as the heat source in additive manufacturing (AM) processes such as laser directed energy deposition (DED) [9], selective laser sintering (SLS) [10] and selective laser melting (SLM) [11].

Lasers come in a variety of configurations depending on the desired application. They are often described based on the lasing medium used, as well as the method and frequency of electromagnetic radiation emission. Common lasing mediums include solid-state (Nd-YAG crystal), gas (He, He-Ne, CO₂), excimer (reactive gasses such as Cl and Fl mixed with inert gasses such as Argon), dye (complex organic dyes such as rhodamine 6G), and semiconductors/diodes (small, low power electronic lasers). The choice of lasing medium is often dictated by the wavelength and power output needed by a given process.

With regards to the power output needed, there are different laser emission strategies that can be utilized to further control the energy transferred to the sample. The two common styles of laser emission are continuous wave (CW) and pulsed. CW lasers maintain a relatively stable power output over a long period of time, with the actual outputted power oscillating within an allotted range. CW lasers are advantageous due to their relative technical simplicity as well as their constant heat input. Conversely, a pulsed laser utilizes a shutter capable of blocking the outgoing beam to briefly store laser power and then release it as a rapid pulse. These pulses generally last between 0.5 and 500 nanoseconds. The increased peak power offered by the pulsed lasers allows for the ablation of materials,

as well as more precise heat input with less heat being dissipated to the surrounding substrate, as in laser welding. Figure 2 shows a comparison of the power output of a CW laser and a simple pulsed laser.

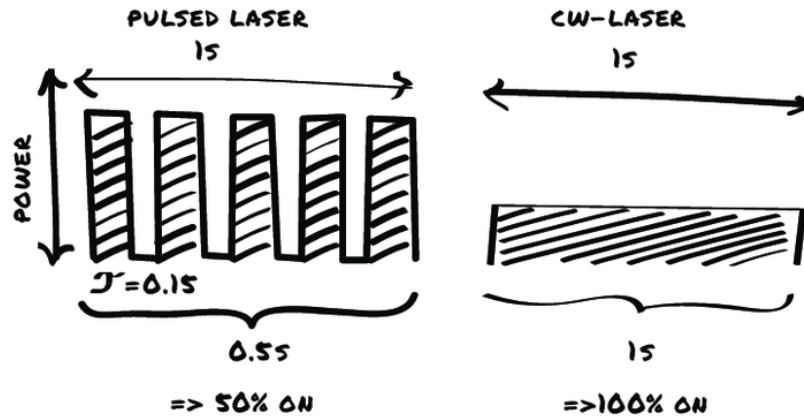


Figure 2: Power output of CW vs. PW laser [12]

Although the average power output is the same between these two methods, the higher peaks present in the pulsed laser allows for higher heat input to a given location, which may result in melting or vaporization of material more so than a gradual, low-power continuous input would be able to achieve.

1.1.1 Rapid Solidification

Rapid solidification refers to processes involving rapid quenching from a liquid state, with cooling rates around 10^4 K/s. This generally manifests much finer microstructures and the opportunity for large deviations from equilibrium. In particular, increases in solid solubility and the formation of metastable phases (crystalline, quasicrystalline, and amorphous). Rapid solidification processes have traditionally been used for powders, flakes, ribbons, wires, and foils. All these traditional uses involve products with a very small surface area to volume ratio (e.g., very thin, wide samples). However, with the introduction of high-density heat input devices such as lasers, it is possible to achieve thicker rapidly solidified samples. By layering these individual tracks, it is possible to create large samples with

properties representative of rapid solidification processes, as is the case with AM. Rapid solidification processes result in several interesting compositional and microstructural effects as discussed below.

Solute trapping, or solute supersaturation, refers to an increase in solute concentration within the solid phase of a solidifying sample resulting from the solute front velocity exceeding the rate at which solute atoms in the melt naturally diffuse into the solid phase. The ratio of the concentration of solute in the solid (C_s) to the concentration of solute in the liquid (C_l) is referred to as the partitioning coefficient (k) and is defined as follows for equilibrium solidification: [13]

$$k = C_s/C_l \quad (1)$$

In cases of rapid solidification, one commonly accepted theory is the continuous growth model, in which the partition coefficient is defined as a function of velocity ($k(V)$).

Building off the simplified partition coefficient for equilibrium conditions, the velocity dependent partition coefficient takes the form: [13]

$$K(V) = (k_e + V/V_D)/(1 + V/V_D) \quad (2)$$

Where V_D is the characteristic solute trapping velocity, a ratio of the solute-liquid diffusion coefficient (D_L) and the solid-liquid interface width (W), estimated as 1-10 m/s. However, in practice, V_D is better treated as a parameter fit to a series of laser melting experiments ranging from interfacial equilibrium to complete solute trapping ($k(V)$ approaching 1). It has been shown in various dilute alloys that as the velocity (V) approaches the characteristic solute trapping velocity (V_D), the solute atoms do not diffuse into the solid quickly enough and are overcome by the rapid movement of the solid-liquid interface resulting in undiffused solute becoming trapped, often changing the resulting microstructure.

1.1.2 Laser Welding

Laser welding is an advanced joining technique involving the use of a laser to join a variety of materials. The laser provides a high-energy-density heat source capable of

penetrating deep into the material and rapidly forming a narrow melt pool. The rapid melt pool formation and deep penetration allows for high welding rates compared to traditional welding processes. Figure 3 shows a basic laser welding apparatus, involving a butt joint perpendicular to the laser welding head, and focused below the surface for complete penetration of the material thickness.

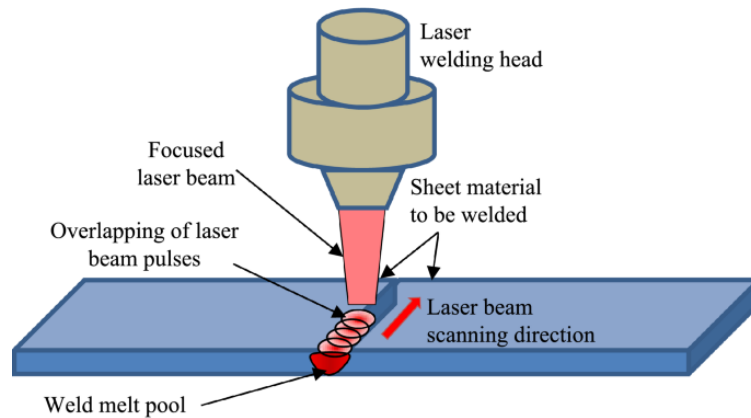


Figure 3: Basic laser welding apparatus of a butt joint [14]

Figure 4 shows the penetration depth of various types of welding, highlighting the advantage of laser welding over traditional approaches. Electron beam welding, which uses a beam of electrons as the energy source as opposed to a laser, has superior penetration and a narrower weld pool than even laser welding, but carries with it a higher cost and requires a high vacuum processing chamber. Laser welding is commonly used with metals and plastics [15] and has also been used to successfully join glass [16]. Metal sheets ranging from 0.01 mm to ~50 mm in thickness can be laser welded, with the latter requiring a shielding gas (helium, argon, or nitrogen).

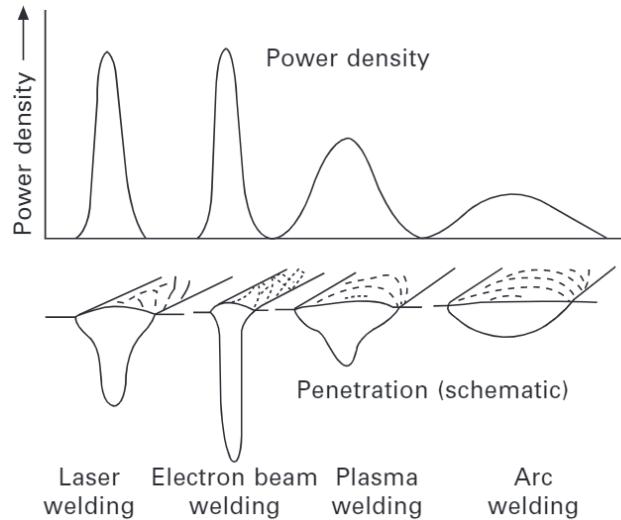


Figure 4: Weld pool depth of a variety of welding processes [17]

1.1.2.1 Types of Lasers for Welding

The three most common laser types in laser welding are CO₂, Nd: YAG, and fiber lasers. CO₂ lasers pass an electrical current through a sealed tube filled with a gas consisting of carbon dioxide, nitrogen, and hydrogen. One end of the tube is a fully reflective mirror, whereas the other is partially reflective, allowing sufficiently bright light to pass through. As the current is passed through the tube, the nitrogen molecules become excited and begin to vibrate, which in turn excite the carbon dioxide molecules. Eventually the system reaches a state known as population inversion whereby the number of excited particles is greater than the unexcited particles. The vibrating nitrogen molecules are in a high energy state, and when these high energy nitrogen molecules come into contact with the low energy helium molecules, they will lose their excited state through the emission of photons. These emitted photons will be reflected by the mirrored tube ends, gaining intensity until eventually transmitting through the partially reflective mirror. CO₂ lasers produce electromagnetic radiation with a wavelength of 10.6 μm and with net outputs as high as 50-kW power in continuous wave (CW). Figure 5 shows an example of a CO₂ welding apparatus.

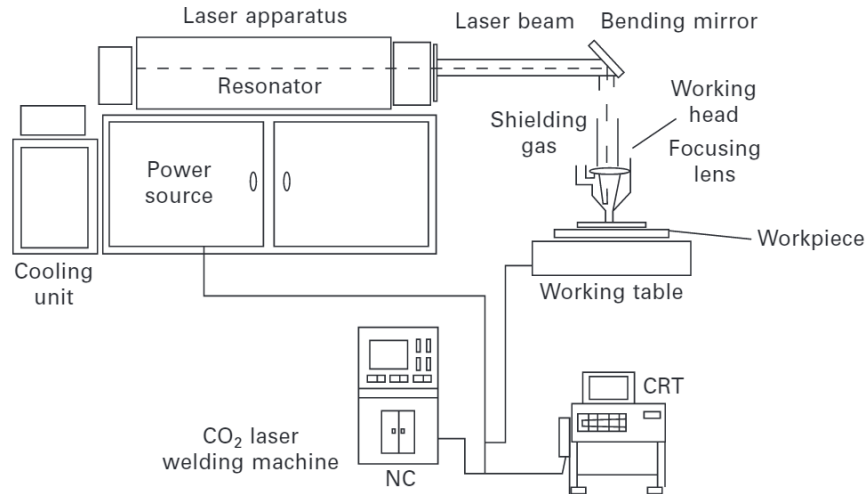


Figure 5: CO₂ laser welding apparatus [17]

Conversely, Nd: YAG lasers are solid-state lasers. A solid-state laser is one that uses a solid rather than a liquid or gas as a gain medium. The gain medium provides the optical gain within the laser, which provides the necessary lasing power, as described above. CW Nd: YAG lasers generally operate between 2 and 7 kW of power. In terms of processing capabilities Nd: YAG lasers have the advantage of offering pulsed wave (PW) operation, whereby the lasing is done in discrete pulses rather than continuous power output. PW allows for control of a variety of process parameters such as pulse power, pulse rate and pulse shape that provides greater control over heat input and positional accuracy allowing for the welding of small and thin parts that would not be possible with traditional welding techniques [18]. Figure 6 shows an example of a Nd: YAG laser setup.

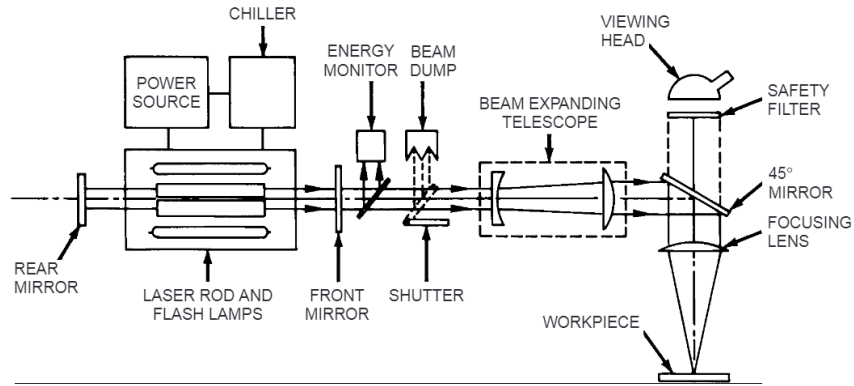


Figure 6: Nd: YAG laser welding apparatus [17]

Unfortunately, Nd: YAG lasers exhibit very poor electrical efficiency (<8%) [19] and despite being widely used historically, they have been replaced by the more favorable fiber lasers. Instead of coupling the Nd: YAG output to an optic fiber, fiber lasers generate the laser power within the fiber itself. Fiber lasers offer high beam quality, power generation and reliability with low noise and jitter in a compact form factor. Fiber lasers have been made possible by advancements in laser diodes which are semi-conductor devices capable of producing lasing conditions at the diode junction with electrical current input. Because they utilize these laser diodes, fiber lasers have higher electrical efficiency and maximum power.

1.1.2.2 Laser Welding Modes

There are two common modes of laser welding: conduction and keyhole. Conduction welding produces melt pools with similar aspect ratios to traditional welding processes, as the laser power used is insufficient to penetrate deeply into the sample. This can be advantageous in thin wall parts, and situations where the final weld is going to be visible because the wide aspect ratio produces a rounded weld that does not require grinding or finishing [20]. Figure 7 shows the melt pool generated in conduction welding.

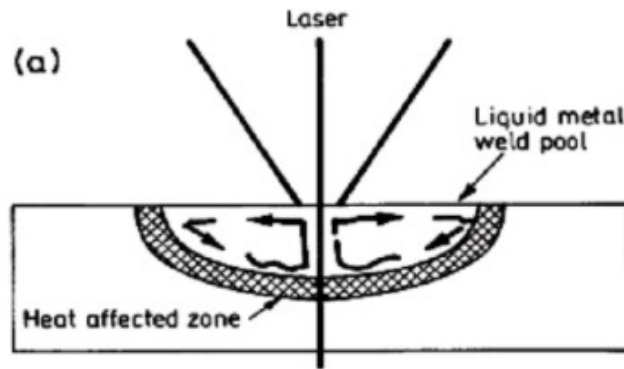


Figure 7: Conduction welding melt pool diagram [21].

Keyhole welding is a deep penetration technique that involves formation of a hole at the leading edge of the weld pool, which is subsequently filled in by the trailing molten metal forming a fully homogenous weld. With adequate power density, the metal surrounding the keyhole will vaporize forming a hollow column supported by the vapor pressure of the metal. As the laser proceeds, the molten metal will eventually overcome this vapor pressure and flow in the opposite direction of the weld, filling the column and solidifying. Depth-to-width aspect ratios of 10 to 1 can be obtained using keyhole welding techniques, with very narrow fusion zones. Figure 8 shows the melt pool generated during keyhole welding.

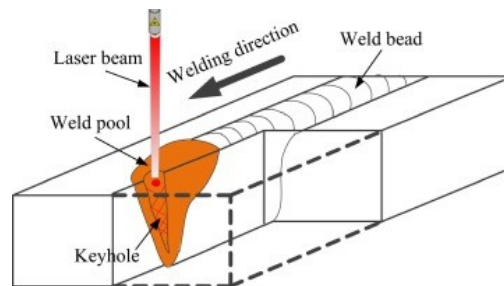


Figure 8: Keyhole generation in laser welding [22]

1.1.2.3 Laser Welding Applications

Laser welding is widely used in the automotive industry, owing to its high weld rate that makes it appropriate for the high volume of welding necessary in vehicle manufacturing.

Additionally, laser welding can be robotically automated to produce repeatable welds, making it easy to implement into high-speed production lines. Within the automotive sector, some examples of large-scale laser welding applications include door frames, trunks, hoods, and chassis. Shallow penetration or PW mode laser welding is also used for small scale electrical connections such as airbag initiators, starter motor windings, and battery tab connections.

1.1.3 Laser Cladding

Laser cladding is an offshoot of laser welding applied to the surface of a part. The surface of the substrate is melted, and material is added in wire, powder, or strip form to build up worn surface, or to deposit a material that offers a mechanical advantage over the base material in terms of traits such as hardness or corrosion resistance. Laser cladding can produce uniform, low porosity, and low dilution samples. Lasers are advantageous in this process due to the ability to accurately focus the heat input just below the surface, minimizing the heat affected zone and eliminating distortion. Figure 9 shows a laser cladding apparatus [23].

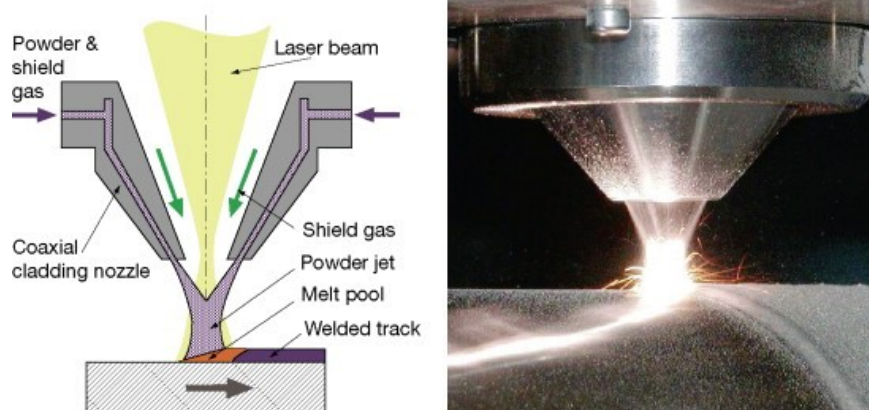


Figure 9: Laser cladding apparatus [23]

A melt pool is formed at the substrate and maintained as additional material is fed into it through either a coaxial feeder surrounding the laser or a single feed track in front of the laser head. By moving the substrate relative to the deposition head, either by rotating about

an axis of symmetry or by scanning back and forth, this melt pool can be used to create a uniform layer of adjacent weld beads. The thickness of a single deposited layer is generally between 50 microns and 2 millimeters [24].

In the context of titanium alloys there has been significant research into various methods of laser cladding. For example, Ti-64 substrate has been clad with commercially pure titanium (CP-Ti), successfully producing a homogenous coating for biomedical applications [25]. In addition to simple cladding, researchers have also shown feasibility of repairing structural members of near alpha titanium alloys using laser cladding [26]. There are also several coatings that have been examined to improve the relatively poor tribological performance of titanium and improve its capabilities in severe wear and friction conditions. In one instance, coating Ti-64 with a 60% tungsten carbide (WC) and 40% NiCrBSi was able to triple the microhardness values and improve wear resistance by up to 400 times [27]. However, some coatings that were able to improve microhardness and wear resistance showed poorer corrosion resistance. Coating Ti-64 with TiB was able to improve microhardness 3-4 times, and the corrosion resistance was improved through the addition of 2 wt% Nd_2O_3 [28]. Similar results were observed in a nickel based composite coating doped with CeO_2 which improved corrosion resistance and maximized wear resistance up to around 3 wt% CeO_2 after which corrosion resistance decreased [29]. Laser cladding shares many similarities with powder fed laser AM processes, whereby a powder feedstock is fed into the path of a laser and deposited accurately through computer numerical control. As such, the success of laser cladding in the context of titanium is promising its use in laser directed energy deposition (DED). The next section will discuss the advancement from simple geometries in laser cladding to the freeform fabrication of laser DED.

1.2 Additive Manufacturing

AM at its core refers to the production of a desired part through progressive addition of material, rather than subtractive removal of material as is common in traditional machining processes. ASTM has defined AM as “a process of joining materials to make objects from

3D model data, usually layer-upon-layer, as opposed to subtractive manufacturing methodologies” [30]. The common layer-upon-layer approach involves dividing a 3D model into a series of 2D cross-sections that, when stacked upon one another, form the desired geometry. This layer-upon-layer approach allows for production of unique shapes resulting from the lack of constraints such as draft angles, undercuts, and machining tool access concerns [31]. AM has been successfully utilized with a wide variety of materials including polymers, ceramics, composites, biological materials, and metals [32]. AM is commonly used for rapid iterative design assessments as it eliminates the need for expensive and long lead-time tooling.

In terms of industrial use, AM features high upfront equipment cost as with most manufacturing techniques. However, in many applications this may eventually be offset by the savings in material waste, which offers both a monetary and environmental incentives. The AM industry was valued at US\$5.933b in 2017 and is projected to reach a total market size of US\$22.2b by 2022 [33]. This market analysis encompasses the 7 common AM technologies; Vat polymerization, metal extrusion, material jetting, binder jetting, directed energy deposition, powder bed fusion and sheet lamination. Of these technologies, 4 are capable of utilizing metal feedstock; binder jetting, powder bed fusion, sheet lamination and DED.

1.2.1 Directed Energy Deposition

DED refers to an array of processes in which focused thermal energy is used to fuse materials by melting as they are deposited [34]. The source of thermal energy and the form of the material feedstock can vary depending on the application, each offering unique advantages and disadvantages. The common sources of thermal energy are laser, electron beam and plasma arc; their relative efficacy for several relevant metrics are shown in Figure 10.




















Process	Build Volume	Detail Resolution	Deposition Rate	Coupling Efficiency	Potential for Contamination
Laser Directed Energy Deposition					
Electron Beam Directed Energy Deposition					
Arc Plasma Directed Energy Deposition					
	Lower 				Higher
This table is intended as a general guide. Variations in individual systems and process advancements may affect the characteristics of each process.					

Figure 10: Comparison of common DED thermal energy sources [35]

For the feedstock there are only 2 common forms, metal powder and wire. Wire feedstock offers a higher deposition rate and lower expense when compared to metal powder [36]. However, powder is capable of higher resolution deposits which improves the quality and accuracy of smaller features such as thin walls and sharp corners, and the ability to easily introduce powders of varying compositions to perform in-situ alloying.

DED equipment is available in a variety of configurations featuring 3-(XYZ), 4-(XYZA) and 5-(XYZAC) axes, respectively. In addition to the number of axes, manufacturers vary whether the motion is occurring at the substrate using a CNC multi-axis trunnion or at the deposition head using a robotic arm. Figure 11 shows a 5-axis trunnion, capable of XYZAC movement.

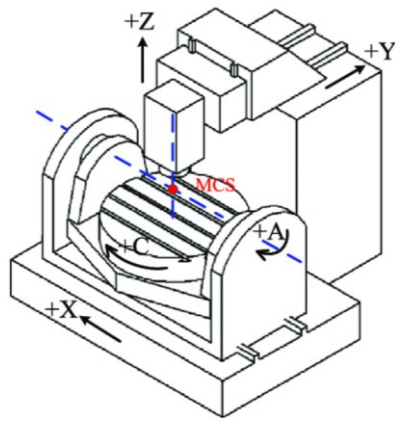


Figure 11: Trunnion capable of 5-axis movement [37].

Due to its lower resolution compared to other metal AM processes, parts will often require separate post-processing such as machining for an improved surface finish, heat treatments, or hot isostatic pressing [38]. As such, hybrid units are available that incorporate traditional subtractive tooling. By combining subtractive and AM, parts can be produced with improved surface finishes and dimensional accuracy [39].

DED equipment can also feature a closed (inert) or open atmosphere depending on the materials of interest. When working with reactive materials such as titanium and aluminum alloys, a closed atmosphere is preferred as it allows for an inert gas atmosphere (such as argon) thus minimizing the amount of oxygen present, which can have a significant detrimental effect on the final mechanical properties.

1.2.2 Laser Powder-Fed DED Equipment

Laser powder-fed DED consists of a laser as the thermal energy source and blown metal powder as the feedstock. The metal powder is held in a sealed powder feeder that is kept under closed atmosphere to minimize the introduction of oxygen. The powder feeder consists of a hopper above a secondary chamber containing an auger. The powder is gradually fed into the secondary chamber where it is agitated by the auger and picked up by a perforated plate. The powder held in the perforated plate is rotated past a flow of argon

which blows it into the deposition head. The mass flow rate of powder into the system is controlled by the RPM of the auger. The system used for this research is equipped with multiple powder feeders that can be individually controlled and mixed before reaching the deposition head which allows for functionally graded materials [40] and in-situ alloying [41]. Figure 12 shows (a) a powder feeder and (b) the auger feed system.

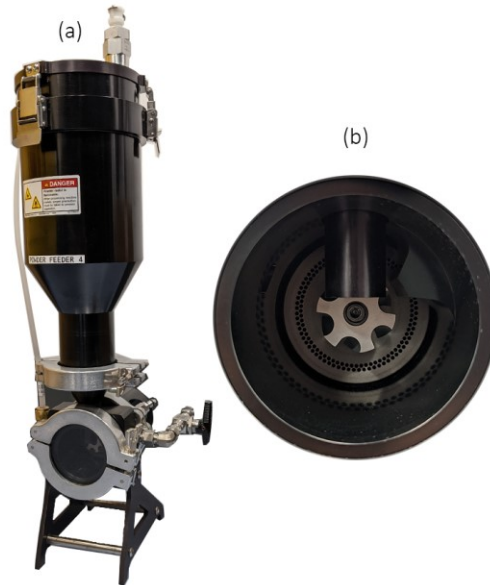


Figure 12: (a) Individual powder feeder and (b) Auger feed system

The metal powder is fed into the deposition head, which consists of four copper nozzles in a conical arrangement, centered around the laser opening. The laser opening has a constant flow of gas designed to prevent the backflow of powder that could potentially damage the optics stack. A schematic of a typical deposition head is shown in Figure 13.

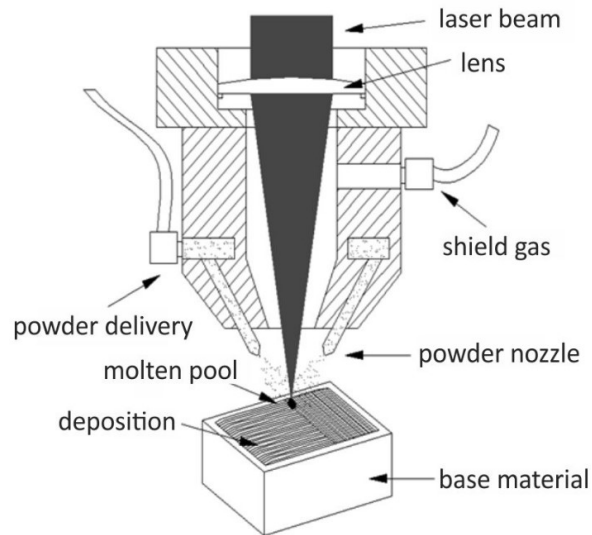


Figure 13: Deposition head components [42]

The most common laser currently used in DED is the Yb-fiber laser due to the fact that at common operating wavelengths it can be transmitted through flexible fiber optic cables. The use of fiber optic cables allows for movement of the deposition head as well as flexibility of the location of the lasing unit in the machine. The fiber optic cable enters the unit at the top of the deposition head where the laser is focused through the optic stack which consists of a series of lenses intended to ensure circularity, spot size accuracy, and correct focal length. In addition to the corrective lenses, there are a series of optically clear lenses that do not alter the laser intended to protect against backflow of powder.

The four powder feed nozzles are arranged such that the streams intersect at the focal point of the laser, maximizing the amount of thermal energy transferred from the laser to the powder particles and creating a melt pool. The deposition head is capable of moving up and down along the z-axis to locate this common focal point slightly below the surface of the substrate on which the desired part will be built. The optimal penetration of this initial melt pool into the substrate varies depending on the material being used, and the thickness of the substrate. The substrate sits on a CNC trunnion capable of rotation about

the z-axis and the x-axis, which is then mounted to the machine's table which provides the linear motion in the x and y axes. With this arrangement, the substrate is manipulated about the stationary laser deposition head to deposit the individual layer geometry, and the vertical z-axis movement is used to advance to subsequent layers.

To maintain a closed atmosphere, the deposition unit is contained within an airtight enclosure featuring a pressurized rubber seal surrounding the main door. An additional smaller pressure vessel is commonly attached to the side of the main chamber with sealed doors separating it. This vessel is known as an antechamber and is used to minimize the amount of gas lost when passing objects from the open atmosphere into the closed chamber. To allow the user to manipulate objects within the main build chamber, a set of gloves are mounted to the front panel that can be rolled up and sealed when not in use. Figure 14 shows the sealed atmosphere unit with antechamber.

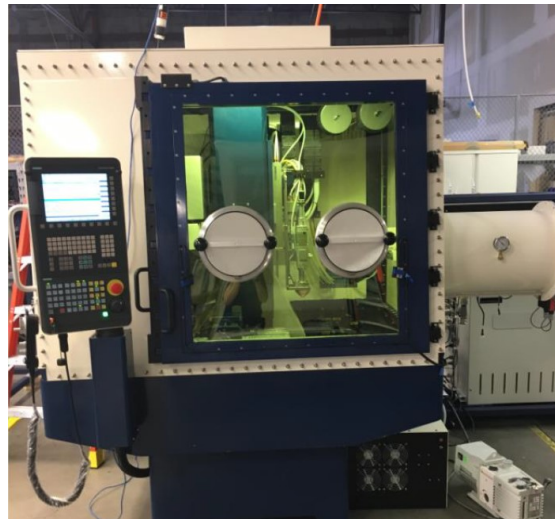


Figure 14: Glovebox and Antechamber

1.2.3 Process Concerns

When attempting to produce an adequately dense sample through laser DED, the most common issue that tends to arise is residual porosity. One mechanism through which it commonly occurs is gas entrapment. This refers to situations wherein gases present and/or evolved during DED collect in the weld pool to form bubbles within the melt. Due to the rapid nature of solidification in laser DED, these bubbles cannot escape before solidification, and thereby prompt the formation of pores in the finished product [43]. Sources of gas include molecular species adsorbed onto the feedstock powder (CO_2 , H_2O , O_2), inert gas pockets (Ar) trapped within the powder particles during atomization, and the protective inert atmosphere (Ar, N_2) utilized during the DED process itself. Gas-induced porosity has been widely studied in the context of traditional welding as it is a recurrent issue there as well [44, 45]. Porosity of this nature is characterized by a highly spherical morphology with a diameter smaller than individual powder particles [46]. Figure 15 shows an example of a gas-induced pore.

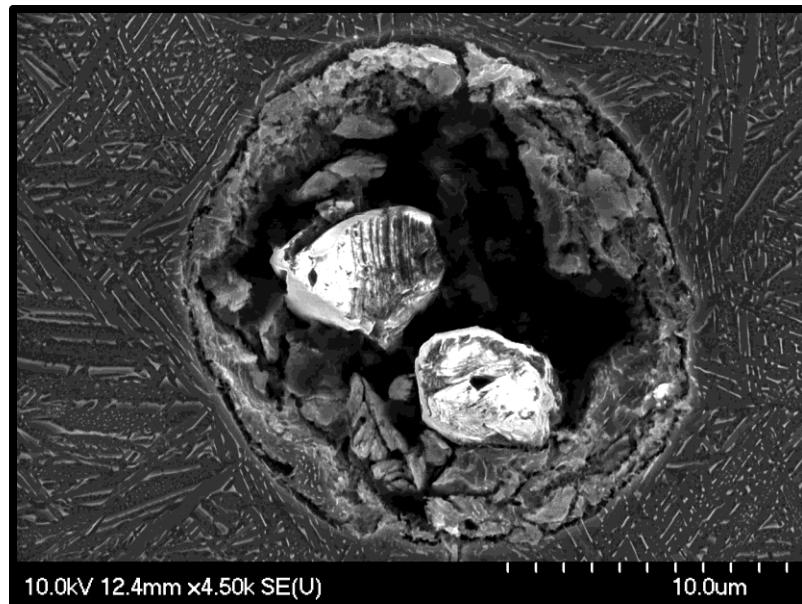


Figure 15: Gas-induced pore.

A second mechanism of porosity formation is based on lack of adhesion; also referred to as process-induced porosity. Here, interconnected networks of pores are present and these result from a failure to properly bond adjacent layers of the build. Pores of this nature have an irregular morphology and are generally larger than the individual powder particles (Figure 16). In addition, they often contain unmelted powder particles that can be readily observed in micrographs. Lack of adhesion porosity is the result of inappropriate choices in process parameters. For example, a clear inverse relationship has been identified between laser power and the amount of process-induced porosity [48, 49]. The existence of this type of porosity indicates a general failure to homogeneously melt and solidify the material of interest. Regardless of the underlying formation mechanism, residual porosity maintains a decisively negative impact on mechanical properties.

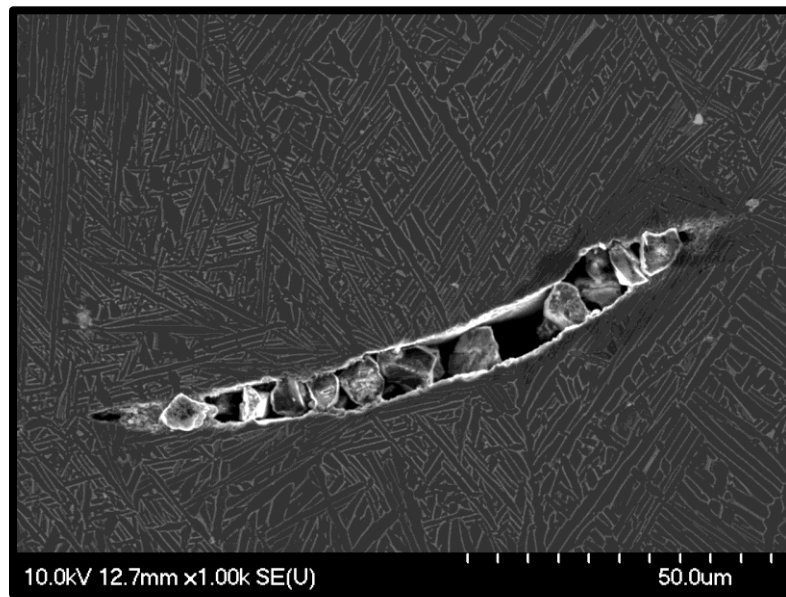


Figure 16: Process-induced pore.

1.2.4 Influence of Process Parameters

1.2.4.1 Laser Power

Laser power refers to the rate at which energy is emitted from a laser, commonly measured in units of watts (W), which is equivalent to one joule per second (J/s). It is the primary process parameter of interest relating to the laser portion of a DED system. This value is

easily monitored throughout the build process with reasonable accuracy and can be held about a fixed value or varied to achieve differential energy input at various stages of the build.

Laser power controls the amount of heat energy inputted at the focal point which influences the melting behavior of the substrate as well as the incoming powder. There is a material dependent minimum laser power below which the substrate will not melt, and the initial layer will fail due to lack of adhesion [50]. Conversely, too high of a laser power, leads to excess heat throughout the build process which is inefficient and can result in detrimental effects. For example, when processing alloys that readily absorb oxygen from their environment, excess heat increases the extent of specimen oxidation as the entire sample is heated throughout the process instead of focusing the heat on the concentrated area surrounding the melt pool. Excess heat input also has a negative effect on the build process itself, leading to an increase in the occurrence of balling whereby splatter adheres to the powder feed nozzles. This can lead to clogging or invoke large inclusions in the build if balls fall off.

1.2.4.2 Traverse Rate

Traverse rate refers to the speed at which the substrate moves relative to the deposition head. This is functionally similar to scan speed in laser powder bed fusion which refers to the speed of the laser scanning over the surface. Traverse rate is particularly important in the laser DED process as it determines whether the melt pool is adequate to melt the incoming fed powder. If the traverse rate is too fast, the substrate will outrun the melt pool promoting the occurrence of inter-track gaps and failed adhesion. The substrate is also unlikely to sufficiently melt with high traverse rates leading to early layer build failures. At slow traverse rates, the issue of overbuilding is introduced. Since the powder is continuously fed at the same mass flow rate throughout the build, it will constantly feed into the melt pool as long as there is sufficient energy to accept it. Because of this, if the traverse rate is slow, it will feed excess powder which will melt and form a taller geometry than desired. This can lead to inaccurate build dimensions and inconsistent layers.

1.2.4.3 Scan Pattern

Scan pattern is the path that the melt pool will follow as it is deposited onto the substrate. Choice of scan pattern will differ depending on the geometry of the part being produced. In the context of the simple geometries used in process parameter optimization, common scan patterns include single track one-way, single-track zigzag, bi-directional and inward spiral. Figure 17 shows the different scan patterns.

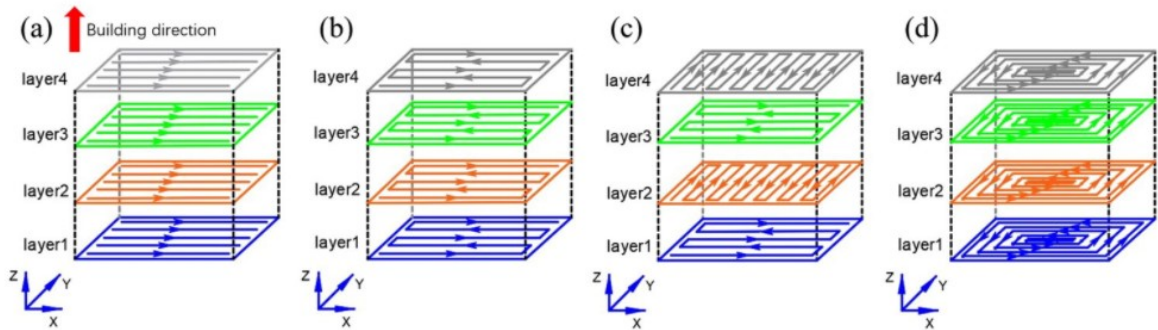


Figure 17: Various Scan Strategies (a) single track one-way, (b) single track zigzag, (c) bi-directional and (d) inward spiral [51]

The optimal scan pattern for a simple rectangle-shaped part is one that minimizes the amount of excess heat caused by sharp changes in direction such as when the melt pool reaches the edge of the sample and reverses direction. Additional considerations when choosing a scan pattern include the start/stop points as the laser must dwell briefly to form the melt pool at these locations. If these start/stop points occur on the same side of the sample for every row deposited, it can lead to overbuilding on that side which will be visible in the top layer of the final part.

It is also important to consider the orientation of the pattern between subsequent layers. As the layers are deposited it is necessary to vary the orientation to fill the gaps created when deposited lines sit directly on one another. Failure to appropriately orient layers relative to one another will lead to poor layer adhesion and extensive porosity throughout the samples. It is generally accepted that the optimal rotation of the scan pattern between

layers is approximately 67 degrees as it mathematically minimizes the opportunity for repeat layers and maximizes volumetric coverage [52]. However, scan strategies using a variety of angles greater than 0 have been used to successfully produce fully dense parts [53]. Since DED processing has a larger resolution than SLM where the 67-degree rotation originated, it melts more of the previous layers and is therefore less sensitive to the chosen rotation between layers. Accordingly, a 90-degree rotation is generally acceptable in DED.

1.2.4.4 Atmosphere

The atmosphere refers to the environment in the immediate vicinity of the build during the deposition process. When processing reactive metals, it is necessary to minimize the presence of gasses that are detrimental to the performance of the final part. Due to the heat input associated with the DED process, many materials will have increased uptake of these gasses if they are present even in small amounts [54]. To eliminate the possibility of these detrimental effects, the impure gas present naturally around the build is replaced by pure argon as it is non-reactive. There are two common methods of ensuring pure atmosphere surrounding the build during deposition and cooling: sealed atmosphere and shielding gas. In a sealed atmosphere system, the entire deposition apparatus is contained within a sealed build chamber. The entire build chamber is evacuated of air using a vacuum pump and then refilled with pure argon. This pure argon can be recirculated through a dri-train which further purifies it [55]. Sealed atmosphere systems ensure a pure atmosphere is maintained throughout the entire build and cooling process, and there is minimized risk of contaminating the build with reactive species such as oxygen or nitrogen. Sealed atmosphere systems are also able to utilize the argon efficiently, with small leaks resulting from imperfections in the build chamber being the only source of lost gas during normal use. However, the efficiency is decreased when considering the need to open the system to air to perform maintenance or change material systems, in which case large quantities of argon are lost. Figure 18 shows an example of a sealed atmosphere build chamber.



Figure 18: Closed atmosphere DED unit [56]

The alternative technique more closely resembles traditional welding processes, whereby the shielding gas is only present in the immediate vicinity of the melt pool. In the case of welding, this works because the heat affected zone is concentrated and the amount of heat input to the base metal outside of the shielding gas is insufficient to heat the base metal to the point where it will readily attract oxygen. In the case of DED, the heat affected zone can be much larger depending on the power-related process parameters, so it is necessary to widen the coverage area of the shielding gas. Figure 19 shows an example of an open atmosphere DED unit.



Figure 19: Open atmosphere DED unit [57]

Both techniques can produce samples with minimal undesired gas uptake, however there are advantages and disadvantages with each. The shielding gas technique has the advantage of feeding the pure argon gas directly around the melt pool, whereas the closed atmosphere risks decreased purity of the argon over time as the circulated argon atmosphere picks up contaminants and/or adsorbed gas from the feedstock powder. The closed atmosphere method is more efficient with its use of argon, since the only loss of argon is through gradual leaks associated with imperfections in the chamber, whereas the shielding gas method loses most of the argon to the surrounding air. With large parts, the sealed chamber is better able to shield the entire part during post-build cooling than the shielding gas method, which can decrease oxidation.

1.2.4.5 Powder Flow

The powder flow rate, or flowability refers to the ease with which a bulk of particles moves throughout a system [58]. Since the powder feed mechanism relies on a combination of gravity as well as gas-assisted passage through a series of tubes, the flowability of a powder is an important consideration. Powder flow rate is measured using a hall flow meter. A hall flow meter is a precisely machined conical hopper with a standardized opening at its peak. A known quantity of powder (commonly 50g) is placed into the hopper with the opening covered, then the hopper is opened and the amount of time for it to completely empty is

measured. The value is reported as either seconds per 50 grams (s/50g) or grams per second (g/s) [59]. Figure 20 shows the hall flow meter apparatus.



Figure 20: Hall Flow Meter [60]

In the context of DED, the hall flow rate of a powder has a direct impact on the mass flow rate of powder transferred to the weld pool. A powder that naturally flows better will require a lower RPM setting on the feeder unit to achieve the same mass flow rate as a poorer flowing powder. As such, measuring the powder feed rate prior to using a specific powder in DED processing is required as powders typically have unique flow characteristics. Here, the mass of powder that flows through the feed nozzles in 60 seconds is measured for a range of powder feed RPMs. This is done using pre-weighed anti-static bags placed over the powder feed nozzles for the set amount of time. By measuring the mass of powder collected several times and converting to grams per second this can be plotted against RPM to confirm the linear relationship and allow for inclusion of mass flow rate when calculating volumetric energy densities.

1.3 Titanium Alloys and Titanium DED

Titanium alloys began seeing popularity around the 1950s as high-performance military aviation began pushing the boundaries of what was possible with existing materials. Titanium is preferable over competing materials such as superalloys, steel, and aluminum due to several factors. For one, pure Titanium has a density of 4.5 g/cm^3 , which is

considerably lower than Iron (7.874 g/cm^3) and Nickel (8.9 g/cm^3). Despite this lower density, titanium alloys can achieve tensile strengths comparable to some martensitic stainless steels, and better than austenitic and ferritic stainless steels [61]. Titanium has a higher cost than ferrous based alloys due to lower demand and increased costs associated with extraction and processing, however its cost is comparable to many superalloys [62]. Titanium alloys also display greater corrosion resistance than stainless steel in many environments and can exhibit biocompatibility making them appropriate for certain medical applications [63].

Microstructurally, metals consist of relatively simple crystal lattices made up of metal atoms. Common crystal lattices are body-centered cubic (BCC), face-centered cubic (FCC), and hexagonal close packed (HCP). Figure 21 shows simplified diagrams of these particular crystal lattices.

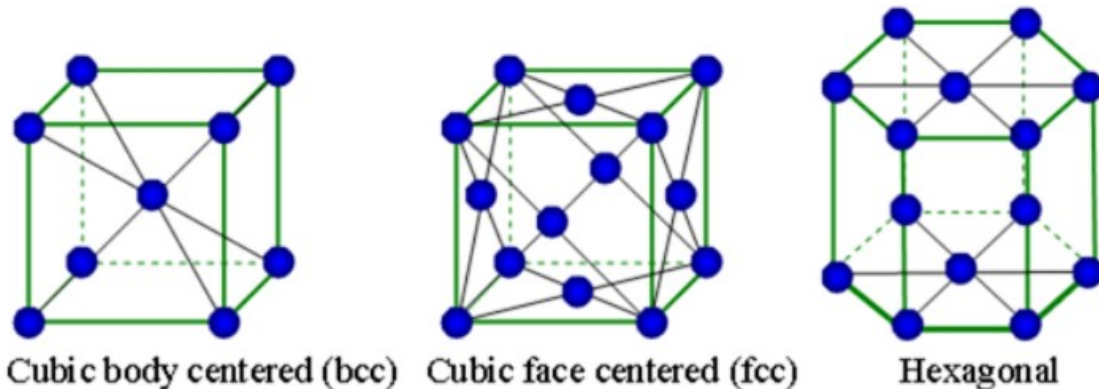


Figure 21: Simplified diagrams of common crystal lattices [64]

Similarly oriented crystal lattices will group to form an arrangement known as a grain. Since crystal lattice orientation differs over the length of a material, metal such as titanium will consist of many grains unless specifically grown as a single crystal. The points at which grains connect are known as grain boundaries. Titanium is an allotropic element, which means that depending on temperature it can take different crystallographic forms. At room temperature the dominant crystal structure is hexagonal close packed (HCP),

known as the alpha phase. At elevated temperatures the crystal structure transforms to a body-centered cubic (BCC) crystal structure, called the beta phase. The temperature at which alpha transforms into beta is known as the Beta-Transus temperature and can be controlled by the addition of alloying elements. Titanium alloys are divided into several categories based on the dominant phases present at room temperature: Alpha, near-alpha, alpha-beta, and beta. These will be discussed in the section that follows.

1.3.1 Classification and Properties of Titanium Alloys

1.3.1.1 Alloying Elements and Microstructure

The phases present at room temperature in titanium alloys are controlled by the constituent alloying elements. Since titanium alloys are defined based on their beta transformation temperature (beta-transus), alloying elements can be classified as either beta stabilizers or alpha stabilizers. Beta stabilizers will lower the beta-transus thereby increasing the capacity for beta phases to be present whereas the opposite is true for alpha stabilizers. Alpha stabilizers include aluminum, gallium, germanium, carbon, oxygen, and nitrogen, with aluminum being the most common. In particular, the presence of interstitial oxygen, nitrogen and carbon will significantly raise the beta transus temperature (stabilizing the alpha phase).

For beta stabilizers there are two categories based on the strengthening mechanism in play. Elements in the beta isomorphous group are miscible in the beta phase (molybdenum, vanadium, tantalum, columbium) meaning they are similar enough to bcc titanium that they do not form intermetallics. Elements in the eutectoid group (manganese, iron, chromium, cobalt, nickel, copper, and silicon) form eutectoids below the beta transus temperature and have low solubility in alpha titanium. As with the alpha phase, existence of interstitial elements (hydrogen in this case) has a significant effect on the beta transus, lowering it and therefore stabilizing the beta phase. Beta alloys are commonly composed of elements from both the eutectoid and isomorphous groups which serves to stabilize the beta phase and prevent formation of undesirable intermetallics at high temperatures.

Pseudo-binary phase diagrams can be generated based on the quantity of beta stabilizing alloying elements present in a given alloy to aid in comparison of select alloys. Figure 22 shows common titanium alloys on a pseudo-binary phase diagram indicating the dominant phase present through a range of temperatures.

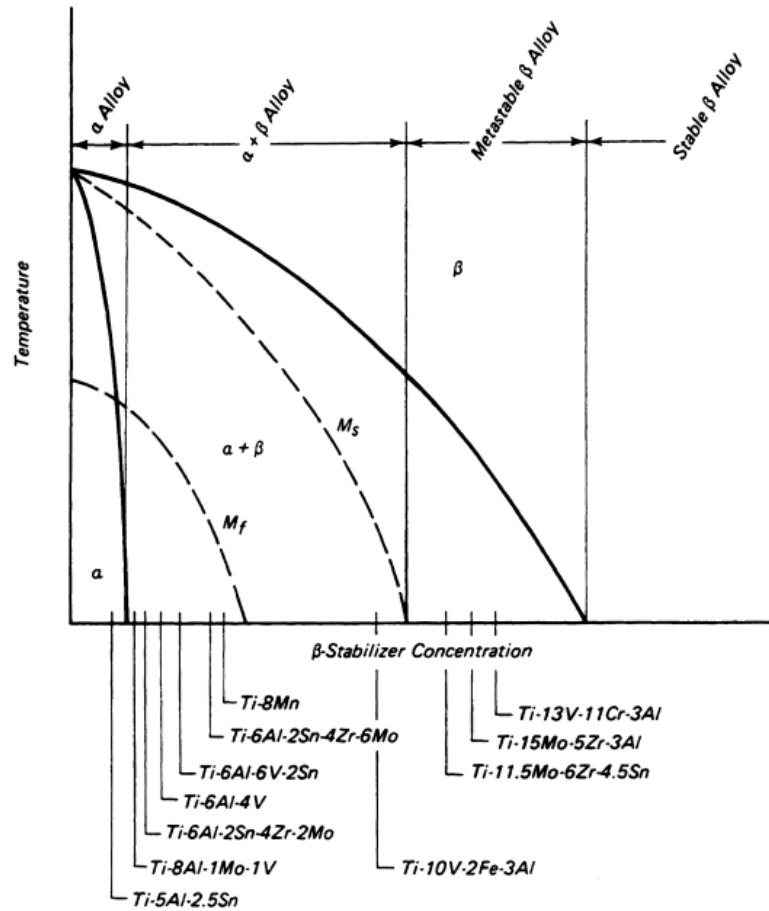


Figure 22: Common titanium alloys on a pseudobinary phase diagram indicating dominant phase throughout range of temperatures [65].

Alpha alloys, such as Ti-5Al-2.5Sn, are comprised of a fully alpha-phased microstructure at room temperature. Alpha-beta alloys (the most common being Ti-6Al-4V) transform to a fully beta microstructure at high temperatures but upon cooling return to alpha and

moderate amounts of retained or transformed beta. Conversely, near-beta or beta alloys can retain large amounts of the transformed beta at room temperatures. Within the alpha and beta phases, morphological microstructural variations can occur depending on several factors including chemistry, cooling rate, the temperature from which the alloy was cooled, and the extent of cold work. Microstructures can be coarse or fine, acicular (needle-like) or equiaxed. Figure 23 shows commonly observed equiaxed alpha, equiaxed alpha + beta, acicular alpha + beta and equiaxed beta.

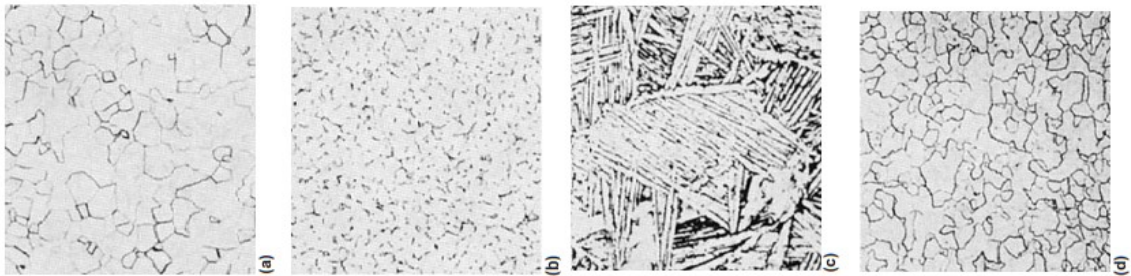


Figure 23: (a) Equiaxed alpha, (b) equiaxed alpha+beta, (c) acicular alpha+beta) and (d) equiaxed beta microstructures [66].

Depending on how an alloy is heat treated, different microstructures can result. For instance, cooling the near-alpha titanium alloy Ti-8Al-1Mo from above the beta transus will result in acicular alpha, whereas cooling it from within the alpha+beta region will result in alpha platelets with intergranular beta phase present. The coarseness of the equiaxed microstructure is dependent on what temperature within the alpha+beta region the sample was cooled from. Figure 24 shows the various microstructures produced when cooling a near-alpha alloy from different regions.

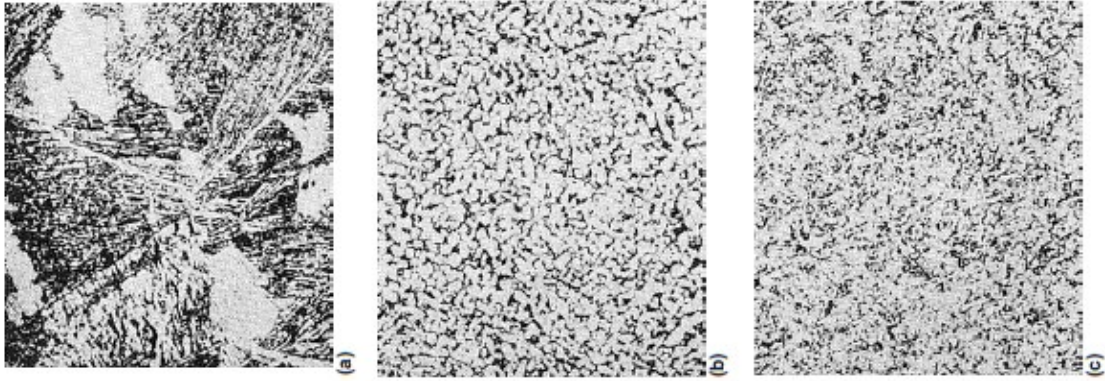


Figure 24: (a) Acicular alpha, (b) equiaxed alpha and intergranular beta, and (c) fine alpha-beta structure [66].

For an alpha-beta titanium, microstructure can be modified by varying both the temperature from which the sample is cooled, and the rate at which it is cooled. A sample air cooled from the beta region will exhibit a microstructure consisting of acicular alpha and intergranular prior beta, but water quenching from the same temperature will result in a martensitic alpha with beta and prior beta present. The same sample heated to within the alpha+beta region prior to air cooling will have coarser grains of primary alpha within a matrix of transformed beta and acicular alpha. Water quenching from the same temperature will eliminate transformed beta in favor of equiaxed primary alpha within a martensitic alpha prime matrix. Figure 25 shows the achievable microstructures for an alpha-beta titanium resulting from varying the cooling rate and initial temperature.

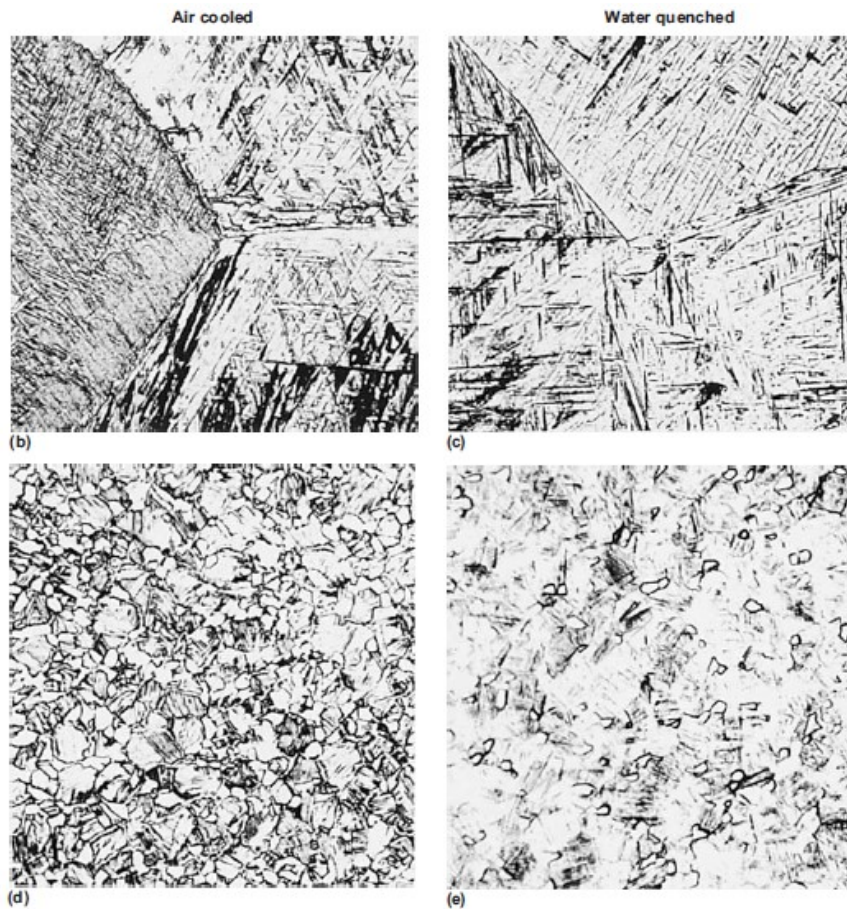


Figure 25: Microstructural possibilities in an alpha-beta titanium alloy. (b) acicular α with prior β grain boundaries, (c) martensitic α' matrix with β and prior β grains, (d) grains of primary α in matrix of transformed β containing acicular α (e) equiaxed primary α in a matrix of martensitic α' [66]

A common microstructural phenomenon in titanium alloys is known as a Widmannstätten structure. These structures are obtained through appropriate heat treatment and comprise a series of parallel alpha plates with a beta phase between them. These structures are formed through a martensitic transformation of existing beta upon rapid cooling [67]. Figure 26 shows the formation of Widmannstätten microstructure upon rapid cooling from above the beta-transus temperature.

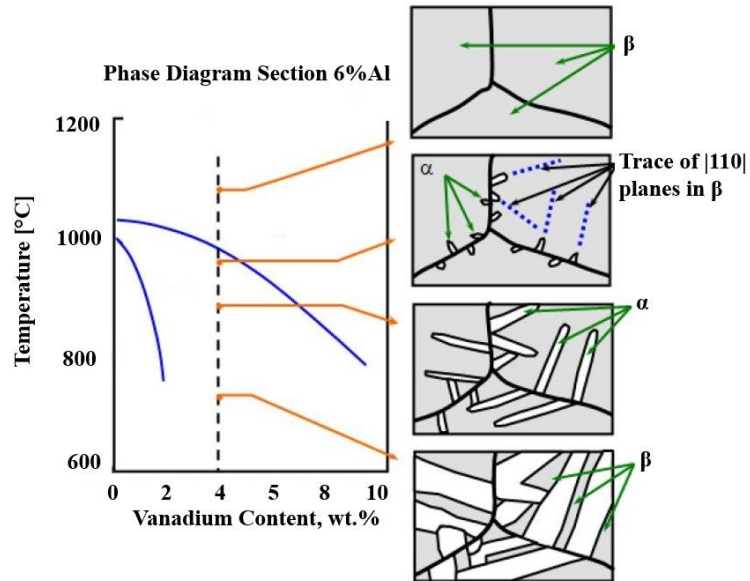


Figure 26: Formation of Widmannstätten microstructure upon rapid cooling from above the beta-transus temperature [68]

In addition to the influence on microstructure, several alloying elements are commonly used for their well understood effects on mechanical performance. Aluminum, tin, and zirconium have been shown to improve creep performance in the alpha phase [69,70]. Since these three elements are also isomorphous in both alpha and beta phase, they are present in most commercial titanium alloys. Iron, chromium, and manganese are often used in high beta alloys due to their effect on hardenability and heat treatability [71]. Nickel, palladium, and molybdenum are used to improve corrosion resistance in unalloyed titanium (alloys containing a small percentage of alloying elements) [72, 73].

1.3.1.2 Alpha Titanium Alloys

Alpha titanium alloys refer to those containing elements that increase the beta-transus temperature thus stabilizing the alpha phase to higher temperatures. They are utilized for their great weldability, good notch toughness, medium strength, and excellent performance at cryogenic temperatures. However, they are not heat-treatable, and therefore do not benefit from aging techniques. Alpha alloys feature high chemical resistance particularly

when exposed to jet fuel. Typical aerospace applications include turbine engine casings and aircraft frame components.

Although alpha titanium alloys exist, near-alpha titanium alloys are more commonly utilized in industry as they feature excellent high-temperature creep strength and oxidation resistance. Near-alpha alloys tend to contain minor amounts of the more ductile beta phase through the inclusion of trace concentrations of beta stabilizing elements. A commonly used near-alpha titanium is Ti-6Al-2Sn-4Zr-2Mo-Si (Ti-6242), which features excellent strength and creep properties up to 550C, corrosion resistance and weldability. Ti-6242 can be found in high performance automotive engine parts as well as in hot sections of turbine engines (discs, impellers, turbines) [74].

1.3.1.3 Beta Titanium alloys

Beta titanium alloys refer to systems containing elements that decrease the beta-transus temperature which encourages the formation of the beta phase at ambient. A significant benefit of these alloys is their heat treatability. As such, they are commonly forged in their solution-treated condition and subsequently aged to transform some of the beta into alpha. The alpha/beta microstructure formed by this solution treating and aging process can lead to improved strength over typical alpha-beta alloys due to fine dispersed alpha particles within a primarily beta matrix. Beta titanium alloys are commonly referred to as metastable beta titanium alloys due to the beta phase being metastable at temperatures below the beta-transus temperature. Industrially, Ti-15V-3Cr-3Al-3Sn sheet was used extensively on the B1-B bomber, because of its great formability and higher strength than Ti-6Al-4V [75]. Ti-10V-2Fe-3Al forgings were used on the Boeing 777, but in recent years the alloy Ti-5Al-5Mo-5V-3Cr (Ti-5553) has been developed which features a higher strength and a more robust processing window. Beta 21s has also been introduced which features improved high temperature performance over existing beta alloys and excellent resistance to the hydraulic fluids used in aircrafts.

1.3.1.4 Alpha-Beta Titanium Alloys

Alpha-beta titanium alloys have the most widespread use of any family of titanium alloys and exhibit a microstructure containing a mixture of alpha and beta phases at ambient. The main reason for alpha-beta alloys dominance is Ti-6Al-4V (Ti-64). This specific alloy accounts for approximately 45% of the total weight of titanium shipped and features attractive features of both alpha and beta titanium alloys including workability and fabricability/machinability. [76] These traits allow for a variety of mill products (large and small) and manufacturing of these raw products into complex components. In addition to combining the positive aspects of alpha and beta titanium alloys, the widespread industrial acceptance of Ti-64 has resulted in the operational experience and commercial availability necessary to ensure consistent economical usage. Although Ti-64 is excellent in many applications, its performance is significantly degraded above ~400C.

1.3.2 Titanium Alloys in AM

Although titanium offers significant advantages in many applications, one reason for its comparatively limited use is a high production cost. This is a result of the complex operations needed to extract metallic titanium underpinned by titanium's high reactivity with oxygen, nitrogen, and hydrogen. The combination of this cost premium with the wasteful nature of traditional subtractive manufacturing (machining) imparts a high buy-to-fly ratio in many scenarios; a common metric employed in the aerospace industry that relates the mass of the initial stock to the mass of the final part. High buy-to-fly ratios are undesirable as it means manufacturers are wasting/recycling more of the material than they are using.

One manufacturing technique that is being developed to minimize the wasted material is AM. Here, titanium alloys can be process in a near-net shape manner to greatly reduce the level of machining required, and in turn, material waste. Figure 27 shows an example of a typical starting stock in traditional machining (left) compared to a near-net-shape product produced through AM (right) and the resulting machined part (center). In this instance, the

buy-to-fly ratio was reduced from 30:1 with for the traditional manufacturing to only 1.7:1 with AM. In addition, residual powder feedstock used AM has also been successfully recycled [77].



Figure 27: Traditional cylindrical stock (left) compared to near-net-shape additively manufactured stock (right) and the resultant machined part (center) [78].

AM also offers unique opportunities with regards to biomedical applications. Titanium is an excellent material choice for implants due to its biocompatibility, high strength-to-weight ratio, and corrosion resistance. AM can produce physical structures that would either not be cost effective or impossible with traditional machining. One example is controlled surface porosity that can lead to improved bone in-growth of implants as well as increased mechano-transduction which improves implant performance and reduces the likelihood of the body rejecting it [79]. AM also offers the capability of producing unique implants based on a specific individual's needs. Figure 28 shows an additively manufactured titanium implant featuring controlled surface porosity to encourage implant uptake.



Figure 28: Spinal implant combining solid and porous structures, imitating calceous bone [80].

The bulk of commercial interest with regards to AM of titanium has centered around Ti-6Al-4V due to its widespread use and well understood mechanical and microstructural properties. Ti-64 has been successfully processed into effectively fully dense (>99% of wrought) manufactured parts in laser and electron beam DED [81-86] as well as powder bed fusion [87-89] systems. AM also offers the unique capability of repairing or adding features to existing components. For instance, researchers have shown that damaged titanium turbine blades could be rebuilt using DED technology. By utilizing a 3D model of the original part, the missing sections can be replaced and then machined to restore the original geometry [90]. This technique has also been applied industrially, receiving widespread acceptance for the repair of gas turbine components [91]. Figure 29 shows an example of a turbine blade repair using DED.

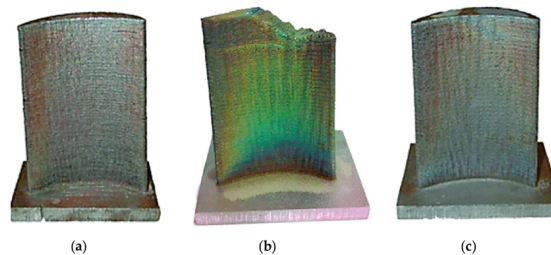


Figure 29: (a) original, (b) damaged, and (c) repaired turbine blade [92]

In terms of industrial examples of additively manufactured titanium parts, Spirit Aerosystems has been producing a Ti-64 door latch fitting used in the Boeing 787 using

their rapid plasma deposition (RPD) process since 2017. The part produced is identical to the original wrought+machined part, however AM has helped achieve a much lower buy-to-fly ratio. Figure 30 shows the as-printed stock and the final machined part.



Figure 30: Deposited near-net-shape stock (left) and final machined part (right) [93].

In the biomedical sector, custom titanium implants have been produced using SLM technology, with successful uptake by patients. One particularly large and complex example is a sternum/rib implant printed by Anatomics (Melbourne, Australia). This implant was designed to replace a portion of cancerous bone and had to be custom fit for the recipient [94]. Figure 31 shows the printed chest implant and a rendering of its placement in the recipients body.

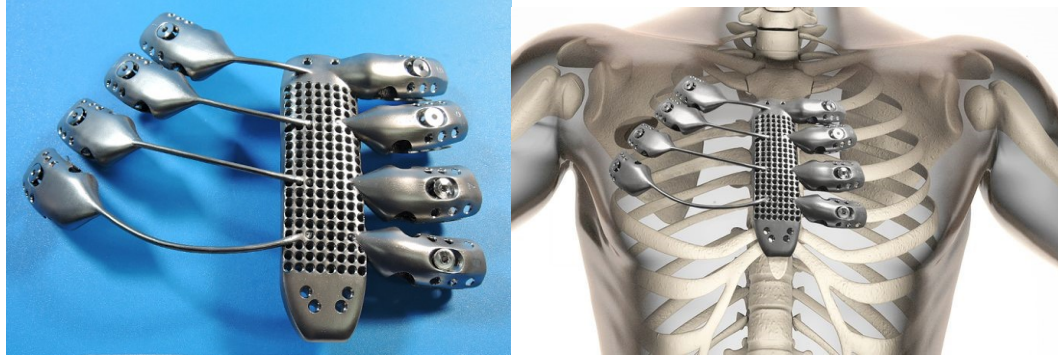


Figure 31: Additively manufactured titanium implant (left) and render of placement (right) [95]

Given the demonstrated success of Ti-64 in an AM context, researchers have begun branching out into other titanium alloys that offer unique advantages. For example, SLM technology has been developed to successfully manufacture components from the alpha-beta alloy Ti-6Al-7Nb [96], as well as beta alloys Ti2448 [97], Ti-13Nb-13Zr [98], Ti-6.5Al-3.5Mo-1.5Zr-0.3Si [99], Ti-1Al-8V-5Fe [100], and Ti-5Al-5Mo-4V-1Cr-1Fe [101]. EBM has also been used to process Ti2448 [102], and wire arc additive manufacturing has successfully processed Ti-3Al-8V-6Cr-4Mo-4Zr [103], Ti-45Al-2.2V [104] and Beta C [105]. The alpha and near-alpha titanium alloy Ti-6Al-2Zr-Mo-V [106] and Ti-6Al-2Sn-4Zr-2Mo (Ti-6242) [107] have both been processed using selective laser melting.

2 RESEARCH OBJECTIVE

This study is part of a long-term initiative to develop novel titanium alloys for use in laser DED. One purpose of this specific phase of the study was to establish a baseline for the industrial workhorse Ti-64, and to determine equipment variability within DED processing. The primary measurements of interest were dimensional accuracy, density, hardness, tensile properties, thermal behavior (differential scanning calorimetry) and microstructure (scanning electron microscope). With this baseline established, a secondary initiative was engaged wherein other industrially relevant titanium alloys from different alloy families were processed to examine their potential viability for DED AM. Ti-6242 and Beta-21s were the alloys of choice, representing a near-alpha and beta titanium respectively. After initial experimentation to ensure the alloys were buildable, key process parameters (laser power, traverse rate, hatch spacing, layer height and powder feed rate) were strategically varied to determine the optimal process parameters. Following process optimization, samples were heat treated to ensure the microstructural change was in line with wrought samples. The key areas of assessment were density, micrography, heat treatment response and tensile properties.

3 INTER-VENDOR STUDY OF DIRECTED ENERGY DEPOSITION BUILD QUALITY USING A COMMERCIAL TI-64 POWDER

N.A. Gosse¹, M.D. Harding², D.P. Bishop³, I.W. Donaldson⁴

1 – Graduate Student, Dalhousie University, Halifax, Nova Scotia, Canada

2 – Program Manager, Tronosjet, Charlottetown, Prince Edward Island, Canada

3 – Professor, Materials Engineering, Dalhousie University, Halifax, Nova Scotia, Canada

4 – Director, Advanced Engineering, GKN Sinter Metals, Conover, North Carolina, USA

Status: Under review by HI-AM network scientific advisory committee for public release.

The following experimental procedures, results, and discussion were primarily completed by N.A. Gosse. Secondary authors aided in data acquisition/review, manuscript editing, and/or project supervision.

Abstract: This research sought to compare the manufacturing capabilities of several vendors of directed energy deposition (DED) equipment in the context of additive manufacturing. Gas atomized Ti-64 powder was utilized in all instances as it maintains a high relevance to industrial practice and is readily applicable in DED processing. A single commercial lot of Ancor Ti-64 powder was secured for this purpose, characterized, and then distributed amongst multiple OEMs of DED equipment. Vendors were also given a 3D model and dimensioned drawing of the desired test build geometry. Upon receipt of the completed builds, dimensions of interest were measured using a 3D coordinate measurement machine and compared to the provided model. Builds were also compared based on a range of metallurgical assessments. These included the acquisition of data on hardness, density (MPIF Standard 42), and tensile properties (ASTM E8M). In addition, optical micrography, scanning electron microscopy, and differential scanning calorimetry were utilized to characterize microstructural features of each build.

Keywords: Additive manufacturing, Alpha-beta titanium, Directed energy deposition (DED), Titanium, Ti-64, Ti-6Al-4V

3.1 Introduction

Directed energy deposition (DED) is a form of additive manufacturing that utilizes a high energy density laser to generate a molten pool, into which metal feedstock is directly deposited. In early applications this feedstock was in the form of a wire, analogous to wire-fed welding. However, in 1995, Sandia National Laboratories developed a process in which metal powder feedstock was fed directly into the melt pool. This technology, known as “Laser Engineered Net Shaping” (LENS) is considered the first commercial DED system [108]. The use of powder feedstock allows for alloying within the melt pool, enhanced material flexibility, and improved dimensional accuracy over wire feedstock, while sacrificing feedstock capture efficiency (amount of feedstock that is successfully captured in the melt pool) and carrying with it a higher material cost. Due to these properties, DED with a powder feedstock is preferred when a near net shape product is desired, whereas wire may be used for larger geometries or as part of a manufacturing process containing subtractive manufacturing as the means of achieving the desired final dimensions [109].

Ti-6Al-4V (Ti-64) is a $\alpha+\beta$ titanium alloy that exhibits excellent corrosion resistance, a high strength to weight ratio and high biocompatibility when directly contacting bone and tissue [110]. These characteristics make Ti-64 the most commonly used titanium alloy in the aerospace and biomedical sectors [111]. Although Ti-64 has proven incredibly useful for these industries, its high cost, high reactivity, low thermal conductivity, and tendency to harden when heated make it difficult and expensive to machine which has limited its applications.

Using DED with Ti-64 powder, it is possible to create near net shape components, minimizing the amount of machining required to achieve the final component and allowing Ti-64 to be employed in high shape-complexity applications despite its poor machinability. Literature reviews have been prepared showing the reduced environmental impact in the context of manufacturing sustainability [112]. By minimizing the amount of wasted

material, the high material cost of titanium manufacturing is reduced, which can allow for production of parts that may be monetarily impractical using traditional manufacturing processes. Additionally, the overall environmental impact of additive manufacturing was shown to be less than subtractive manufacturing according to a life cycle assessment meta-analysis [113].

With the growing popularity and industrial interest surrounding DED, the number of vendors of producing DED equipment has grown as well. As such, the objective of this research is to examine and compare the processing capabilities of several of these vendors and determine the capabilities of each in the context of titanium DED processing. By comparing these results, the amount of variation between different styles of DED equipment and vendor-determined process parameters can be quantified.

3.2 Materials and Methodology

The powdered material utilized in this research was AncorTi powder supplied from GKN Hoeganaes. The prealloyed powder was produced by Electrode Induction-Melting Inert Gas Atomization (EIGA) and met the composition specification for Grade 5 Ti-64 in accordance with ASTM B348-13 [114]. The flowability of the powder and apparent density are shown in Table 1 Table 4.

Table 1: Flow rate and apparent density of starting Ti-64 powder.

Test	Value
Hall Flow	21.8 s/50g
Apparent Density	2.57 g/cc

Impurities in the form of adsorbed/absorbed gas on the powder was also measured, as shown in Table 2.

Table 2: Impurity contents of the starting Ti-64 powder

	O	H	N	C
Measured	0.188	0.0018	0.027	0.024
Grade 5 Standard	0.200	0.0150	0.050	0.080

Chemical analysis was completed by inductive coupled plasma optical emission spectroscopy (ICP-OES) . The resultant assay is shown in Table 3.

Table 3: Measured concentrations of alloying elements and impurities in the starting Ti-64 powder.

	Ti	Al	Cr	Fe	Ni	V
Measured	89.962	6.030	0.010	0.225	0.018	3.754
Grade 5 Standard	87 – 91	5.5 – 6.75	-	0 – 0.4		3.5 – 4.5

The powder featured a narrow particle size distribution (Figure 32) ($D_{10} = 52 \mu\text{m}$ and $D_{90} = 102 \mu\text{m}$) and a highly spherical morphology, making it appropriate for DED processing due to its high flowability and limited interparticle friction. Figure 1 shows the particle size distribution and SEM image of powder morphology.

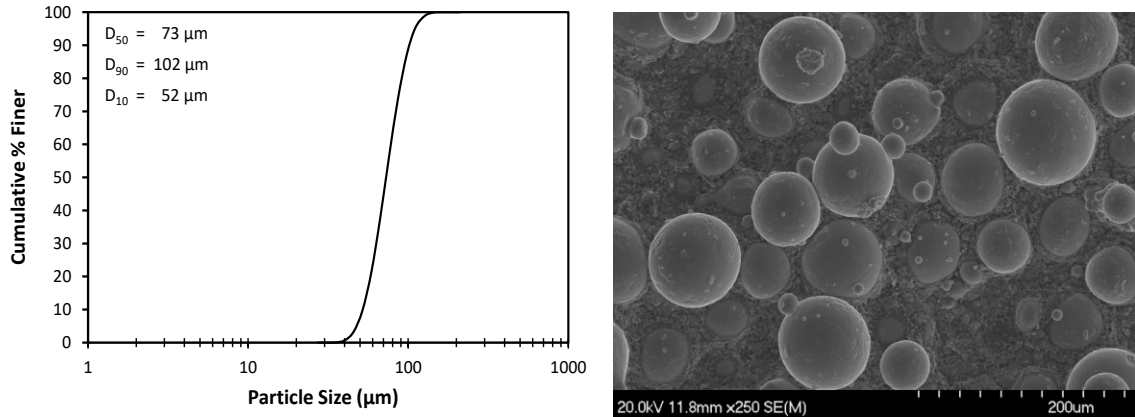


Figure 32: (a) Particle Size Distribution and (b) Powder Morphology of the as-received Ti-64 powder.

To establish baseline data on the Ti-64 powder of interest, a build configuration was designed in AutoCAD and sent to a series of companies that produce DED equipment. These are henceforth denoted as Vendors A, B, and C. Details on the build design are presented in Figure 33.

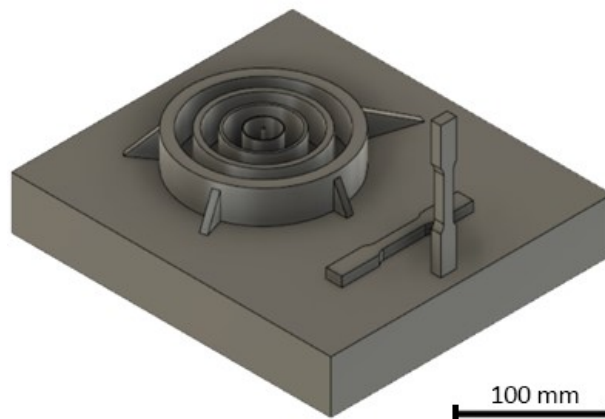


Figure 33: 3D model distributed to vendors consisting of test geometry and tensile specimens.

The design included a series of concentric rings with progressively larger wall thickness, and a series of angled columns with systematically different sloped profiles connecting at

the outermost ring. Vertical columns (75 mm tall with a 10 mm × 10 mm cross section) were also built at each vendor so that tensile properties could be measured in a direction transverse to the build layers; the orientation likely to present the most conservative property values. Each vendor was also supplied with a 25mm thick build plate of wrought Ti-64 (annealed), and identical Ti-64 powder. Regarding the latter, a 50kg sample of the powder was extracted from a singular commercial lot and distributed to the vendors for build purposes. Each vendor was well-versed in the processing of Ti-64 and maintains unique DED technology. As such, each vendor was asked to produce the build under the conditions known to be ideal for Ti-64 powder in their respective system from prior studies. Upon receipt of the builds, and prior to any material characterization, all builds were stress relieved according to SAE Aerospace Material Standard AMS 2801B to ensure that all samples were tested in a stress relieved condition.

Figure 34 shows the builds produced by each vendor. In terms of qualitative visual inspection, vendor A had the poorest quality with inconsistent layer thicknesses and evidence of overbuilding at the start/stop point of each layer. Vendor B had considerably better visual quality with consistent layer thicknesses and sharp transition between the top and sides of the rings. Vendor C showed the highest visual quality with consistent layer thicknesses and higher resolution resulting from thinner layers. Additionally, the inner rings of Vendor C had sharper transitions from the top to the sidewalls, without any bulging or filleting.

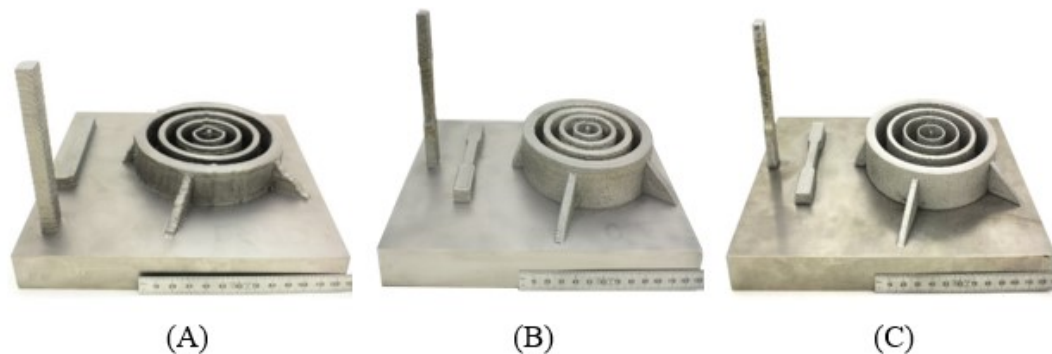


Figure 34: As-received builds produced by vendor A, B and C.

Characterization of the builds included dimensional inspection and metallurgical analysis. For the former, builds were assessed with a three-dimensional coordinate measurement machine. Here, the height and wall thickness of each ring was measured at 5 locations (72° between each point). These averages were then compared to the intended dimensions as defined by the CAD model to quantify the dimensional accuracy in terms of percent difference. In addition to the macroscopic dimensional accuracy, samples were examined using laser confocal microscopy to quantify the average surface roughness. This surface roughness relates to the quality of individual layers and the consistency of the distribution of layers.

For the latter, data on the density, hardness, microstructure, tensile properties, composition, and thermal behavior were acquired from the vertical and horizontal bars once removed from the build plate and milled to remove any as-built surface roughness. To measure density, an Archimedes type of approach was utilized, as defined by MPIF standard 42. Hardness was measured on each bar 5 times in the Rockwell C scale using a Wilson Instruments Rockwell 2000 Hardness Tester. For microstructural studies, samples were mounted in a conductive Bakelite using a Buehler SimpliMet 3000 automatic mounting press. Samples were oriented such that the exposed surface was perpendicular to a prescribed build direction, allowing for examination of layer adhesion and effects of repeated heating during manufacturing. Mounts were then polished using a 1200 grit Silicon Carbide pad, a $15\mu\text{m}$ diamond suspension, and finally, a $0.05\mu\text{m}$ colloidal silica suspension. All polishing steps were completed using a Struers Tegramin autopolisher. After obtaining micrographs of the polished and unetched microstructure using an optical microscope, each specimen was etched with a solution of 0.5% hydrofluoric acid. The etched structures were examined using optical and scanning electron microscopy.

To quantify tensile properties, each bar was machined into a flat dog bone-type test specimen compliant with ASTM E-8M. Bars were loaded at a rate of 5MPa/s to fracture in an Instron model 5594-200HVL hydraulic load frame equipped with a 50kN load cell. A calibrated epsilon (model 3542) extensometer with a 25mm gauge length was attached to

each specimen to facilitate accurate strain measurements. All numerical measurements for a vendor/orientation combination were averaged to obtain a singular value for comparison purposes. Fracture surfaces were examined using a Hitachi S-4700 Cold Field Emission Scanning Electron Microscope (SEM). Following fractography, one grip end of each bar was sectioned and manually polished using a 360-grit silicon carbide polishing pad. These prepared samples were mounted in zero diffraction holders and examined using a Bruker D8 Advance x-ray diffractometer. Additionally, a sample of powder from the same commercial lot as the builds was examined using the same XRD parameters to allow for comparison. A second smaller portion of the grip end was examined using differential scanning calorimetry. One sample from each vendor was heated to 1200°C and then cooled to room temperature. Afterward, a single representative sample was reheated to 1200°C to determine if the initial heating had homogenized the sample. In addition to the grip end samples, a sample of wrought Ti-64, and a sample of the distributed Ti-64 powder were exposed to the same heating conditions to allow for comparison.

3.3 Results and Discussion

3.3.1 Dimensional Accuracy

Upon receiving the finished builds from each vendor, measurements were taken of the various features to determine how accurately each vendor was able to recreate the provided CAD model. Figure 35 shows the percent difference between the angle of columns achieved by the vendors and the desired angle in the CAD model. All vendors were able to recreate these angles within a reasonable margin (<15% percent difference). However, Vendor C was able to recreate the desired angles most accurately, with an average percent difference of 2.31%, followed by Vendor A (5.40%) and finally Vendor B (7.47%).

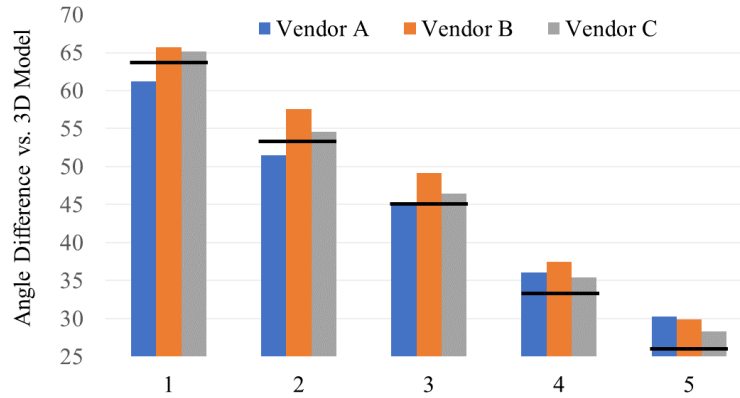


Figure 35: Difference in angle from 3D model, the black bar indicates the desired angle

Although the overall angles were roughly the same, there was a noticeable difference in the quality and continuity of the angled columns. The angles were calculated using the measured length and height of the angled columns and Pythagorean theorem, which assumes that the columns are triangular. Figure 36 shows a comparison of angle 4 for the three vendors. The quality difference between the vendors is clear, with Vendor C having the smoothest column, followed by Vendor B then Vendor A, which disagrees with the angular percent difference.

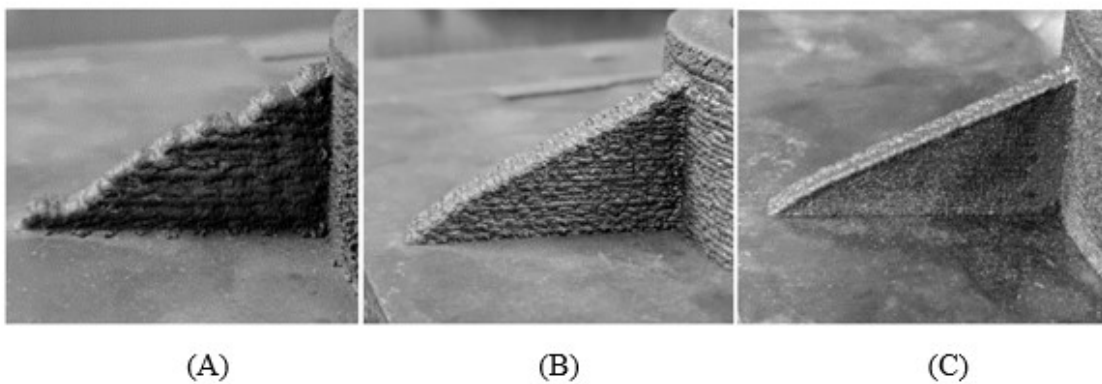


Figure 36: Comparison of angled column 4 for (a) Vendor A, (b) Vendor B, and (c) Vendor C.

In addition to the angled columns, the dimensions of the concentric rings were also of interest. The purpose of the concentric rings was not only to compare the vendor’s ability to accurately reproduce the CAD model, but also to determine the minimum thickness that each machine was capable of producing with optimal parameters. Figure 37 shows the percent difference in the thickness of each ring compared to the provided CAD model. None of the vendors were capable of accurately reproducing the first ring with the desired thickness of 0.5 mm. Vendor C was able to get the closest, achieving a minimum thickness of 1.44 mm for ring 1. Comparing average percent difference across all rings and the center post, vendor C was the most accurate (45%) followed by vendor A (162%) and vendor B (189%). These results show that despite Vendor B’s build having better quality visually, it was less dimensionally accurate. Depending on the desired application, and intended post-process machining, either build may be seen as appropriate.

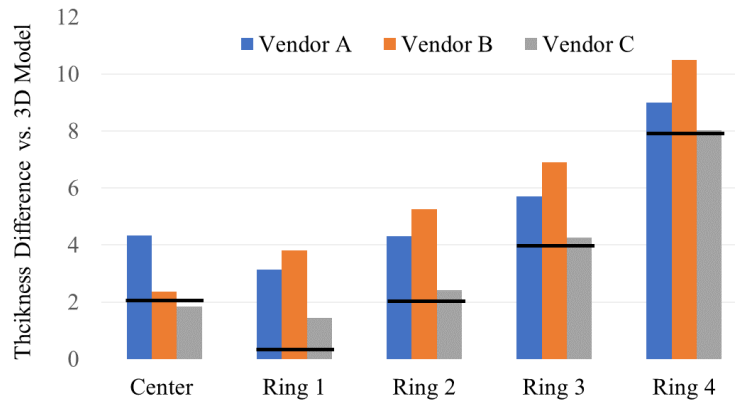


Figure 37: Thickness of Rings (% difference from CAD model).

Figure 38 shows a comparison of percent difference between the height of the concentric rings and center post for each vendor compared to the distributed model. The difference in the height of these features represents the vendor’s ability to accurately control the depth of the melt pool and resulting layer heights and accounting for these layer heights when building to the desired dimensions. Comparing the average percent difference over all concentric rings and the center post, vendor C was the most accurate (3%) followed by vendor A (6%), and finally vendor B (96%) which was consistently overbuilt.

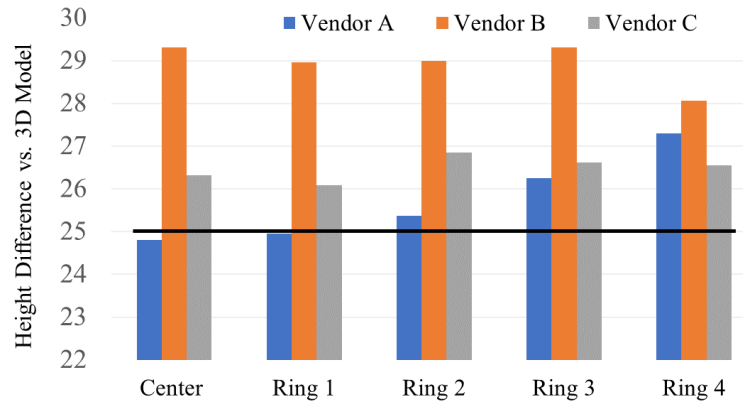


Figure 38: Height of Rings (% difference from CAD model).

In addition to the dimensional accuracy measurements, the surface roughness was also determined using laser confocal microscopy. The extremes are represented in Figure 39, looking side-on at the layers, revealing the layer lines. From observing these surface maps, there is a clear pattern of repeating lines visible in the sample on the right. Conversely, the sample on the left has a rough surface but no clear repeating patterns indicative of layer resolution. Performing a multiline surface analysis on both samples confirmed that the sample on the left had a lower roughness ($R_a=42$) than the sample on the right ($R_a=51$)

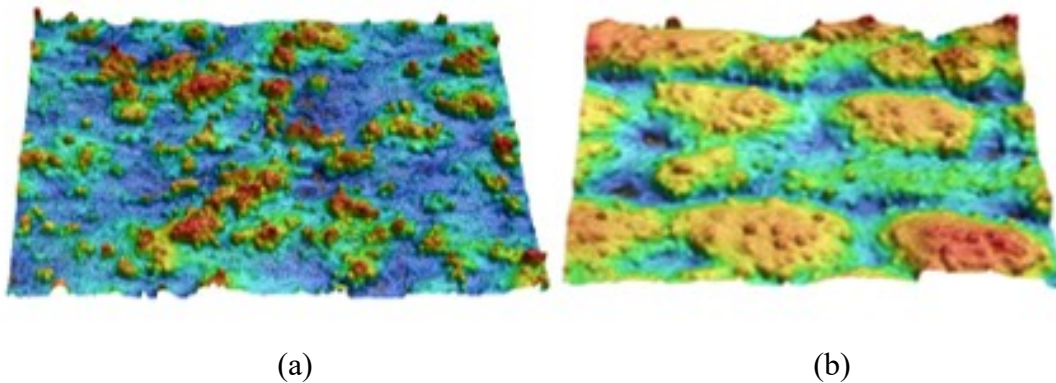


Figure 39: Surface roughness maps of (a) Vendor C and (b) Vendor A

3.3.2 Density and Hardness

Table 4 shows the hardness data collected from the tensile bars prepared by each vendor. Since DED involves repeated heat exposure, there is the potential for vendor parameters (such as excess heat input, or presence of oxygen) to impact the hardness of the final product. Hardness was found to be consistent between all vendors for z and x-direction built samples. The x-direction samples were slightly harder (42 HRC) than the z-direction samples (39 HRC). The measured hardness for both the x-direction and z-direction built samples are within a reasonable margin of comparable wrought Ti-64 (41 HRC).

Table 4: Average hardness from tensile bars fabricated by each vendor

Vendor	Build Orientation	Hardness (avg.)
A	Z-Direction	39
	X-Direction	42
B	Z-Direction	39
	X-Direction	42
C	Z-Direction	39
	X-Direction	42

Table 5 shows the density data for the tensile bars provided by each. The difference in densities can be attributed to the porosity inherent in DED. Some of the porosity is a result of gas entrapped in the Ti-64 powder by the atomization process. This gas-induced porosity tends to survive localized melting, resulting in porosity in the final product. Additionally, particles with surface satellites can impede the flowability through the feed nozzle resulting in a non-homogenous consolidation and a decrease in density. Since all vendors were provided with powder from a single commercial lot, this gas-induced porosity should be consistent between builds, meaning differences in density can be attributed to process differences rather than differences in the powder.

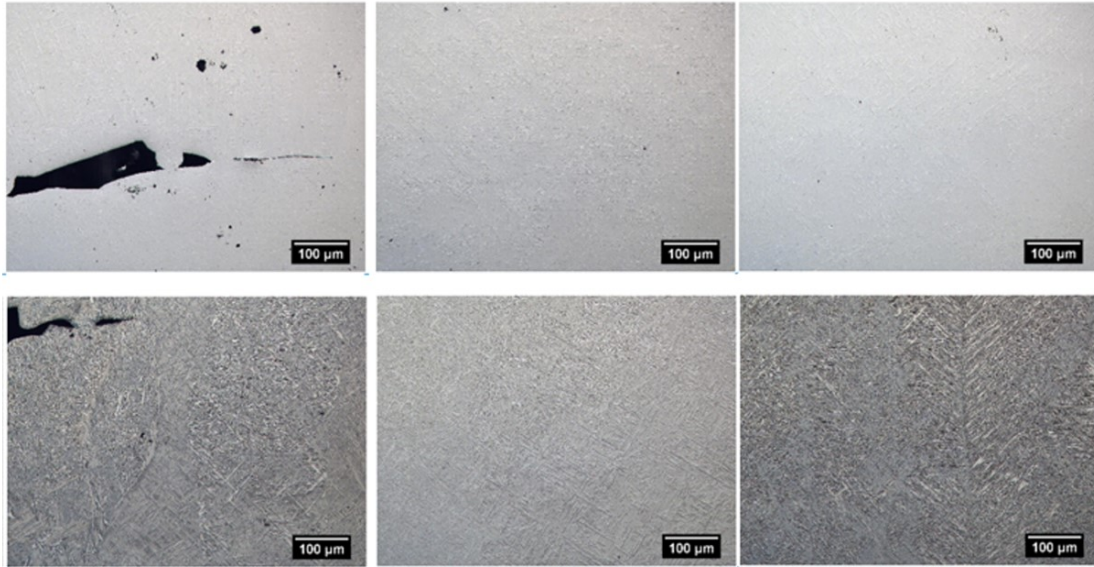
Table 5: Average density from tensile bars fabricated by each vendor.

Vendor	Build Orientation	Density (g/cm ³)
A	Z-Direction	4.376
	X-Direction	4.412
B	Z-Direction	4.408
	X-Direction	4.417
C	Z-Direction	4.404
	X-Direction	4.411

For the z-direction built samples, both vendor B and C were comparable to wrought Ti-64 (4.43 g/ cm³) with percentages of 99.5% and 99.4% respectively. Vendor A’s z-direction built sample was noticeably less dense than wrought Ti-64 with a percentage of 98.77%. For the x-direction built samples, densities were all comparable to wrought Ti-64, with percentages of 99.7%, 99.6% and 99.57% for vendors A, B, and C respectively. The x-direction builds likely have less porosity due to the decreased number of layer-layer interfaces resulting in fewer opportunities for parameter induced porosity.

3.3.3 Microstructure

Images of the typical microstructure observed in the z-direction builds are shown in Figure 40. A relatively high level of residual porosity and regions demonstrating a lack of inter-layer fusion were apparent in the build constructed by Vendor A. The density was higher in builds fabricated by Vendors B and C although the presence of micropores was noted in both, likely resulting from minute infrequent porosity in the starting powder. Etching revealed that the microstructures were somewhat complex as they appeared to contain martensitic α' (acicular/plate-like α -Ti). These complex martensitic microstructures are expected when cooling Ti-64 rapidly as is the case in DED.



(A)

(B)

(C)

Figure 40: Unetched (top row) and Etched (bottom row) microstructures observed transverse to the build direction of z-direction built samples of (a) Vendor A, (b) Vendor B, and (c) Vendor C, showing the variation in porosity.

Figure 41 shows the unetched and etched microstructures for the x-direction built samples. There is a distinct difference in the amount of process-induced porosity in the x-direction built samples. This can be explained by the x-direction built samples being shorter, meaning they have fewer layers than the z-direction built samples and therefore less opportunity for interlayer porosity which accounts for most of the porosity in the samples. The etched microstructures look comparable to the z-direction built samples, consisting of primarily martensitic α' (acicular/plate-like α -Ti).

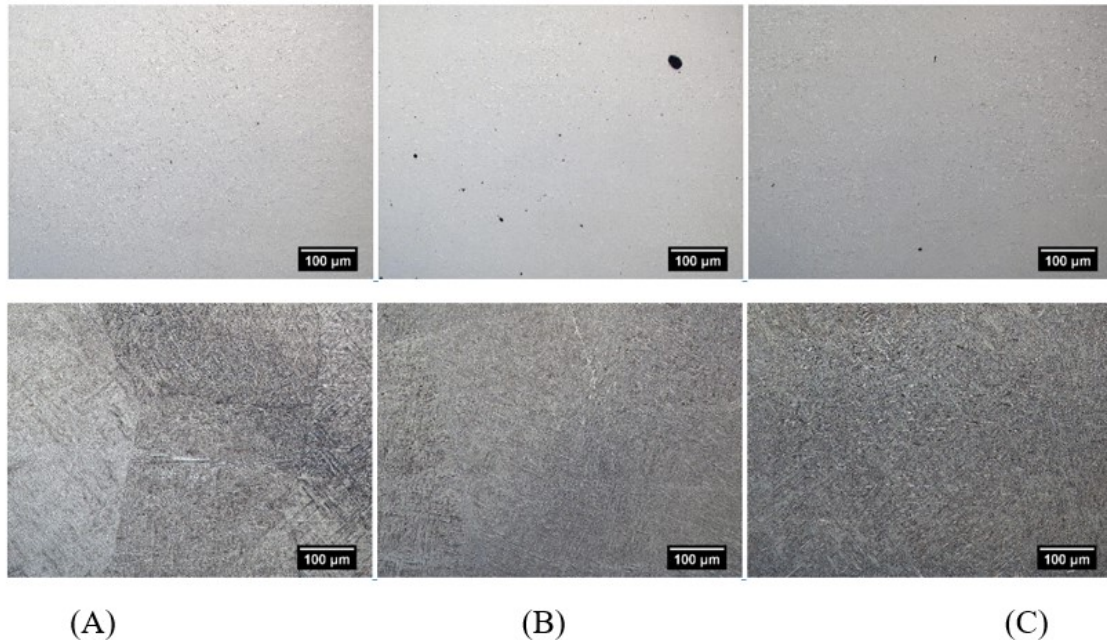


Figure 41: Unetched (top row) and Etched (bottom row) microstructures observed transverse to the build direction of x-direction built samples of (a) Vendor A, (b) Vendor B, and (c) Vendor C, showing the variation in porosity.

The average yield strength, ultimate tensile strength and percent elongation of each build are summarized below, comparing the x and z-direction built samples. The z-direction built samples showed consistently lower ultimate tensile strengths and yield strengths. This came as no surprise as many metallic AM materials demonstrate inferior properties when loaded in a direction that is normal to the build plane, resulting from crack formation at the interface between layers, ultimately causing delamination between layers as opposed to material failure. Lack-of-fusion pores present between layers exacerbates this effect due to the sharp edges of these pores aligning with the layers and concentrating local stresses. Vendor A showed the poorest mechanical properties for the z-direction build, with very low strengths as well as poor elongation. This result is owed to the clear delamination of layers as is evident from the fractography that follows.

Figure 42 shows the ultimate tensile strengths for the x and z-direction built samples for each vendor. The x-direction built samples showed consistently higher ultimate tensile strengths than z-direction built samples. All vendors were able to produce x-direction built samples with strengths comparable to wrought (900 MPa), however only vendor B and C were able to produce successful z-direction built samples.

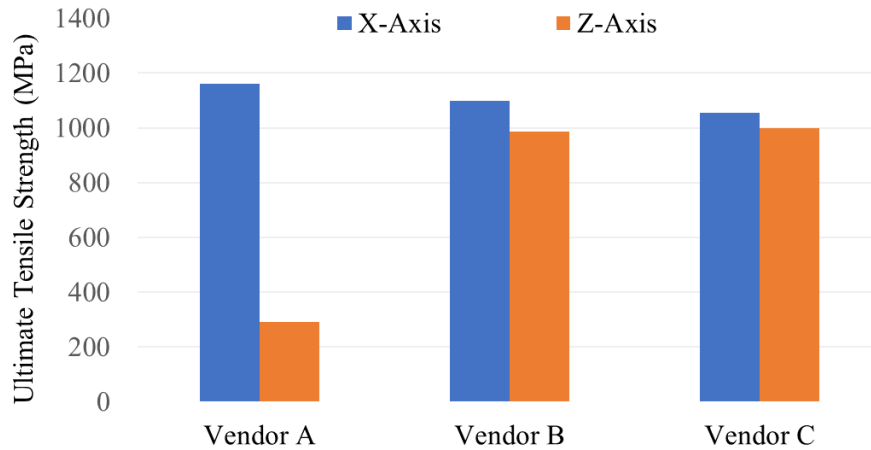


Figure 42: Ultimate Tensile strength of vendor-built samples.

Figure 43 shows the yield strengths of the x and z-direction built samples from each vendor. The results here are comparable to those for the ultimate tensile strength as expected, with x-direction built samples having consistently higher yield strengths than z-direction built. One distinct difference is that the yield strength for vendor C is lower than vendor B despite having very similar ultimate tensile strengths.

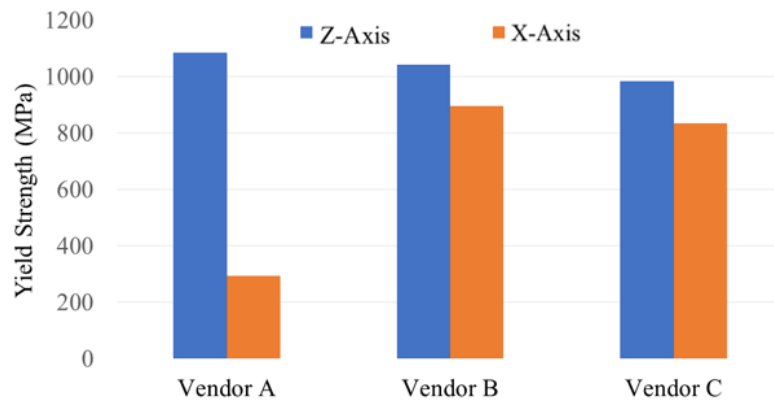


Figure 43: Yield strength of vendor-built samples.

Figure 44 shows the percent elongation of the x and z-direction built samples from each vendor. These results show an inverse trend to the strength data above, the x-direction built samples had lower percent elongation than the z-direction built samples. The percent elongation of the z-direction built sample from vendor A indicates a clear delamination failure, whereby the layers completely detached without stretching, mimicking brittle failure.

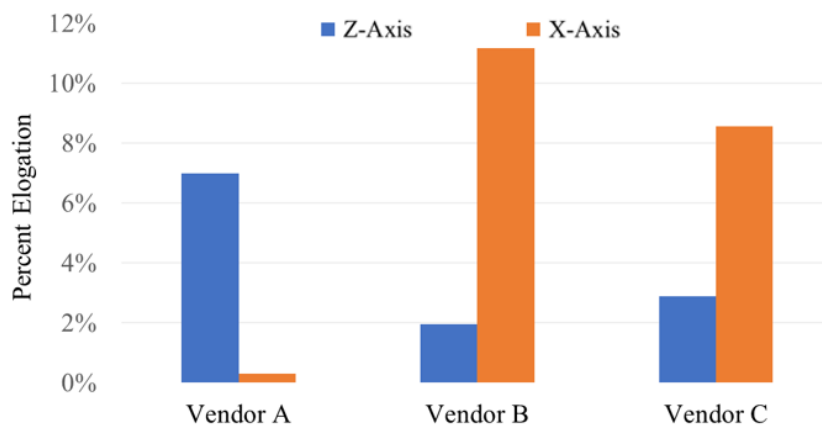


Figure 44: Percent elongation of vendor-built samples.

When comparing the mechanical properties above to the properties of wrought Ti-64, the DED samples had higher strengths overall (~200 MPa higher for x-direction built and ~100 MPa higher for z-direction built) and percent elongations ranging from equal to wrought (10%) significantly lower than wrought (2%). The improved strength can be attributed to the microstructure consisting of primarily martensitic α' , as opposed to the typical large primary alpha plates and transformed beta. With regards to the lower percent elongation, a small number of lack-of-fusion pores as well as spherical pores present in the starting powder serve as stress concentrators that result in poorer ductility.

Following tensile, fractography was performed on select samples in order to examine the fracture mechanisms that were present. The two fracture surfaces observed were clear lack of layer adhesion (a) or semi-ductile fracture (b). Lack of layer adhesion was evident from the presence of unmelted powder on the fracture surface, and small areas of cups and cones. Conversely, the semi-ductile fracture surfaces featured cups and cones throughout the entire surface which is consistent with wrought Ti-64 fracture surfaces.

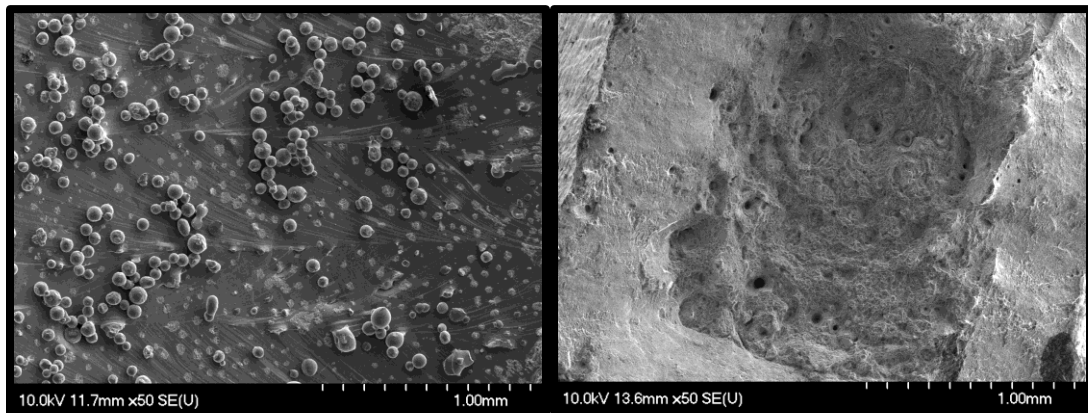


Figure 45: Fracture surfaces of (a) Vendor A and (b) Vendor C z-direction built samples

3.3.4 Differential Scanning Calorimetry

Several aspects of the x-direction builds were examined using DSC. Firstly, Figure 46 shows the heating and cooling curves for the various builds from each vendor. All samples

showed comparable shape and area under their curves, suggesting that there is negligible difference in the extent of inhomogeneity of solute between vendors.

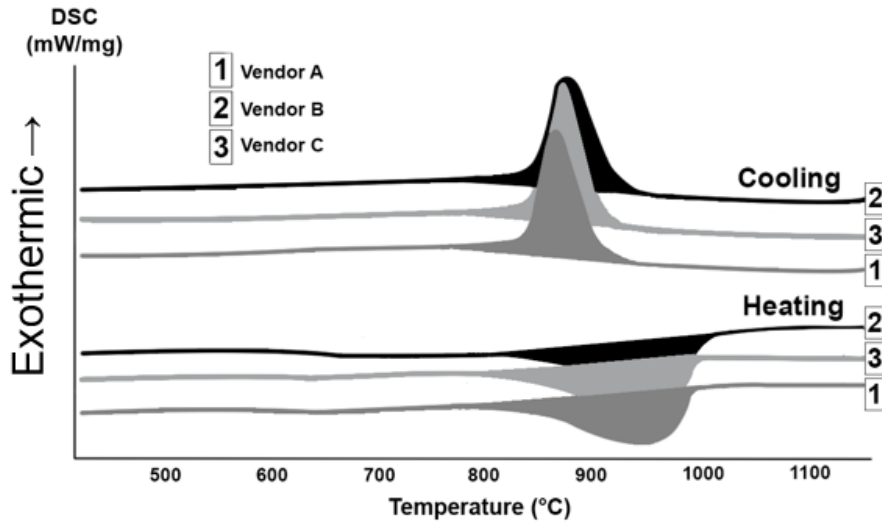


Figure 46: Heating and cooling curves for x-direction built DED samples from each vendor.

Figure 47 shows the heating and cooling curves for a DED built sample that was heated to 1200°C, allowed to cool, and then reheated. There is no significant difference between the first and second runs, suggesting that the microstructure is stable throughout this temperature range. Therefore, the thermal stability of the DED Ti-64 is comparable to wrought samples in terms of homogeneity and microstructure.

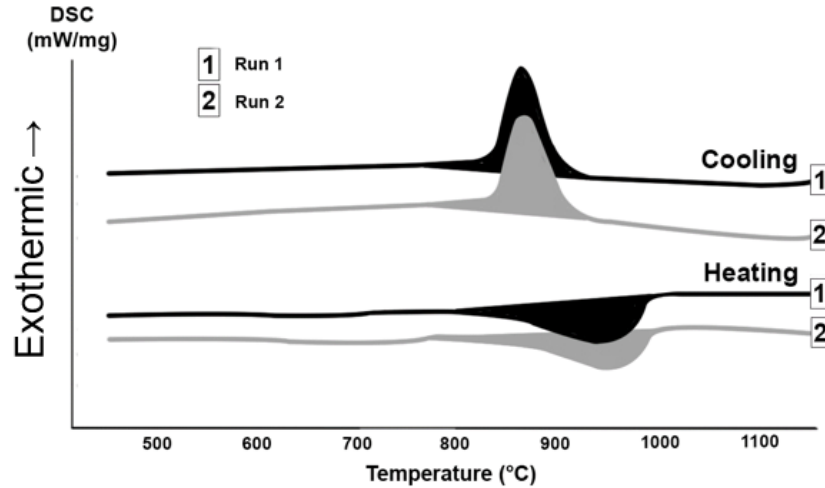


Figure 47: Heating and cooling curves for an x-direction built sample undergoing reheating.

3.4 Conclusions

Based on the analysis of the three builds, it was observed that the dimensional accuracy of the builds featured considerable variation, with all three vendors being unable to reproduce the smallest features (the 2 mm diameter center column and 0.5 mm thick first ring). Overall, vendor C was able to most accurately reproduce the build, measurably better than vendors A and B. Vendors B and C were able to produce high density x and z-direction samples, whereas vendor A's z-direction build showed the poorest density, with a high abundance of residual pores and clear interlayer lack of fusion defects. The hardnesses of all samples were comparable, with a slight increase in the x-direction built samples. The microstructures were as-expected for additively manufactured Ti-64, consisting of martensitic α' (acicular/plate-like α -Ti). The tensile properties of x-direction samples were consistent across vendors and comparable to wrought Ti-64. The z-direction samples for vendor B and C were slightly below wrought, vendor A was significantly below wrought showing very poor mechanical performance resulting from lack of interlayer fusion. Despite similar UTS and YS results, there was a significant variation in the ductility of x-direction built samples. DSC curves showed no distinct difference between vendors and

indicated microstructural thermal stability similar to wrought Ti-64 when exposed to repeated heating to 1200°C.

Acknowledgements

The authors would like to graciously acknowledge the funding support provided by the Natural Sciences and Engineering Research Council of Canada (NSERC) strategic partnerships grant for networks entitled “NSERC Network for Holistic Innovation in Additive Manufacturing (HI-AM)”.

4 DIRECTED ENERGY DEPOSITION PROCESSING OF NEAR-ALPHA AND BETA TITANIUM ALLOYS TI-6242 AND BETA-21S

N.A. Gosse¹, I.W. Donaldson², D.P. Bishop³

1 – Graduate Student, Dalhousie University, Halifax, Nova Scotia, Canada

2 – Director, Advanced Engineering, GKN Sinter Metals, Conover, North Carolina, USA

3 – Professor, Materials Engineering, Dalhousie University, Halifax, Nova Scotia, Canada

Status: Under review by HI-AM network scientific advisory committee for public release.

The following experimental procedures, results, and discussion were primarily completed by N.A. Gosse. Secondary authors aided in data acquisition/review, manuscript editing, and/or project supervision.

Abstract: The objective this research was to determine the optimal process parameters for 2 titanium alloys of different compositions in laser powder-fed additive manufacturing (LPF-AM). The two alloys chosen for examination were Ti-6242 (near-alpha alloy) and Beta 21-s (beta alloy). These alloys were chosen for their widespread use in traditional manufacturing and potential for use in additive manufacturing. The same experimental methods were employed for each alloy with different variable ranges. Experiment 1 varied the laser power and traverse rate, with the sample density (MPIF Standard 42 and optical micrography) as the dependent variable. These results were used to narrow the range of variables in a second experiment that varied laser power, traverse rate, hatch spacing, layer thickness and powder feed rate. The optimal parameter set determined through experiment 2 was then used to prepare tensile samples according to ASTM-E8 that were heat treated according to common industrial heat treatments in order to obtain mechanical properties. Both alloys were successfully processed, producing samples with densities greater than 99.8% of theoretical density. Both alloys responded favorably to heat treatments, with resultant microstructures comparable to wrought. Mechanical properties were near wrought in terms of tensile strength but suffered from decreased ductility.

Keywords: Beta-21s, Ti-6242, Alpha, Near-Alpha, Beta, Titanium, Additive manufacturing, Directed energy deposition, near net-shape

4.1 Introduction

Directed energy deposition (DED) refers to the freeform fabrication of a material using a powder or wire feedstock directed into the focal point of a high energy heat source (laser, arc, or electron beam) forming a precise melt pool [115]. By manipulating the deposition head and/or build plate the movement and solidification of this melt pool can be used to form desired geometries. Due to the freeform nature of the process, DED is a near net shape technology, creating a finished part that requires minimal post process machining and a reduced amount of wasted material. When compared with other additive manufacturing (AM) processes, DED offers a faster deposition rate at the cost of increased heat input and lower print resolution [109]. Industrially, DED is principally utilized in the repair of components such as turbine blades and worn shafts [116]. In both instances, excess material is deposited onto the surface to allow for post process machining to the final geometry.

In the context of titanium alloys, significant effort has been focused on Ti-6Al-4V (Ti-64) which is the workhorse of the titanium industry. Ti-64 is an α -beta titanium alloy that offers an excellent combination of density, strength, fatigue, and corrosion resistance [117]. Although it is a well-balanced system that is utilized in many applications, there are opportunities for alternative titanium alloys that provide better specific properties for certain scenarios. One example is Ti-6Al-2Sn-4Zr-2Mo (Ti-6242); a near- α titanium alloy that offers excellent strength and ductility along with improved high temperature creep and fatigue performance compared to Ti-64. Ti-6242 is functional up to approximately 550°C whereas Ti-64 generally becomes unusable above 350°C [118]. Ti-6242 is currently used in lightweight hot zone applications in aerospace, such as turbine components, afterburner components and airframes. Notably, it was the first titanium alloy to get SAE Aerospace Material Specifications (AMS) approval specifically for use with AM [119].

The bulk of AM research for Ti-6242 has been focused on laser powder bed fusion processes (LPBF) with researchers successfully achieving crack-free 99.5% dense products [120]. Research into post-process operations has confirmed that the microstructure can be manipulated by various heat treatment cycles to achieve a balance of moderate strength (1068 +/- 3 MPa) and high ductility (16.5 +/- 1.3%) as well as high strength (1400 MPa) and low ductility (5% elongation) [121]. To date, Ti-6242 has been successfully used in the context of DED to laser clad a worn turbine, combining near-net shape processing and post-process machining to the final dimensions as shown in Figure 48 [122]. This study utilized a single parameter set that was determined to produce the best results through trial and error. The chosen parameter set was a laser power of 1000W, traverse rate of 400 mm/min and a powder feed rate of 0.016 g/s. The toolpath was modified to shut off the laser at reversal points in order to prevent excess material build-up resulting from the increased heat input [122].

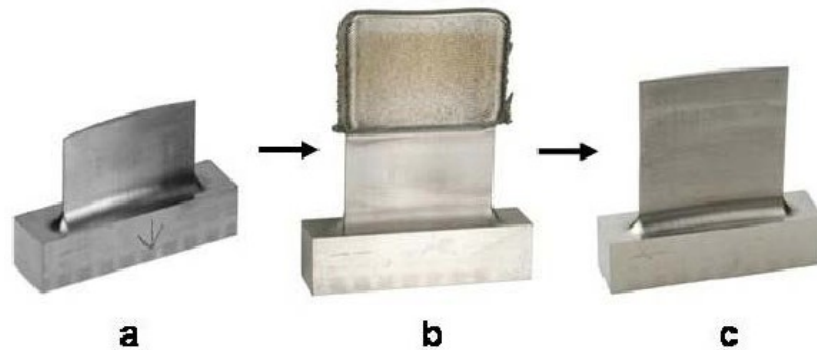


Figure 48: Ti-6242 turbine blade repaired using DED and post-process machining [122].

Another group of titanium alloys that offers unique properties over Ti-64 are β /near- β materials. β titanium alloys have the highest strength-to-weight ratio of all titanium alloys, along with excellent heat treatability [123]. Ti-15Mo-2.7Nb-3Al-0.2Si (Beta 21s) is one such alloy designed to improve corrosion resistance (particularly when exposed to aircraft hydraulic fluids) while maintaining oxidation resistance, tensile strength, and creep resistance at high temperatures as well. Beta 21s has not been examined in the context of DED; however, it has been successfully processed using LPBF. Researchers were able to

achieve moderate strength (UTS = 831 \pm 3 MPa) and high elongation (21 \pm 1.2% elongation) in as-built samples. With single (UTS = 1034MPa) and double (UTS = 862 MPa) aging heat treatments the strength was modified with concomitant adjustments in total ductility (6% and 10% elongation to failure respectively) [124]. Similar conclusions were independently observed with successful heat treatment of LPBF Beta 21s samples producing a UTS of 946 \pm 19 MPa and 25.3 \pm 3% elongation in the solution treated (ST) condition versus a UTS of 1348 \pm 4 MPa and ductility of 6.5 \pm 1% with subsequent aging (STA) [125]. In a similar vein, it is notable that Yanetta [126] was able to successfully process both Ti-20V and Ti-12Mo, both of which are β -stabilized titanium alloys. Through manipulation of the process parameters, both alloys produced microstructures considered sufficiently homogenous for industrial use, occurring at high power densities. The success experienced by Yanetta in processing these binary β titanium alloys provides confidence in the viability of DED processing for more complex β titanium alloys.

Collectively, studies in the open literature detailing the AM response of Ti-6242 and Beta 21S are largely limited to LPBF. The objective of this research was to expand upon these works but in the context of DED AM. In doing so, the effects of the principal process parameters were investigated in a statistically meaningful manner utilizing design of experiments concepts. Effective combinations of build parameters were then identified, and the resultant products subjected to comprehensive metallurgical assessment.

4.2 Materials and Methodology

4.2.1 Materials

Two metal powders supplied by GKN Hoeganaes were utilized in this research - AncorTi Beta 21S Grade C and AncorTi 6242. Each was produced through Electrode Induction-Melting Inert Gas Atomization (EIGA) technology into a fully prealloyed powder that was sieved to a size range appropriate for DED AM. Figure 49 shows representative images of

each powder source. Both maintained a spherical powder morphology with a sporadic presence of satellites.

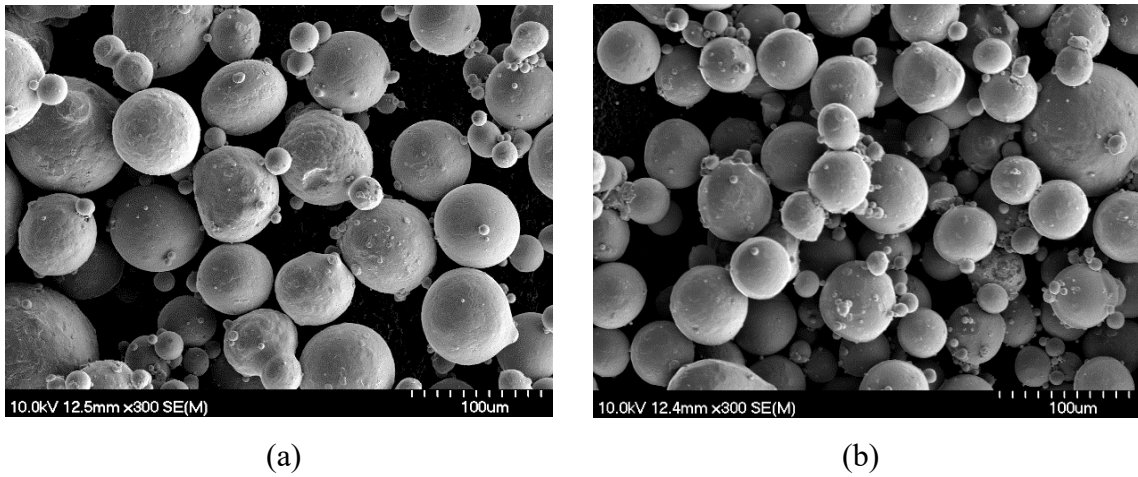


Figure 49: Powder morphology of (a) AncorTi Beta-21s and (b) AncorTi 6242.

Bulk chemical analyses were completed using a Varian Vista-PRO inductively coupled plasma – optical emission spectrometer (ICP-OES).. The measured chemical assays are shown in Table 6. All values were within the acceptable ranges specified for wrought counterparts.

Table 7 shows the results of impurity analyses for the as-received powders. OHN concentrations were measured through inert gas fusion (Eltra Elementrac ONH-p2 analyzer) while carbon values were quantified by combustion using a Leco (model 744) C/S analyzer. All values were within the acceptable ranges specified for these alloys.

Table 6: Assays for the raw powders utilized relative to wrought specifications (weight %).

Alloy		Al	Mo	Sn	Zr	Si	Nb
6242	Spec [127]	5.50 - 6.50	1.80 - 2.20	1.80 - 2.20	3.60 - 4.40	0.06 - 0.13	-
	Powder	6.20	2.10	2.00	3.90	-	-
Beta-21s	Spec [128]	2.50 - 3.50	14.00 – 16.00	-	-	0.15 - 0.25	2.40 - 3.20
	Powder	3.50	15.30	-	-	0.15	2.74

Table 7: Trace impurity analyses of raw powders (weight %).

Element	Ti-6242		Beta-21s	
	Spec. (max) [127]	Measured	Spec. (max) [128]	Measured
Carbon	0.08	0.02	0.05	0.01
Oxygen	0.15	0.11	0.17	0.11
Hydrogen	0.0125	0.003	0.015	0.001
Nitrogen	0.05	0.02	0.05	0.01

Flowability of the powders was determined using a hall flow meter according to MPIF Standard 03 while apparent density was measured using an Arnold meter according to MPIF Standard 48 [129, 130]. The results of these tests are presented in Table 8. Ti-6242 powder had a lower apparent density and a higher flow rate than the Beta-21s. However, both powders showed good flowability which is necessary for successful powder feeding through the deposition head.

Table 8: Apparent density and hall flow rate.

Alloy	Apparent Density (g/cc)	Flow Rate (s/50g)
Ti-6242	2.07	33.0
Beta-21S	2.58	24.8

Figure 50 shows the particle size distributions (PSD) measured through laser light diffraction (Malvern Mastersizer 3000). Table 9 lists the 10%, 50%, and 90% passing sizes (D10, D50, and D90 respectively) for each powder. All values ranged from 46 μm to 117 μm which is ideal for flowability and DED processing.

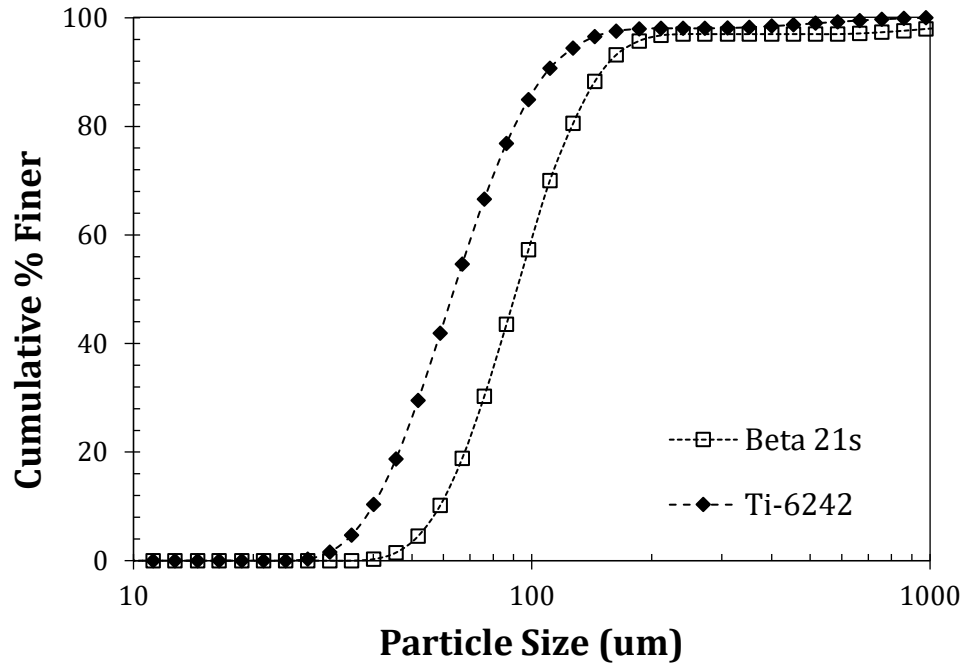


Figure 50: Cumulative % finer for the as-received Ti-6242 and Beta 21s powders

Table 9: Average particle diameters (D10, D50 and D90) for Ti-6242 and Beta-21s

Passing Size	Ti-6242	Beta 21s
D ₁₀	46 μm	58 μm
D ₅₀	59 μm	81 μm
D ₉₀	117 μm	110 μm

4.3 Methodology

4.3.1 DED Processing

Test specimen required in the research were produced with an Optomec LENS 500MTS-CA DED apparatus. The system was equipped with a 1kW Yb-fiber laser operated in continuous wave mode and focused to a nominal laser spot diameter of $\sim 700\mu\text{m}$. All builds were produced within the confines of a fully enclosed build chamber that was filled with ultra-high purity Ar (99.999%) and maintained a continuously measured oxygen concentration $\leq 10\text{ppm}$. The system afforded full control over laser power, traverse rate, hatch spacing, layer thickness, and powder feed rate. Each specimen geometry was

initially prepared as a stereolithography (.stl) file in Autodesk Fusion 360, which is a triangulated representation of the 3D model. Individual specimen files were then imported into MasterCAM 2020 where they were combined and arranged on the build plate appropriately. Using the post-processing features of MasterCAM 2020 along with the APlus plugin, each specimen was sliced into layers and the requisite processing parameters were applied.

Initially, a thin wall geometry was chosen to minimize the amount of time per sample and allow for an expedited initial assessment of process parameters. These were comprised of single bead width layers (0.8 mm), stacked to a height of 10 mm. The build strategy was kept simple, with active deposition occurring in only one direction followed by a return to origin with the laser disabled before beginning the next layer. Additional geometries included 10x10x10mm cubes for density measurements and 10x10x85mm rectangles fabricated with the long axis parallel to the build direction for the purposes of studying heat treatment effects on tensile properties. A consistent build strategy was implemented for these samples, consisting of a simple zig-zag pattern, with the orientation of the pattern rotating 90 degrees between each layer to ensure full coverage while concurrently offsetting the start/stop points.

4.3.2 Statistical Investigation of DED Processing Parameters

To efficiently examine the effects and interactions between the primary process parameters, a statistical approach was chosen. This included builds fabricated in accordance with two separate designs of experiments (DOEs) for each alloy. All DOE specimens were 10x10x10mm cubes built on commercially pure titanium plate 12.5mm thick. The initial DOE (DOE1) varied the two most effective parameters (laser power and traverse rate) and covered a wide range to confirm the feasibility of DED processing for these alloys and identify the approximate working range for the subsequent DOE. Table 10 lists the range of process parameters selected for each alloy. All ranges were chosen based on prior work with similar titanium-based alloys coupled with basic trials using single bead depositions. A central composite design that facilitated statistical analysis was

then generated using Minitab software. When executing DOE1 all other controllable variables were kept constant.

Table 10: Process parameter ranges utilized in the development of DOE1.

Alloy	Laser Power (W)		Traverse rate (mm/s)	
	Minimum	Maximum	Minimum	Maximum
Beta 21s	305	445	5.5	11.4
Ti 6242	380	520	7.6	13.6

With input from the results of DOE1, a second central composite design (DOE2) was generated. This was more comprehensive as it not only included the influence of laser power and traverse rate but was also broadened to allow for consideration of hatch spacing, layer height, and powder feed rate. The choice of process parameter ranges for laser power and traverse rate was informed by the results of DOE1, whereas those for the additional parameters were based on prior experiments with Ti-64 powder. The DOE2 parameter ranges for both alloys are shown in Table 11. To minimize build time while maintaining statistical significance, a half composite design was developed in Minitab comprising 32 discrete samples that embodied the full ranges of parameters considered.

Table 11: Process parameter ranges utilized in the development of DOE2.

Alloy	Laser Power (W)		Traverse Rate (mm/s)		Hatch (mm)		Height (mm.)		Powder Feed Rate (g/s)	
	<i>Min</i>	<i>Max</i>	<i>Min</i>	<i>Max</i>	<i>Min</i>	<i>Max</i>	<i>Min</i>	<i>Max</i>	<i>Min</i>	<i>Max</i>
Beta-21s	300	500	3.18	12.70	0.64	2.67	0.10	0.51	0.13	0.64
Ti-6242	350	550	6.35	14.82	0.64	2.67	0.10	0.51	0.03	0.17

4.3.3 Material Characterization

All samples were removed from the build plate with a vertical bandsaw and any rough edges removed with 80 grit SiC paper. Density measurements were completed using an

Archimedes approach coupled with oil infiltration (MPIF Standard 42 [131]). Following density measurements, samples were cleaned using a Soxhlet extractor with immersion in petroleum ether for 30 minutes to remove any infiltrated oil. Samples were then sectioned perpendicular to the build direction using a diamond abrasive cutoff wheel and mounted in conductive bakelite. Mounts were then ground and polished (500 grit diamond abrasive disc, 9-micron MD-Largo suspension and 3-micron MD-Dac with an OP-S+H₂O₂ suspension) prior to cleaning with acetone in an ultrasonic bath. Microstructures were examined as polished and after etching using a two-step process of swabbing with Kroll's reagent followed by immersion in Weck's reagent. Samples were imaged using a Keyence VK-X3000 laser confocal microscope to obtain full surface stitched images and a Hitachi S-4700 Cold Field Emission Scanning Electron Microscope (SEM) for higher magnifications. An accelerating voltage of 10 kV and emission current of 20000 nA were used for the latter.

Specimens fabricated for tensile testing purposes were heat treated based on a series of industrially relevant practices for each alloy. Two bars were tested for each alloy/heat treatment considered. The type of cycle and the time/temperature parameters employed are shown in Table 12. All heat treatments were performed in air using a Thermo Scientific Lindberg/Blue M Model BF51866-1 box furnace that was calibrated for the given sample size and associated heating and cooling rates. Samples were air cooled between steps. Test bars were then machined into cylindrical tensile samples with threaded ends as per ASTM standard E8/E8M-21 [132]. An Instron model 5594-200HVL hydraulic load frame equipped with a 50kN load cell was used for tensile testing purposes. A calibrated Epsilon model 3542 extensometer with a gauge length of 25 mm was utilized for strain measurement and remained attached to the specimen through the point of fracture.

Table 12: Heat treatments applied to DED specimen.

Alloy	Heat Treatment	Temperature (°C)	Time (h)	Temperature (°C)	Time (h)
Ti-6242	Stress Relief (SR-1)	595	4	-	-
	Stress Relief (SR-2)	705	0.25	-	-
	Solutionize and Age (STA)	955	1	595	8
	Anneal	900	0.75	-	-
Beta-21s	Anneal	843	0.5	-	-
	Solution Treat Age (STA-1)	843	0.5	510	8
	Solution Treat Age (STA-2)	843	0.5	679	8

4.4 Results and Discussion

4.4.1 Beta 21s

4.4.1.1 DOE1

The initial 13 cube DOE was performed using the parameter ranges listed in Table 10. All parameter sets were able to successfully deposit a sample approximating the desired geometry. The densities of specimens ranged from 4.58 g/cm³ to 4.64 g/cm³. To compare results more easily across various parameter sets, a commonly used input parameter is volumetric energy density (VED):

$$VED = \frac{L_p}{T_r H_s Z_s}$$

Where L_p is the laser power, T_r is the traverse rate, H_s is the hatch spacing, and Z_s is the layer height. For this series of samples, the energy densities ranged from 173 J/mm³ to 385 J/mm³. Figure 51 shows an example build plate for the DOE1 Beta 21s samples, highlighting the consistent outward appearance of the various process parameters.

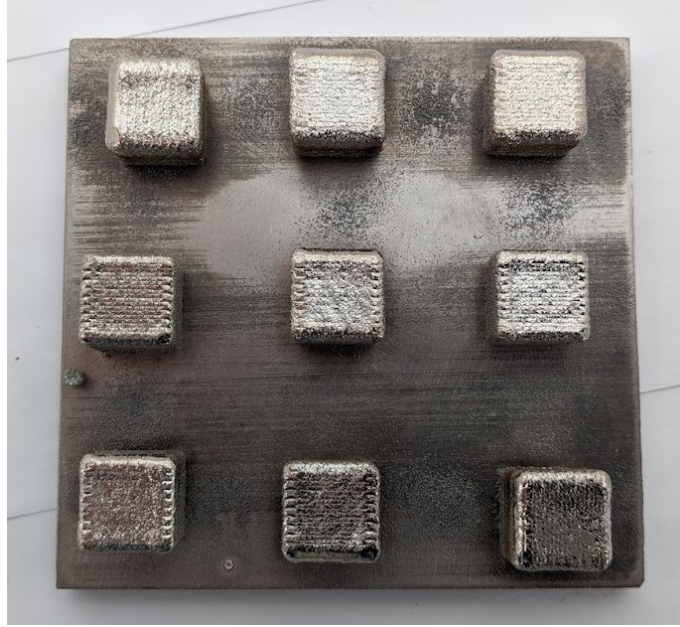


Figure 51: As-built DOE1 Beta 21s samples on Ti-64 substrate.

Data illustrating the correlation between the applied VED and final build densities are shown in Figure 52. In general, there was a modest upward trend with density improving slightly as VED increased to a level of $\sim 300 \text{ J/mm}^3$. In this sense, a minimum density of 4.90 g/cm^3 was noted at 185 J/mm^3 , while a maximum value of 4.93 g/cm^3 was measured with a VED input of 250 J/mm^3 . At higher VED inputs, the build density values remained static or declined slightly. These parameter sets consisted of very slow traverse rates (5.5 and 6.35 mm/s) and relatively high laser power (375 and 425W) which brought about circumstances that could have manifested keyhole porosity. The highest densities (4.93 g/cm^3) represented 99.8% of the reported theoretical density of wrought Beta-21s (4.94 g/cm^3) and even the lowest density products were $>99.2\%$ of full theoretical.

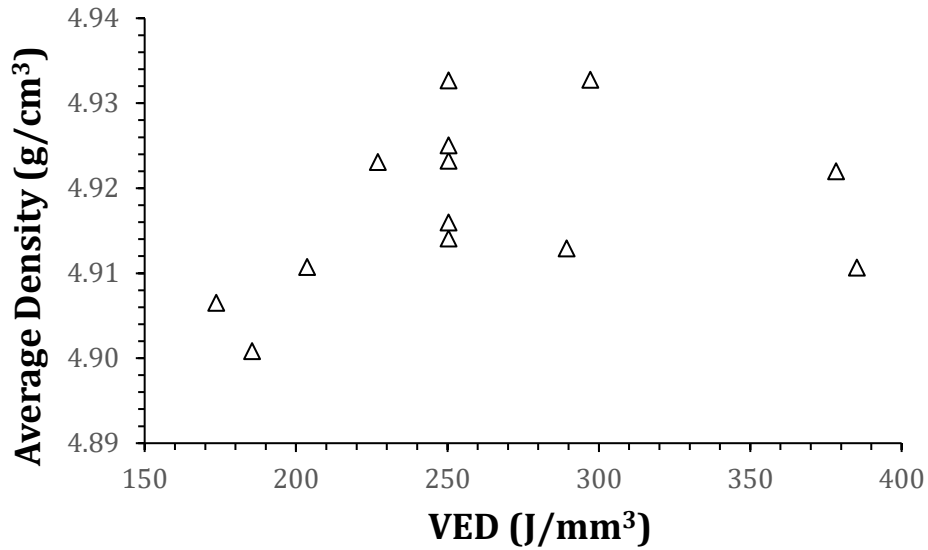


Figure 52: Density vs. VED for Beta 21s specimen (DOE1).

Figure 53 shows the interaction plots between laser power and traverse rate, the parameters of interest in this set of experiments. The 3 lines represent the 3 different traverse rates, and the plot compares the averaged density (y-axis) to the laser power (x-axis). All three traverse rates feature an upward trend with increasing laser power which indicated that as laser power increases density does so as well regardless of traverse rate. The slopes for the 8.5 and 10.6 mm/s trend lines were similar, while the 6.4 mm/s line was less acute. The reduced slope for the latter suggests that the density was less dependent on laser power for this low speed. It was postulated that these differences reflected the balance needed between speed and energy input in the formation of an effective melt pool. In this sense, the density was more acutely influenced by laser power for the faster traverse rates since the melt pool was moving rapidly under these conditions This reduced the duration of time for melting of the incoming powder and thereby manifested a need for higher energy input that results from increased laser power.

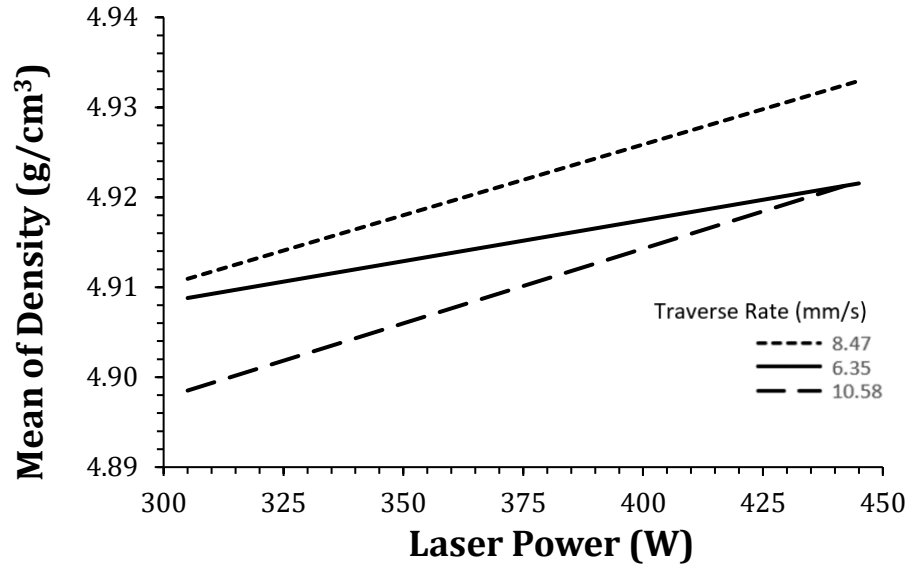


Figure 53: Interaction plot showing the effects of laser power and traverse rate on averaged densities for Beta 21s samples built in DOE1.

Figure 54 highlights an issue encountered during DOE1 with regards to the initial layer adhesion. Here, several samples showed failure to fully adhere in the first few layers although the problem resolved itself throughout the remainder of the build. Through additional experimentation it was determined that this defect was the result of an excessive initial z-offset. To determine a more effective setting, replicate samples were prepared using identical process parameters but three different z-offsets of 6.35, 7.94, and 9.53mm. These samples were then examined under the laser confocal microscope. It was noted that the same lack of adhesion prevailed in the sample fabricated with the same offset utilized in DOE1 (9.53mm). The defect was eliminated in both of the other offsets considered although the smallest distance manifested overbuilding. As such, an intermediate value of 7.94mm was chosen for all remaining builds.

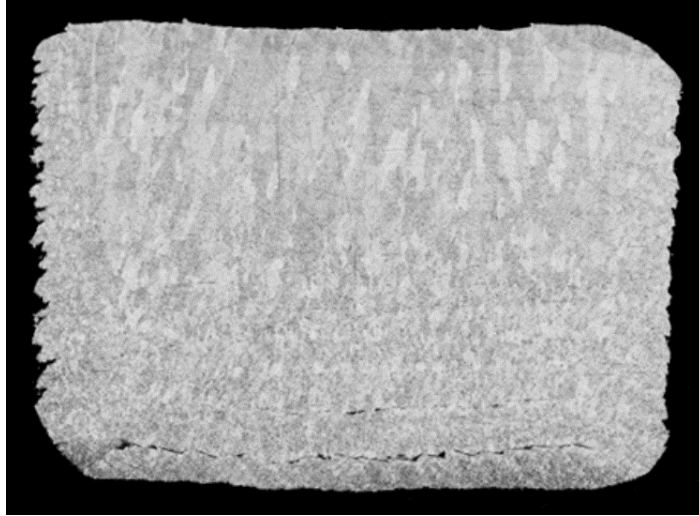


Figure 54: Initial layer adhesion issue observed in DOE1 builds of Beta 21S fabricated with a z-offset of 9.53mm. Sample produced with a laser power of 425 watts and a traverse speed of 10.6 mm/s.

4.4.1.2 DOE2

Given the relative success of all parameter sets in DOE1, the working ranges for laser power and traverse rate were increased to 350-500W and 6.3-15.9 mm/s respectively in the second experimental design (DOE2) that featured additional process variables. Figure 55 shows the density vs. VED results for the complete set of 32 samples. The initial upward trend observed in DOE1 is present here as well although with the increased sample size and parameter ranges, the trend was more definitive. The lowest VED values resulted in relatively low-density samples. However, gradually improved densities were observed to VEDs of $\sim 150 \text{ J/mm}^3$. Density values were then scattered from 4.89 to 4.93 for higher energy densities. The highest density observed (4.93 g/cm^3) occurred at an energy density of 126 J/mm^3 while the minimum density of 4.79 g/cm^3 occurred at an energy density of 37 J/mm^3 . There were several VED values that included multiple samples, yet the results were scattered significantly as each was produced under a unique set of process parameters. This highlighted the importance of accounting for the process parameter variations, given their different individual impacts. Such effects are not reflected in the simplistic plots premised on a calculated VED and thereby mandated the integration of statistical analyses.

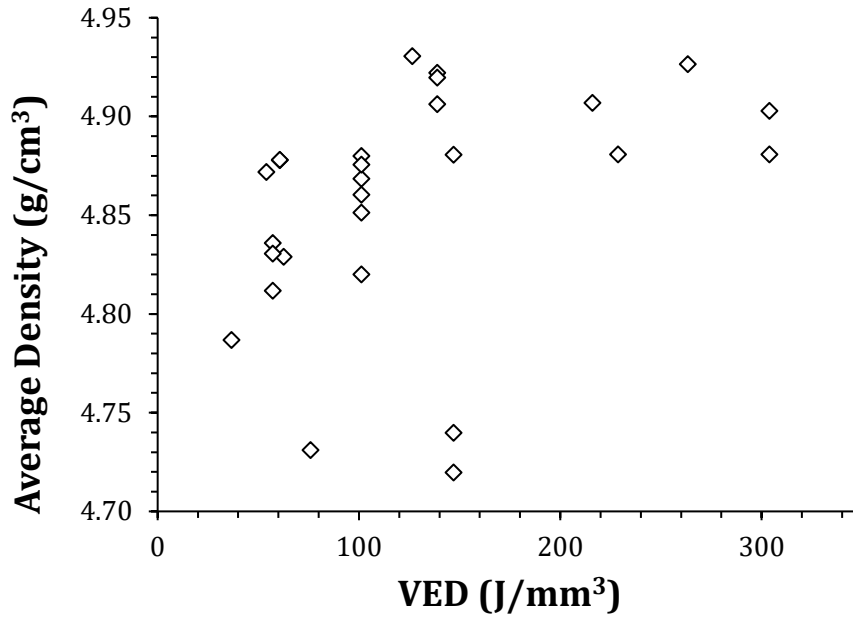


Figure 55: Density vs. VED for Beta 21s specimen (DOE2).

Figure 56 shows the results of statistical analysis applied to individual effects of specific process parameters on build density. Laser power showed an upward trend. The modest difference between the low and high extremes in this variable implied that the lowest power had likely exceeded the minimum level necessary for sufficient melting of the incoming powder so as to form a stable melt pool.

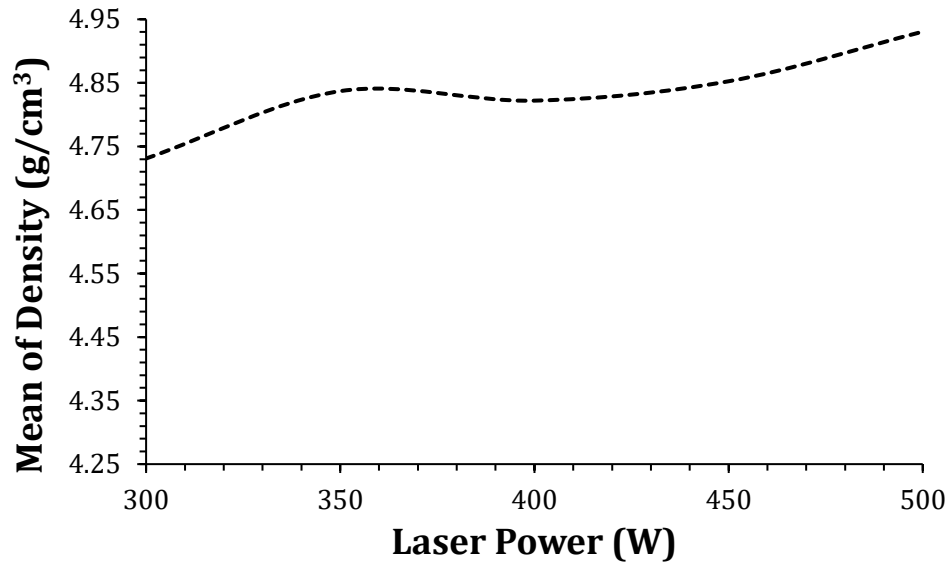


Figure 56: Main effect plot of Laser power for Beta-21s powder.

The traverse rate (9.5-16 mm/s) and layer height (0.08-0.2 mm) showed similar trends to each other with a peak density observed at low parameter values followed by a significant decrease with increased set point values. As shown in Figure 57, the peak density coincided with a speed of ~11 mm/s. There was no meaningful density-based advantage to going below this value and the risk of overbuilding increased. Above this value, the melt pool would have moved too quickly to maintain a consistent build quality as reflected in the steep decline in density.

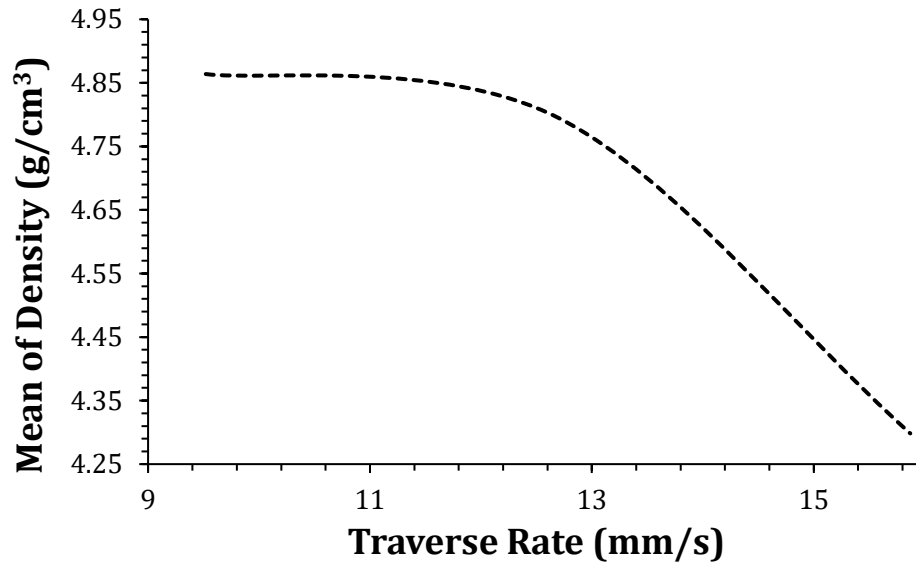


Figure 57: Main effect plot of traverse rate for Beta-21s powder

Figure 58 shows the effect of layer height on mean density. A layer height set point of ~ 95 μm was coincident with peak density. Here, adequate z-direction overlap would have occurred to melt the freshly blown powder and concurrently allow for remelting and densification of gaps in previously solidified layers. This capacity would have deteriorated at increased layer heights as these would have limited the extent of prior layer re-melting.

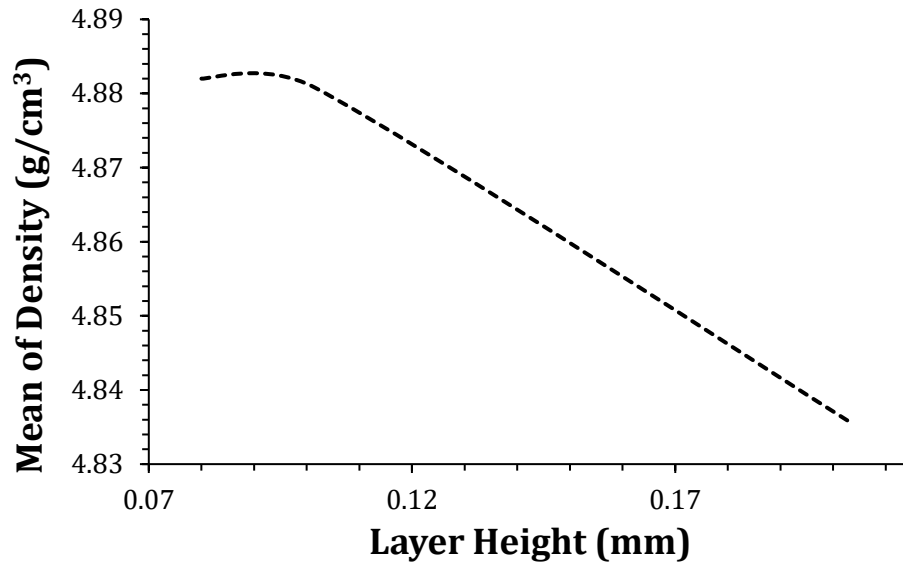


Figure 58: Main effect plot of layer height for Beta-21s powder

Hatch spacing was varied between 0.6 and 1.7 mm and manifested a continual downward trend as it was increased towards larger values as shown in Figure 59. As the hatch spacing increases the gap between adjacent weld tracks is increased. Under certain conditions, this can promote inadequate overlapping and remelting of prior tracks leaving parallel arrays of voids in the material and a reduced final density. These factors would have driven the downward trend observed. When pairing a large hatch spacing with a small layer height it is possible for subsequent layers to remelt and fill these gaps, however, it is preferable to determine an appropriate hatch spacing to minimize the number of layers and thereby minimize build times.

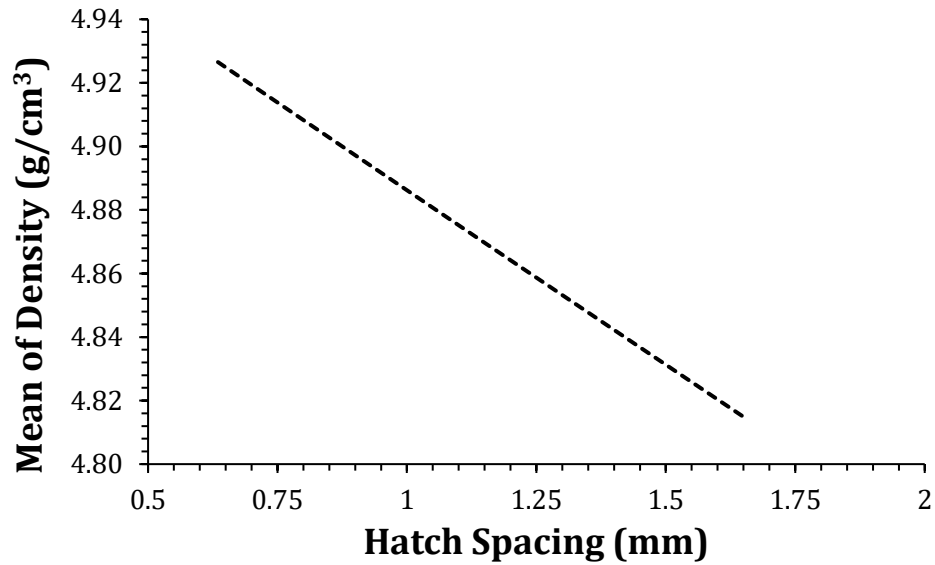


Figure 59: Main effect plot of hatch spacing for Beta-21s powder

An example of porosity induced by improper hatch spacing is shown in Figure 60. In this sample, there was a clear grid of large pores throughout the bottom layers, which indicates that the hatch spacing was excessive such that a gap was retained between deposition tracks. This large hatch spacing combined with a layer height that precluded adequate remelting to fill the gaps resulted in a series of vacant channels throughout the sample and very poor density.



Figure 60: Porosity induced in a build of Beta-21S due to excessive hatch spacing. Sample fabricated with a hatch spacing of 2.67 mm.

The powder feed rate (0.09-0.69 g/s) showed the inverse trend of traverse rate and layer height as observed in Figure 61. In this sense, low powder feed rates manifested the production of samples with low densities. However, build density then improved steadily to a peak value where it remained relatively static throughout the highest feed rates considered. The low powder feed rates would have provided an insufficient amount of powder to form a melt pool of a size needed for full density processing. Conversely, the peak powder feed would have coincided with the maximum powder capture rate and the presence of a sizable, stable melt pool. The delivery of excessive powder beyond this point would have exasperated overspray and an increased level of wasted powder. Although the density changes were seemingly minor at feed rates above ~ 0.55 g/s, the possibility of a modest downward trend was apparent. This was viewed as a plausible scenario as excessive powder could divert a meaningful portion of the incident radiation away from the melt pool so as to reduce its size and build effectiveness.

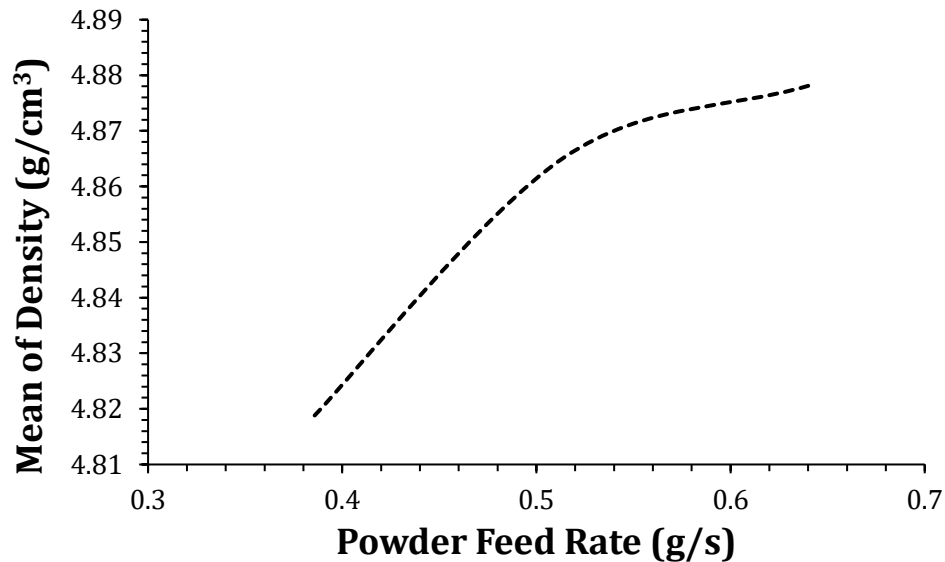


Figure 61: Main effect plot of powder feed rate for Beta-21s.

Beyond process-induced porosity, select builds also showed evidence of gas-induced porosity (Figure 62). This was believed to result from entrapment of the flowing argon gas used to transport powder to the laser and/or the release of surface-adsorbed gases present

on the powder. Features such as this are common to DED products given that as the solidification front quickly progresses, the gas can become trapped within the melt pool. Due to the rapid solidification present in the laser DED process, the associated bubbles cannot escape before solidification, leaving a spherical pore in the solidified product.

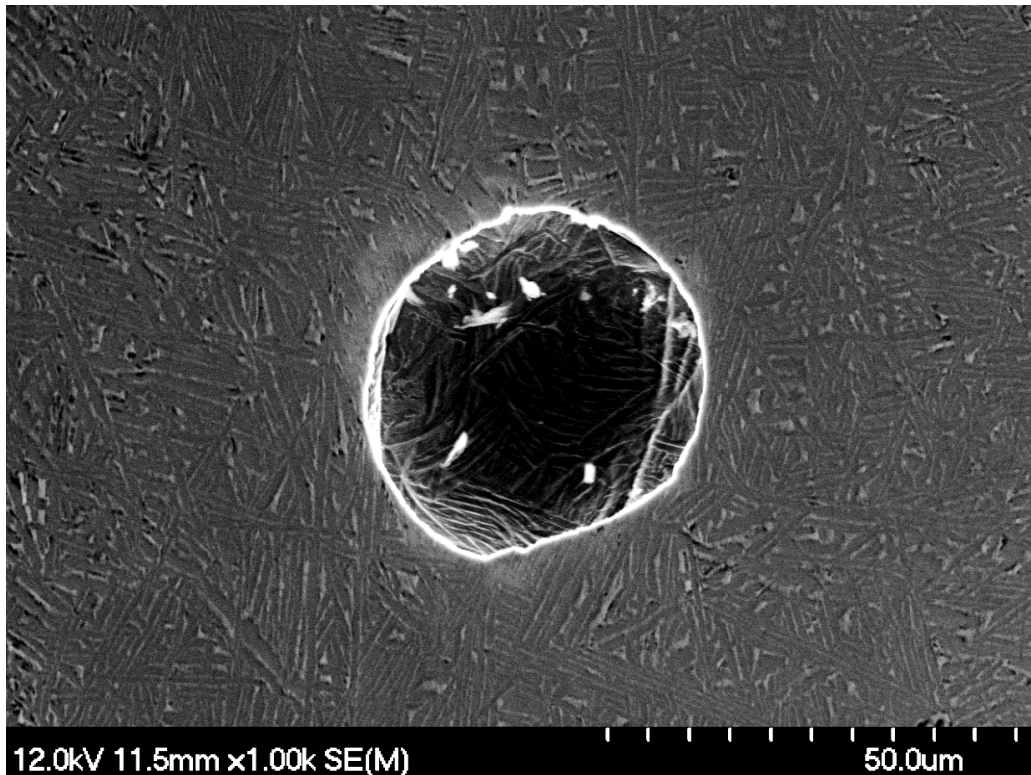


Figure 62: Example of gas-induced porosity retained in a Beta 21S build.

Based on DOE2, several parameter sets were identified as being capable of producing samples that were effectively fully dense. Many parameter sets produced densities >99% of theoretical density, with 4 of them producing densities >99.8%. Given the success of all 4 sets, it was necessary to take into account the ease of building in addition to the numerical results. For example, one difficulty was balling of partially melted powder on the nozzles which led to clogging, poor surface finish, and inaccurate sample geometry. During the build process the fabrication cycle would need to be stopped to clear these clogs which significantly increased build time and the amount of direct supervision required which

would be impractical for a larger scale build. Balling was most frequent on parameter sets that featured low traverse rates and high laser powers, which also tended to produce higher density samples. Of the high-density process parameters, the one that experienced minimal balling comprised a laser power of 450W, traverse speed of 6.35 mm/s, 1.14 mm hatch spacing, 0.4 mm layer height, and a powder flow rate of 0.55 g/s. Hence, these parameters were chosen for subsequent builds needed for heat treatment studies as they represented a balance between achievable density and the practical capacity to produce test specimen.

4.4.1.3 Heat Treatments

Heat treatment specimens were rectangular, and all were fabricated so that the longitudinal axis was parallel to the build direction. This orientation was selected as it represented the approach under which the most conservative values for tensile properties would be expected due to the increased likelihood of layer delamination. These were heat treated and machined into tensile bars. A summary of the tensile results for Beta 21S is shown in Table 13. This includes experimental data as well as textbook values for the wrought counterpart when known. As-built samples maintained a yield strength and UTS that were similar to wrought Beta 21S in an annealed state. However, they also exhibited a relatively low stiffness and a net ductility of only 2% to fracture. The latter was significantly inferior to wrought (12%) and regarded as a low value for a typical commercial alloy. Application of an annealing treatment manifested beneficial changes. In this sense, ductility more than tripled to 7% while a modest gain in stiffness also transpired. UTS remained essentially static while a slight decline in yield strength transpired as well. The corresponding microstructure of these samples are shown in Figure 63(a) and (b). It is evident looking at these microstructures that this heat treatment converted the as-built microstructure consisting of large hexagonal β grains into a combination of prior- β grains, grain boundary alpha (α_{GB}) and acicular α within these grains. Although the introduction of α phase generally decreases ductility in wrought samples, the improvement in microstructural homogeneity between as-built and annealed likely contributed to the increase from 2 to 7%. In general, both as-built and annealed samples had ductilities lower than wrought

which is consistent with previous findings [133]. In an overall sense, the mechanical properties of annealed DED specimen of Beta 21S were reasonably comparable to those of the wrought counterpart but clear deficiencies were retained.

The other heat treatments considered were STA processes (Table 13). In each case, the samples were processed through the same annealing cycle discussed above, but then reheated through a secondary cycle of aging that involved a lower temperature, but longer hold time. For cycle STA-1 wherein samples were aged at 510°C for 8 hours, significant gains in the vicinity of 50% were observed in yield strength and UTS relative to data from the annealed specimen. The averaged values for these properties were also comparable to those typical of a wrought counterpart. Stiffness was improved as well yet ductility declined back to a level similar to the as-built material. After the application of STA-2 (aging 8h at 679°C), lower values of yield strength and UTS were observed yet the net strain to fracture improved significantly rising to 10%; the highest value measured for any of the Beta 21S samples. Notably, this ductility as well as the averaged values for yield strength and UTS all exceed the typical values achieved in wrought Beta 21S.

Trends in the tensile properties of STA specimen confirmed that the DED material was responsive to both aging cycles. During this stage of heat treatment it is known that the α phase will precipitate at preferential nucleation sites such as grain boundaries, dislocations and point defects resulting in α_{GB} and acicular or plate-like α within the grains. Due to the rapid solidification present in AM processes, more vacancies tend to become trapped within the grains, which results in an increase in intragranular α . Further aging following nucleation will result in growth of the intragranular α into α plates, which can be observed in Figure 63(c) and (d). The prolonged higher temperature heat treatment (STA2) resulted in a larger amount of α_{GB} as well as more acicular intragranular α . The increased amount of intragranular α results in impeded growth leading to less coarse α with a more acicular morphology than the larger plate-like intragranular α produced by the lower temperature heat treatment in STA1.

Table 13: Tensile properties of Beta 21S bars fabricated in accordance with high density build parameters (DOE2) and select post-build heat treatments. Typical data for the wrought counterpart shown for comparison purposes [134-136].

	YS		E		UTS		% Ductility	
	Meas.	<i>Wrought</i>	Meas.	<i>Wrought</i>	Meas.	<i>Wrought</i>	Meas.	<i>Wrought</i>
As-Built	873 (+/- 93)	-	71 (+/- 6)	-	902 (+/- 102)	-	2 (+/- 1)	-
Annealed	857 (+/- 77)	883	75 (+/- 6)	100	911 (+/- 84)	931	7 (+/- 0.2)	12
STA-1	1315 (+/- 35)	1383	111 (+/- 18)	-	1447 (+/- 53)	1473	2 (+/- 0.4)	-
STA-2	1040 (+/- 50)	965	86 (+/- 3)	100	1103 (+/- 47)	1034	10 (+/- 3)	6

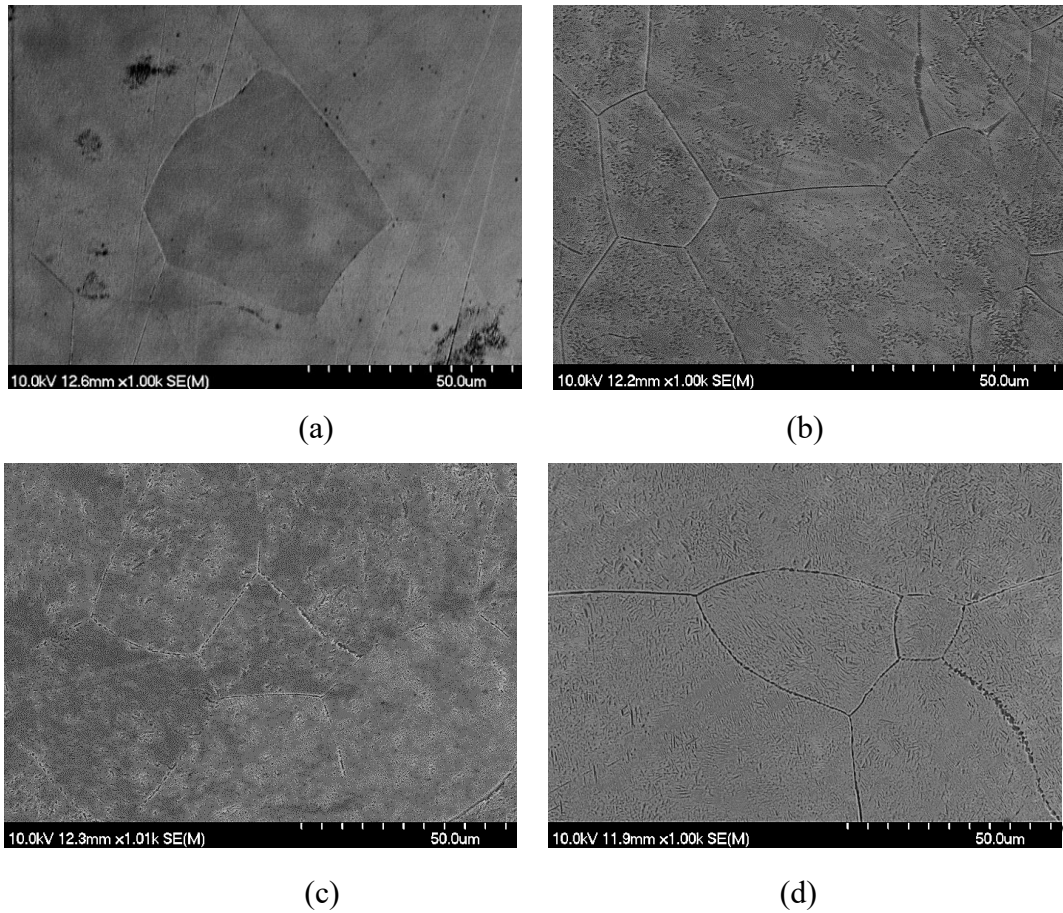


Figure 63: Microstructures of Beta 21S specimen (a) as-built, and after (b) STA1, (c) STA2, and (d) annealing heat treatments.

4.4.2 *Ti-6242*

4.4.2.1 *DOE1*

The experimental design techniques employed for Beta 21s were also used for Ti-6242 with the parameter ranges modified slightly (See Table 10) based off initial experiments. The results of the preliminary DOE1 in terms of density vs. volumetric energy density are shown in Figure 64. There was no clear trend in the data due to the range of resultant densities being too small. The highest density sample was 4.535 g/cm^3 at an energy density

of 240 J/mm³, and the lowest was 4.526 g/cm³ at 335 J/mm³. This represented a range of only 0.009 g/cm³, which was too narrow of a range to confidently make conclusions. Although these results did not aid in identifying trends, the findings were promising as they indicated that nearly full densities could be achieved (~99.9% of wrought Ti-6242 at 4.54 g/cm³) over a relatively wide range of energy densities (178 to 334 J/mm³).

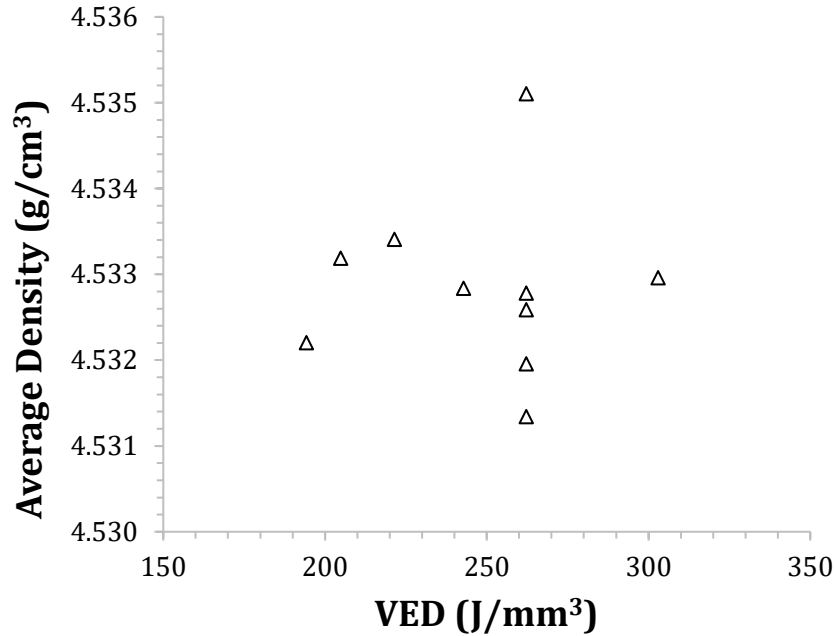


Figure 64: Density vs. VED for Ti-6242 specimen (DOE1).

Figure 65 shows the interaction plots for mean of density vs. laser power and traverse rate. Each line represents a different traverse rate, encompassing the three values used in this set of experiments. For the 8.47 and 10.58 mm/s speeds, there was a similar upward trend, with improved densities noted at progressively higher laser powers. For the 8.47 mm/s curve, the low laser power density values were much lower than counterparts fabricated at 10.58 mm/s. As the laser power increased, the slope of the 8.47 mm/s curve became much steeper, ultimately resulting in both traverse rates producing the same density product (~4.534; 99.9%) at a laser power of 520W. When using the highest traverse speed considered (12.7 mm/s) the densities of all samples were statistically equivalent regardless

of the laser power employed. Furthermore, the densities from all three traverse speeds converged to a final value of ~99.8-99.8% of full theoretical at a laser power of 520W. These transitions indicated that products impinging on full theoretical density could be produced over a considerable range of laser powers provide that an appropriate traverse speed was utilized (12.7 mm/s).

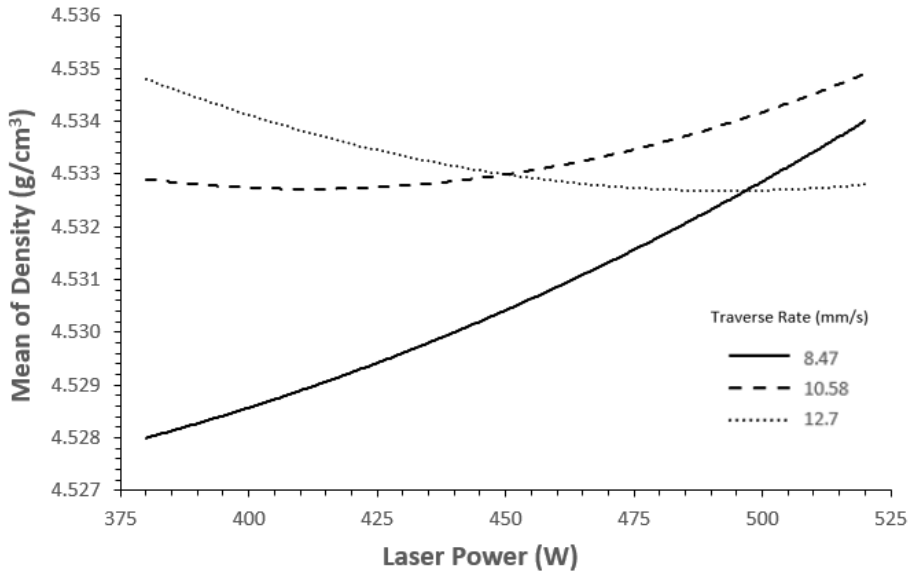


Figure 65: Interaction plot showing the effect of laser power and traverse rate on mean density for Ti-6242 (DOE1).

4.4.2.2 DOE2

Figure 66 shows the plot of density vs. energy density for Ti-6242 DOE2. The lowest densities were ~4.37 g/cm³ and occurred at low VEDs ranging from ~50-100 J/mm³. Although considerable scatter in the data prevailed, generally speaking, densities were improved with higher VED inputs. Further analysis of these data are shown in the main effect plots of Figure 67-69.

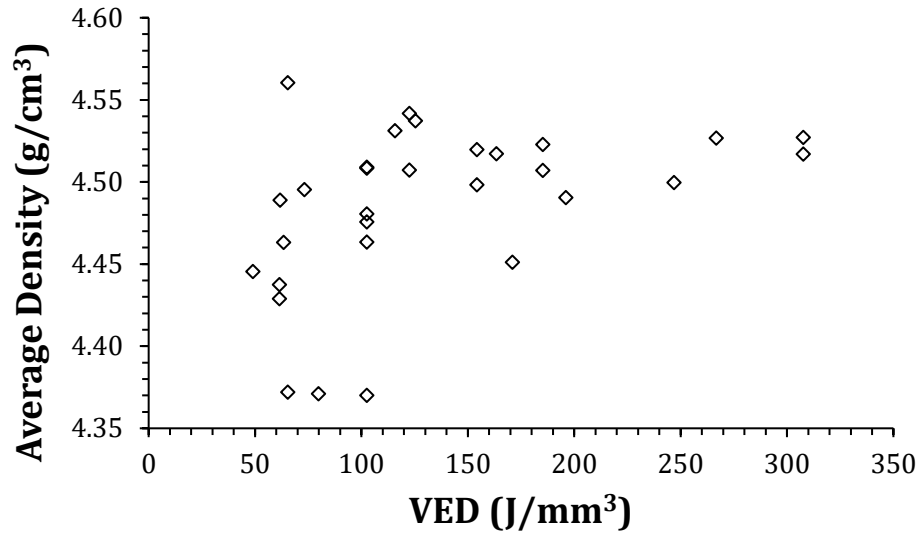


Figure 66: Density vs. VED for Ti-6242 specimen (DOE2).

In Figure 67, the main effect plot for laser power is presented. Here, a linear, upward trend of improved density with increased laser power was observed. This was largely as expected, as increased power would invoke increased heat input thereby improving powder capture efficiency and melt pool stability.

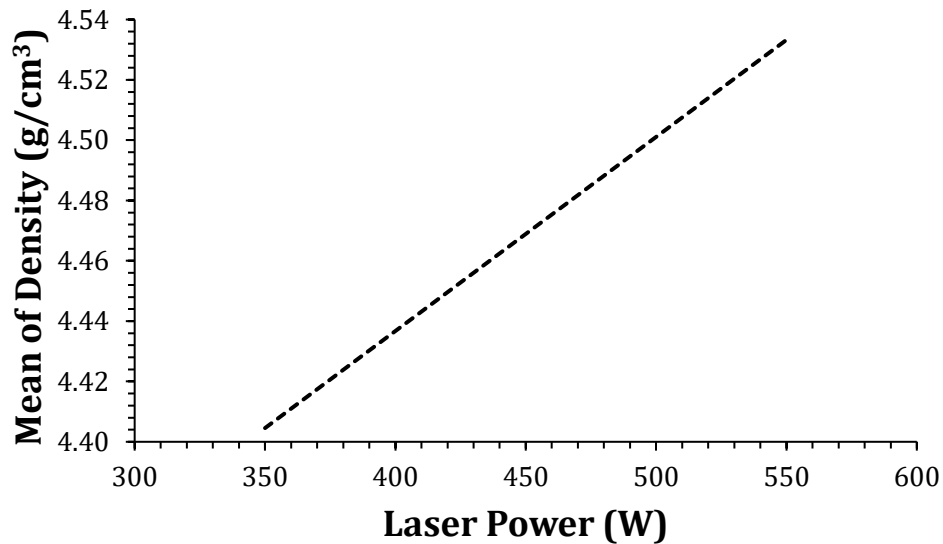


Figure 67: Main effect plot of laser power for Ti-6242 powder.

Unlike laser power, the traverse rate, hatch spacing, layer height and powder feed rate plots all exhibited downward trends in density as the parameter set point was increased. For traverse rate (Figure 68), increases in this parameter would have invoked reduced levels of heat input. This would have diminished the ability to maintain a stable melt pool and deteriorated final density values.

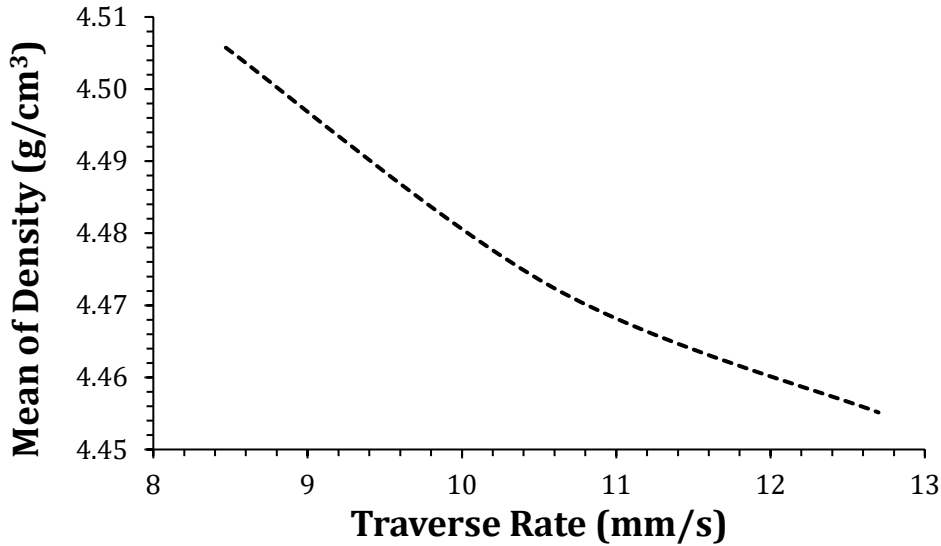


Figure 68: Main effect plot of traverse rate for Ti-6242 powder.

For hatch spacing (Figure 69), a value for this parameter should be utilized such that the deposited tracks maintain a level of overlap to ensure appropriate fusion with those applied through prior passes by the laser. Assuming that the weld track itself maintains a relatively consistent width, increases to hatch spacing diminish the extent of overlap. Excessively large values could eliminate it altogether and prompt the formation of a gap (and concomitantly, porosity) between adjacent tracks to the detriment of final product density.

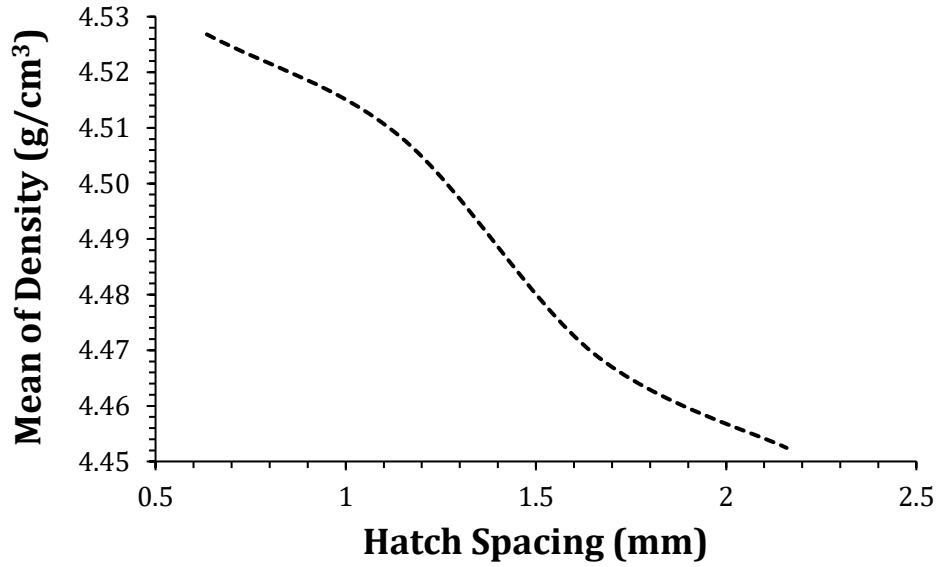


Figure 69: Main effect plot of hatch spacing for Ti-6242 powder.

The layer height effects are shown in Figure 70. As the set point value for this parameter was increased, density declined through a statistically meaningful extent of 4.52 g/cm³ (99.6%) to 4.43 g/cm³ (97.6%). Thin layer heights have the advantage of invoking appreciable remelting of prior layers which can potentially fill small gaps and/or porosity within them. As the layer height was increased, the capacity to eliminate these defects would have declined, manifesting the steady reduction in density that was observed.

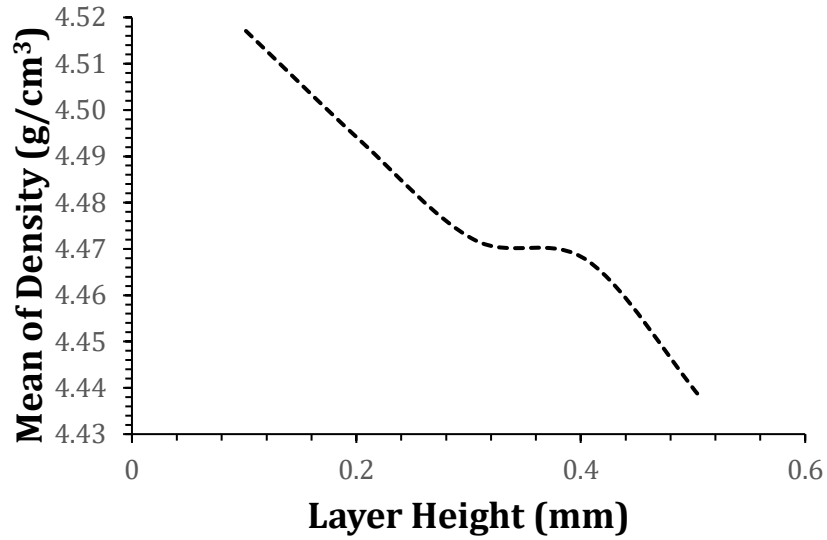


Figure 70: Main effect plot of layer height for Ti-6242 powder.

The decrease in density with increasing powder feed rate shown in Figure 71 doesn't have a clear explanation. However, comparing to the Beta-21s results (Figure 61), it is possible that the chosen powder feed rate range fell on the right side of the curve, where the lowest chosen value represents the necessary rate for maximum density, and any increase thereby had a negative effect.

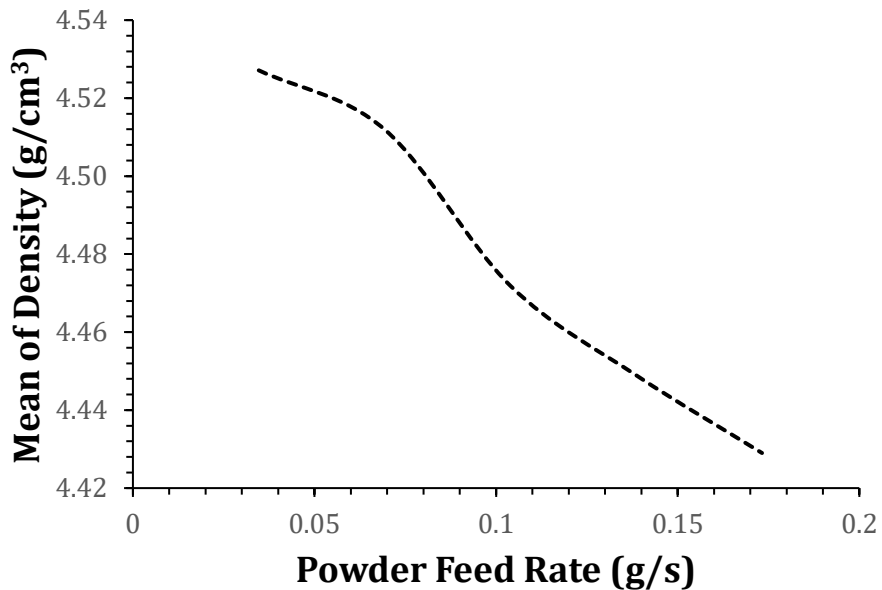


Figure 71: Main effect plot of powder feed rate for the Ti-6242 powder.

As with the Beta-21s samples, the Ti-6242 samples also exhibited two morphologies of porosity. Figure 72(a) shows a sample with gas-induced porosity, distinguished by a spherical morphology, and caused by gas entrapment in the melt pool. Conversely, Figure 72(b) shows a sample with process-induced porosity which is the result of an excessive hatch spacing that facilitated the development of a gap between adjacent tracks.

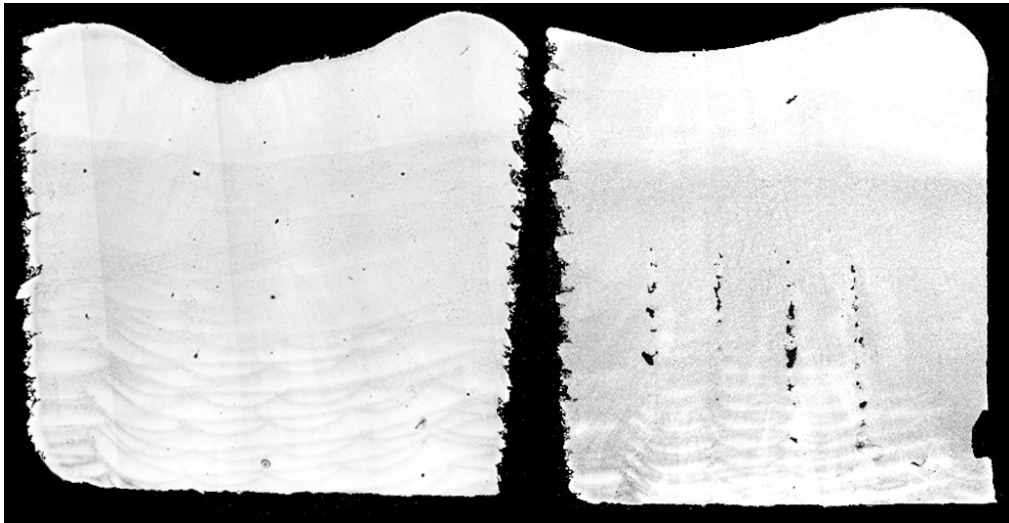


Figure 72: Examples of (a) gas-induced porosity and (b) process-induced porosity in Ti-6242 DOE2.

Based on the results of DOE2, there were 18 parameter sets that produced high density (>99%) samples of Ti-6242. Given that several options for high-density parameter sets were known, qualitative observations needed to be factored in to determine which parameter set should be used to fabricate additional samples for heat treatment studies. Several of the noted parameter sets featured relatively high laser powers combined with relatively low traverse rates. These resulted in significant overbuilding which would render the production of dimensionally accurate parts difficult. In addition, the frequency of balling on and subsequent clogging of the powder deposition nozzles was also a concern. Based on a balance of high density, dimensional accuracy and minimal balling, the parameter set chosen for heat treatment and mechanical testing was: 450W laser power,

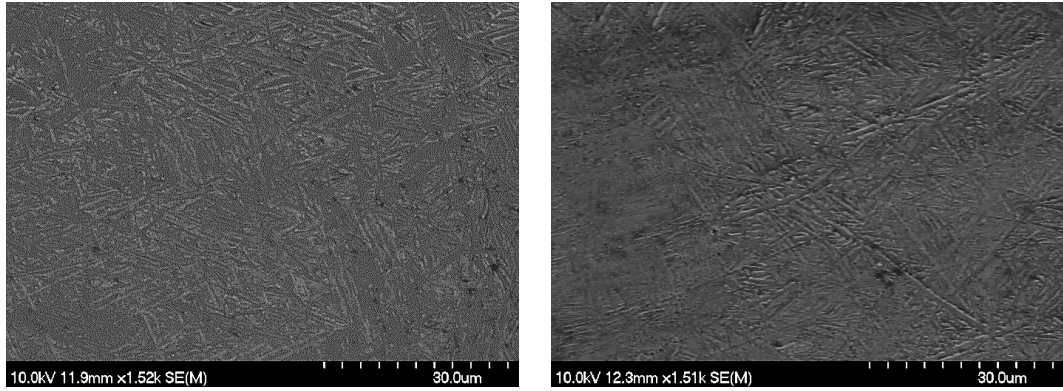
6.35 mm/s traverse rate, 0.4 mm layer height, 1.14 mm hatch spacing and a powder feed rate of 0.14 g/s.

4.4.2.3 Heat Treatments

Table 14 shows averaged tensile results for Ti-6242 samples in the as-built condition and after the application of different heat treatments appropriate for this alloy. Figure 73(a) and (b) show the microstructures of as-built and annealed samples respectively. The as-built sample had a UTS of 973 MPa, annealing at 900C for 30 minutes decreased the UTS slightly to 970 MPa which is slightly less than the wrought value of 1060 MPa. Comparing the microstructures, they both consisted of primarily martensitic α' , which is representative of rapidly cooled near- α titaniums at cooling rates greater than $\sim 1300^\circ\text{C/s}$ [137]. Annealing heat treatment resulted in a slight coarsening of the martensitic microstructure. Two stress relief heat treatments were applied at temperatures of 705C and 595C, with their microstructures shown in Figure 73(d) and (e). Stress relieving at 705 for 45 minutes had a negligible effect on the UTS, increasing to 975 MPa. The lower temperature (595C) stress relief decreased UTS to 927 MPa. The most significant strength effects were seen with a solution treating and aging which increased the UTS to 1049 MPa. Comparing the STA microstructure in Figure 73(c) to the other heat-treated microstructures, the greater thermal energy input associated with the STA HT had a clear impact on the resultant microstructure, with significant coarsening of the laths occurring. With regards to ductility, the as-built sample had a percent elongation of 2%, increasing only slightly with annealing (2% to 5%) and reaching a maximum of 5% with the high temperature (705C) stress relief. These ductility amounts are well below the textbook values for this material (12-15%), primarily due to the build direction resulting in the tensile force being applied perpendicular to the layers which results in layer delamination rather than bulk material fracture, which is a well understood phenomena in additively manufactured samples. [133]

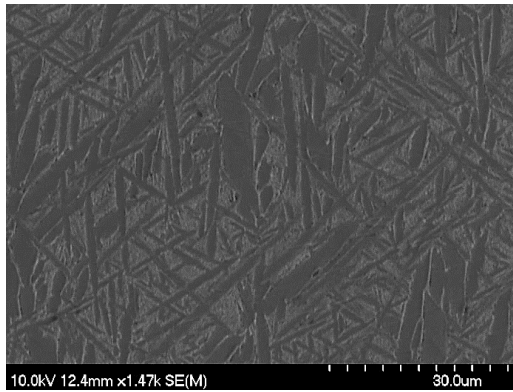
Table 14: Tensile properties of Ti-6242 bars fabricated in accordance with high density build parameters (DOE2) and select post-build heat treatments. Typical data for wrought counterpart shown for comparison purposes [138, 139].

	YS		E		UTS		% Ductility	
	Meas.	<i>Wrought</i>	Meas.	<i>Wrought</i>	Meas.	<i>Wrought</i>	Meas.	<i>Wrought</i>
As-Built	913 (+/- 33)	-	107 (+/- 2)	-	973 (+/- 2)	-	2 (+/- 2)	-
Annealed	913 (+/- 12)	910	103 (+/- 2)	-	970 (+/- 68)	1060	5 (+/- 1)	15
STA	1016 (+/- 39)	860	128 (+/- 2)	114	1049 (+/- 22)	940	4 (+/- 0.1)	15
SR-1	888 (+/- 85)	-	107 (+/- 1)	-	927 (+/- 47)	-	3 (+/- 2)	-
SR-2	905 (+/- 1)	-	118 (+/- 3)	-	975 (+/- 37)	-	5 (+/- 1)	-

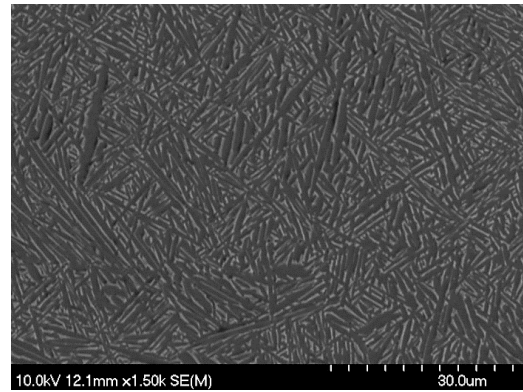


(a)

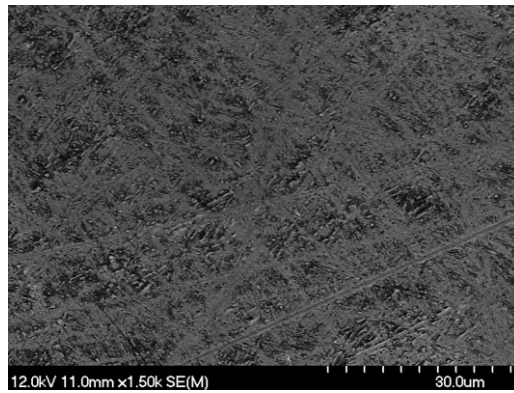
(b)



(c)



(d)



(e)

Figure 73: 1500x magnification SEM images of (a) As-built, (b) Annealed (900) (c) STA (970/595), (d) Stress relieved (595) and (e) Stress relieved (705) Ti-6242 samples.

4.4.3 DED Processing of Ti-6242 vs. Beta-21s

When examining the DED processing of each alloy, it is necessary to define criteria with which they can be compared. First and foremost, for a material to be feasible it must be possible to produce a highly dense product. Multiple parameter sets were identified for each alloy that produced samples with a density >99.8% of full theoretical, which suggested both alloys were successful in this regard. The scope of parameter sets for which such densities can be achieved is also worthy of consideration as a more expansive range implies an improved level of process robustness could be observed in commercial practice. Of the two alloys, Ti-6242 was more robust with 4 of the parameter sets producing greater than 99.8% dense samples. Comparatively, only 1 of the beta-21s parameter sets produced greater than 99.8%.

Beyond sample density, another consideration that was not quantified was the need for process intervention after the build commenced. The primary factor that necessitated this was balling on the deposition nozzles. In this regard, Beta-21s required lower laser powers and performed better at higher traverse rates. This lessened nozzle balling and thereby lessened the net build time relative to that found possible with Ti-6242.

With regards to heat treatment and mechanical properties, both alloys responded favorably to heat treatment, approaching, or exceeding wrought tensile strengths. However, with the exception of STA2 for Beta-21s (10% elongation) which exceeded wrought (6% elongation), both materials were well below wrought ductility as is typical of AM processes. With the success of AM produced parts depending on so many variables, it was not possible to conclusively determine whether Ti-6242 or Beta-21s was a clearly better candidate for DED processing. However, both alloys responded well enough to suggest that with appropriate processing parameters that either alloy could be feasible for commercial DED operations.

4.5 Conclusions

In this study the response of two titanium alloy powders to laser DED processing was investigated. Multi-stage DOEs were applied to each alloy wherein the effects of key processing parameters was considered and evaluated in a statistical manner. As a result of these efforts the following conclusions have been reached:

1. The two alloys of interest (Beta 21S and Ti-6242) responded favorably to DED processing in that nominally full density products (>99.8% of theoretical) could be fabricated when appropriate combinations of process parameters were utilized.
2. Ti-6242 was potentially more robust to DED processing than Beta 21S as a larger number of parameter sets produced samples of a nominally full density.
3. Tensile bars built in the z-axis orientation demonstrated that both alloys maintained as-built properties that included a relatively high yield strength and UTS coupled with limited ductility to fracture.
4. Post-build heat treatments were an effective means of adjusting the tensile properties of both alloys.
5. Application of the solution treating and aging (STA-2) sequence to Beta-21s was a particularly effective heat treatment as the product demonstrated tensile properties that exceeded typical values for the wrought counterpart.

4.6 Acknowledgements

The authors would like to graciously acknowledge the funding support provided by the Natural Sciences and Engineering Research Council of Canada (NSERC) strategic partnerships grant for networks entitled “NSERC Network for Holistic Innovation in Additive Manufacturing (HI-AM)”.

5 SUMMARY AND CONCLUSIONS

This research successfully quantified the variation in dimensional accuracy, density, hardness, and mechanical properties caused by differences in DED equipment. OEM DED equipment vendors were provided with portions of a single commercial lot of Ti-64 powder and advised to produce a dimensionally accurate, fully dense builds including several geometries as well as horizontally and vertically built tensile samples. Samples were measured and compared in terms of dimensional accuracy (3D coordinate measurement machine), hardness, density (infiltrated Archimedes approach), microstructure (scanning electron microscopy), tensile properties, fracture surfaces, and thermal behavior (differential scanning calorimetry).

Additionally, a near-alpha titanium (Ti-6242), and a beta titanium alloy (Beta-21s) that have industrial relevance were examined for their feasibility of being processed using DED. Following initial experimentation to ensure buildability, key process parameters (laser power and traverse rate) were varied strategically to narrow down the optimal ranges. With these ranges determined, several process parameters were added to the statistical model (hatch spacing, layer height and powder feed rate) to further improve density and identify the robustness of the process. The successful parameter set offering the greatest balance of density, dimensional accuracy, and buildability was chosen to produce tensile samples. Industrial heat treatments were applied to these samples and tensile properties were acquired.

5.1 Inter-vendor variation of DED processed Ti-64

Based on the analysis of the three builds provided by the vendors, there was considerable variation in the dimensional accuracies achieved, with no vendors successfully reproducing the 2mm diameter center cylinder or the 0.5 mm wall thickness concentric ring. Vendor C was the most dimensionally accurate. Vendors B and C were able to produce high density samples in the horizontal and vertically built directions, whereas vendor A showed

considerably lower vertically built density due to interlayer lack of fusion and residual gas-induced porosity. Hardness was comparable between vendors, with horizontally built samples showing consistently higher hardness than vertically built. Microstructures were as-expected consisting of martensitic (acicular/plate-like alpha-titanium). Vertically built samples had lower tensile properties across the board due to layer delamination, where-as horizontally built samples were near-wrought with the exception of ductility which was considerably lower than wrought in all samples. The DSC curves showed thermal stability when exposed to reheating up to 1200°C.

Throughout the paper, vendor names were hidden due to the nature of conference proceedings. Vendors A, B and C were DM3D Technology, BeAM, and RPM innovations respectively. Although the vendors did not provide details regarding the specific process parameters chosen, there are several fundamental differences in the manufacturing process that should be noted. The difference that seemed to have the most significant effect on build performance was the choice between motion occurring in the deposition head or the deposition head remaining stationary above a moving trunnion. BeAM and RPM innovations both utilize a stationary deposition head, whereas DM3D opts for a deposition head mounted to a 5-axis robotic arm. Based on the dimensional accuracy and mechanical property measurements, it appears as though the stationary deposition head resulted in improved dimensional accuracy, surface finish and mechanical properties compared to the robotic arm. That being said, there are advantages that were not captured in the scope of this experiment, namely the larger build volume due to freedom of movement associated with the robotic arm. Robotic arms also offer the ability to produce part geometries not achievable using a stationary deposition head, and can be more easily manipulated around existing components for repair or feature addition.

5.2 Feasibility of Ti-6242 and Beta-21s for DED processing

Ti-6242 and Beta-21s were both successfully processed using DED, producing fully dense samples (>99.9% of theoretical density) with high dimensional accuracy, considering the near-net shape nature of directed energy deposition often incorporating post-process

machining when tight tolerances are required. Several issues were identified irrespective of alloy, namely balling of powder on the deposition nozzles and failed initial layer adhesion resulting from excessive z-offset. Balling was minimized when laser powers were kept as low as (<500W), traverse rates were kept relatively high (>10 mm/s), and layer heights were high enough to minimize overbuilding (>0.25 mm). Issues related to the z-offset were experienced at low z-offset values particularly when using thicker (~0.5 in) substrates. Due to the increased heat dissipation, lower z-offsets were necessary to ensure adequate heat input when initially forming the melt pool. With inadequate melt pool formation, the early layers would fail to adhere to one another and causing significant lack-of-adhesion porosity within the final sample. Both samples responded to their corresponding industrial heat treatments as expected, showing similar tensile strength gains to wrought samples. However, both alloys had decreased ductility resulting from the chosen tensile sample build orientation.

Both Ti-6242 and Beta-21s showed promising results in terms of their feasibility of being processed using DED and would make excellent candidates for further research into part specific heat treatments, parameter optimization, and build orientation experimentation in order to use DED processing to supplement traditional manufacturing in terms of near-net-shape part production, repair of complex components and reduction of waste material for near-alpha and beta titanium parts.

5.3 Future Works

Several other studies were not explored due to time constraints. Recommendations for further research that would be beneficial to the overall understanding of DED processing of titanium alloys are as follows:

1. Comparing Ti-64, Ti-6242 and Beta-21s samples produced under closed atmosphere to those produced using a shielding gas in terms of O/N analysis and mechanical properties (tensile and hardness)

2. Electron back scatter diffraction (EBSD) as a means of further quantifying microstructural and crystallographic information, identifying any DED-specific texture.
3. Determination of optimal heat treatment parameters for achieving ideal mechanical properties from additively manufactured samples, as opposed to implementing common industrial heat treatments, taking into consideration the unique rapid solidification present in AM processing.
4. Experimenting with the build constraints for each alloy in terms of maximum overhang, surface roughness, wall thicknesses, hole features, and minimum radii using different sample geometries.
5. Exploring the effect of automatically varying process parameters throughout the build process through in-situ monitoring as a means of achieving consistently high densities in less controlled environments
6. Development of computational model to predict mechanical behavior based on inputted process parameters for both alloys

REFERENCES

- [1] Svelto O. (2010) "Principles of Lasers". Springer, Boston, MA. https://doi.org/10.1007/978-1-4419-1302-9_1
- [2] Gould, R. (1959). "The LASER, Light Amplification by Stimulated Emission of Radiation". In Franken, P.A.; Sands R.H. (Eds.). The Ann Arbor Conference on Optical Pumping, the University of Michigan, 15 June through 18 June 1959. p. 128. OCLC 02460155
- [3] Edwards, T. (2011). "How A Laser Works". Physics 212, University of Alaska Fairbanks. http://ffden-2.phys.uaf.edu/212_spring2011.web.dir/Thomas_Edwards/How%20Lasers%20Work.html
- [4] Hecht, J. (1999). "Laser Guidebook, Second Edition". Ch. 22, Blue Ridge Summit, PA
- [5] Geusic, J. E., Marcos, H. M., and Van Uitert, L. G. (1964). "Laser Oscillations in Nd-DOPED Yttrium Aluminum, Yttrium Gallium and Gadolinium Garnets", Applied Physics Letters, vol. 4, no. 10, pp. 182–184. doi:10.1063/1.1753928.
- [6] Koechner, W. (2006). "Solid-State Laser Engineering". p. 376 Springer, New York, NY.
- [7] Gujba, Abdullahi K., and Mamoun Medraj. (2014). "Laser Peening Process and Its Impact on Materials Properties in Comparison with Shot Peening and Ultrasonic Impact Peening" Materials 7, no. 12: 7925-7974. <https://doi.org/10.3390/ma7127925>
- [8] Dinesh Babu, P., Balasubramanian, K.R., Buvanashakaran, G. (2011). "Laser Surface Hardening: A Review". International Journal of Surface Science and Engineering, 5:2-3, 131-151
- [9] Gibson, I., Rosen, D., & Stucker, B. (2015). Directed energy deposition processes. In Additive manufacturing technologies (pp. 245-268). Springer, New York, NY.
- [10] Kruth, J. P., Wang, X., Laoui, T., & Froyen, L. (2003). Lasers and materials in selective laser sintering. Assembly Automation.
- [11] Yap, C. Y., Chua, C. K., Dong, Z. L., Liu, Z. H., Zhang, D. Q., Loh, L. E., & Sing, S. L. (2015). Review of selective laser melting: Materials and applications. Applied physics reviews, 2(4), 041101.
- [12] Barcikowski, S., Amendola, V., Lau, M., Marzun, G., Rehbock, C., Reichenberger, S., ... & Gökce, B. (2019). Handbook of laser synthesis and processing of colloids.
- [13] Cantor, B., O'Reilly, K. (2003) Solidification and Casting. IOP

- [14] Sahoo, C. K., Mallick, S., Kumar, K., & Masanta, M. (2021). Pulse laser welding of high carbon alloy steel: assessment of melt pool geometry and mechanical performance. *Sādhanā*, 46(1), 1-8.
- [15] Hong, K. M., & Shin, Y. C. (2017). Prospects of laser welding technology in the automotive industry: A review. *Journal of Materials Processing Technology*, 245, 46-69.
- [16] Cvecek, K., Dehmel, S., Miyamoto, I., & Schmidt, M. (2019). A review on glass welding by ultra-short laser pulses. *International Journal of Extreme Manufacturing*, 1(4), 042001.
- [17] Specifications, S. W. P. (2011). *ASM handbook, volume 6A: welding fundamentals and processes*.
- [18] E. Assuncao, S. Williams, Comparison of continuous wave and pulsed wave laser welding effects, *Opt. Lasers Eng.* 51 (6) (2013) 674–680.
- [19] Sipes, D. L. (1985). Highly efficient neodymium: yttrium aluminum garnet laser end pumped by a semiconductor laser array. *Applied Physics Letters*, 47(2), 74-76.
- [20] Quintino, L., & Assuncao, E. (2013). Conduction laser welding. In *Handbook of laser welding technologies* (pp. 139-162). Woodhead Publishing.
- [21] Negrutiu, M. L., Sinescu, C., Cozarov, D., Culea, L., Rominu, M., & Pop, D. M. (2008, February). Repairing method of fixed partial prostheses in dentistry: laser welding. In *Lasers in Dentistry XIV* (Vol. 6843, pp. 54-61). SPIE.
- [22] Ai, Y., Jiang, P., Shao, X., Li, P., Wang, C., Mi, G., ... & Liu, W. (2017). The prediction of the whole weld in fiber laser keyhole welding based on numerical simulation. *Applied Thermal Engineering*, 113, 980-993.
- [23] Lyon, S., Richardson, T., Cottis, B., Lindsay, R., Scantlebury, D., Stott, H., & Graham, M. (2010). *Shreir's Corrosion*.
- [24] Vilar, R. (1999). Laser cladding. *Journal of laser applications*, 11(2), 64-79.
- [25] Kumar, S., & Mandal, A. (2021). Laser Cladding of Titanium Alloy. In *Laser Cladding of Metals* (pp. 215-242). Springer, Cham.
- [26] Wang, W., Wang, M., Jie, Z., Sun, F., & Huang, D. (2008). Research on the microstructure and wear resistance of titanium alloy structural members repaired by laser cladding. *Optics and Lasers in Engineering*, 46(11), 810-816.

- [27] Al-Sayed Ali, S. R., Hussein, A. H. A., Nofal, A. A. M. S., Hasseb Elnaby, S. E. I., Elgazzar, H. A., & Sabour, H. A. (2017). Laser powder cladding of Ti-6Al-4V α/β alloy. *Materials*, 10(10), 1178.
- [28] Han, G., & Zhang, Y. (2021). Microstructure and Corrosion of Laser Cladding Coatings on Titanium Alloy With Nd₂O₃. *Journal of Engineering Materials and Technology*, 143(1).
- [29] Ye, F., Shao, W., Ye, X., Liu, M., Xie, Y., Bian, P., ... & Wu, H. (2020). Microstructure and Corrosion Behavior of Laser-Cladding CeO₂-Doped Ni-Based Composite Coatings on TC4. *Journal of Chemistry*
- [30] ASTM F2792-12a. (2012). *Standard Terminology for Additive Manufacturing Technologies*, ASTM International, West Conshohocken, PA
- [31] Gibson, I., Rosen, D., & Stucker, B. (2015). Design for additive manufacturing. In *Additive Manufacturing Technologies* (pp. 399-435). Springer, New York, NY.
- [32] Gibson, I., Rosen, D., Stucker, B., & Khorasani, M. (2021). Materials for additive manufacturing. In *Additive Manufacturing Technologies* (pp. 379-428). Springer, Cham.
- [33] Business Wire. (2017). *3D Printing Market (2017-2022): Analysis by Material, Printer, Form, Industry Vehicle, Application and Geography*. Research and Markets.
- [34] ASTM F3187-16. (2016). *Standard Guide for Directed Energy Deposition of Metals*, ASTM International, West Conshohocken, PA.
- [35] Tang, Z. J., Liu, W. W., Wang, Y. W., Saleheen, K. M., Liu, Z. C., Peng, S. T., ... & Zhang, H. C. (2020). A review on in situ monitoring technology for directed energy deposition of metals. *The International Journal of Advanced Manufacturing Technology*, 108(11), 3437-3463.
- [36] Cunningham, C. R., Flynn, J. M., Shokrani, A., Dhokia, V., & Newman, S. T. (2018). Invited review article: Strategies and processes for high quality wire arc additive manufacturing. *Additive Manufacturing*, 22, 672-686.
- [37] Xiang, S., & Altintas, Y. (2016). Modeling and compensation of volumetric errors for five-axis machine tools. *International Journal of Machine Tools and Manufacture*, 101, 65-78.
- [38] Peng, X., Kong, L., Fuh, J. Y. H., & Wang, H. (2021). A review of post-processing technologies in additive manufacturing. *Journal of Manufacturing and Materials Processing*, 5(2), 38. Hybrid DED
- [39] Stavropoulos, P., Souflas, T., & Bikas, H. (2021). Hybrid manufacturing processes: an experimental machinability investigation of DED produced parts. *Procedia CIRP*, 101, 218-221.

- [40] Singh, D. D., Arjula, S., & Reddy, A. R. (2021). Functionally Graded Materials Manufactured by Direct Energy Deposition: A review. *Materials Today: Proceedings*, 47, 2450-2456.
- [41] Mosallanejad, M. H., Niroumand, B., Aversa, A., & Saboori, A. (2021). In-situ alloying in laser-based additive manufacturing processes: A critical review. *Journal of Alloys and Compounds*, 872, 159567.
- [42] Articek, U., Milfelner, M., & Anzel, I. (2013). Synthesis of functionally graded material H13/Cu by LENS technology. *Advances in Production Engineering & Management*, 8(3).
- [43] Wang, H., Gould, B., Parab, N., Zhao, C., Greco, A., Sun, T., & Wolff, S. J. (2021). High-speed synchrotron X-ray imaging of directed energy deposition of titanium: effects of processing parameters on the formation of entrapped-gas pores. *Procedia Manufacturing*, 53, 148-154.
- [44] D'Andrea Jr, M. M. (1966). SOURCES AND CAUSES OF POROSITY IN TITANIUM ARC WELDS. ARMY MATERIALS RESEARCH AGENCY WATERTOWN MASS MATERIALS TECHNOLOGY DIV.
- [45] Huang, J. L., Warnken, N., Gebelin, J. C., Strangwood, M., & Reed, R. C. (2012). On the mechanism of porosity formation during welding of titanium alloys. *Acta Materialia*, 60(6-7), 3215-3225.
- [46] Sola, A., & Nouri, A. (2019). Microstructural porosity in additive manufacturing: The formation and detection of pores in metal parts fabricated by powder bed fusion. *Journal of Advanced Manufacturing and Processing*, 1(3), e10021.
- [47] Wang, W., Ning, J., & Liang, S. Y. (2021). Prediction of lack-of-fusion porosity in laser powder-bed fusion considering boundary conditions and sensitivity to laser power absorption. *The International Journal of Advanced Manufacturing Technology*, 112(1), 61-70.
- [48] Zhong, C., Gasser, A., Schopphoven, T., & Poprawe, R. (2015). Experimental study of porosity reduction in high deposition-rate Laser Material Deposition. *Optics & Laser Technology*, 75, 87-92.
- [49] Brown, C. U., Brown, C. U., Jacob, G., Possolo, A., Beauchamp, C., Peltz, M., ... & Donmez, A. (2018). The effects of laser powder bed fusion process parameters on material hardness and density for nickel alloy 625. US Department of Commerce, National Institute of Standards and Technology.
- [50] Zhang, Y., Jing, H., Xu, L., Han, Y., & Zhao, L. (2021). Effects of different scanning patterns on nickel alloy-directed energy deposition based on thermal analysis. *Virtual and Physical Prototyping*, 16(sup1), S98-S115.

- [51] Dimter, M., Mayer, R., Hümmeler, L., Salzberger, R., Kotila, J., & Syvänen, T. (2011). U.S. Patent No. 8,034,279. Washington, DC: U.S. Patent and Trademark Office.
- [52] Cloots, M., Spierings, A. B., & Wegener, K. (2013, August). Assessing new support minimizing strategies for the additive manufacturing technology SLM. In 2013 International Solid Freeform Fabrication Symposium. University of Texas at Austin.
- [53] Malev, M. D. (1973). Gas absorption and outgassing of metals. *Vacuum*, 23(2), 43-50.
- [54] Robino, C. V. (1999). A Glove Box Enclosed Gas-Tungsten Arc Welding System (No. SAND99-1648). Sandia National Lab.(SNL-NM), Albuquerque, NM (United States); Sandia National Lab.(SNL-CA), Livermore, CA (United States).
- [55] AM Chronicle. (2019). Optomec Announces new LENS CS 600 and CS 800 Controlled Atmosphere DED Systems. <https://www.amchronicle.com/news/optomec-unveils-two-new-lens-cs-600-and-cs-800-systems/>
- [56] Trumpf Group (2022). Laser Metal Deposition. https://www.trumpf.com/en_CN/newsroom/stories/how-does-lmd-with-powder-actually-work/
- [57] Juliano, P., & Barbosa-Cánovas, G. V. (2010). Food powders flowability characterization: theory, methods, and applications. *Annual review of food science and technology*, 1, 211-239.
- [58] ASTM B213-17. (2017). Standard test methods for flow rate of metal powders using the hall flowmeter funnel. *ASTM Int*, 1-4.
- [59] AimSizer. (2021). AS-300 Hall Flowmeter. http://www.aimsizer.com/as_300_hall_flow_meter_overview.html
- [60] Boyer, R. R. (1996). An overview on the use of titanium in the aerospace industry. *Materials Science and Engineering: A*, 213(1-2), 103-114.
- [61] Froes, F. H., Friedrich, H., Kiese, J., & Bergoint, D. (2004). Titanium in the family automobile: the cost challenge. *Jom*, 56(2), 40-44.
- [62] Ratner, B. D. (2001). A perspective on titanium biocompatibility. In *Titanium in medicine* (pp. 1-12). Springer, Berlin, Heidelberg.
- [63] Kopeliovich, D. (2012). Metals Crystal Structure. https://www.substech.com/dokuwiki/doku.php?id=metals_crystal_structure

- [64] Sinha, A., Sanyal, S., Bandyopadhyay N.R. (2017). Thermal Treatment for Strengthening Titanium Alloys, *Comprehensive Materials Finishing*, Elsevier, Pages 288-336, ISBN 9780128032497, <https://doi.org/10.1016/B978-0-12-803581-8.09193-1>
- [65] Welsch, G., Boyer, R., & Collings, E. W. (Eds.). (1993). *Materials properties handbook: titanium alloys*. ASM international.
- [66] Ahmed, T., & Rack, H. J. (1998). Phase transformations during cooling in $\alpha + \beta$ titanium alloys. *Materials Science and Engineering: A*, 243(1-2), 206-211.
- [67] Rajan, S. (2020). *Analysis of Microstructure Evolution and Mechanical Properties of Linear Friction Welded Titanium alloys* (Doctoral dissertation, Carleton University).
- [68] Shamblen, C. E., & Redden, T. K. (1972). Creep resistance and high-temperature metallurgical stability of titanium alloys containing gallium. *Metallurgical Transactions*, 3(5), 1299-1305.
- [69] Soyama, J., Oehring, M., Limberg, W., Ebel, T., Kainer, K. U., & Pyczak, F. (2015). The effect of zirconium addition on sintering behaviour, microstructure and creep resistance of the powder metallurgy processed alloy Ti-45Al-5Nb-0.2 B-0.2 C. *Materials & Design*, 84, 87-94.
- [70] Jaffe, L. D. (1955). Hardenability of titanium alloys calculated from composition: A preliminary examination. *JOM*, 7(11), 1245-1249.
- [71] Robertson, I. M., & Schaffer, G. B. (2009). Suitability of nickel as alloying element in titanium sintered in solid state. *Powder metallurgy*, 52(3), 225-232.
- [72] Cotton, J. B. (1967). The role of palladium in enhancing corrosion resistance of titanium. *Platinum Metals Review*, 11(2), 50-52.
- [73] Dyer, J. P. (2003). *Evaluation of preventative solutions for fretting fatigue damage of Ti-6242 in aircraft engines* (Doctoral dissertation, Carleton University).
- [74] Boyer, R. R., & Briggs, R. D. (2005). The use of β titanium alloys in the aerospace industry. *Journal of Materials Engineering and Performance*, 14(6), 681-685.
- [75] Donachie, M. J. (2000). *Titanium: a technical guide*. ASM international.
- [76] O'Leary, R., Setchi, R., Prickett, P., & Hankins, G. (2016). An investigation into the recycling of Ti-6Al-4V powder used within SLM to improve sustainability. *InImpact: The Journal of Innovation Impact*, 8(2), 377.
- [77] Najmon, J. C., Raeisi, S., & Tovar, A. (2019). Review of additive manufacturing technologies and applications in the aerospace industry. *Additive manufacturing for the aerospace industry*, 7-31.

- [78] Bose, S., Robertson, S. F., & Bandyopadhyay, A. (2018). Surface modification of biomaterials and biomedical devices using additive manufacturing. *Acta biomaterialia*, 66, 6-22.
- [79] Meena, V. K., Kumar, P., Kalra, P., & Sinha, R. K. (2021). Additive manufacturing for metallic spinal implants: A systematic review. *Annals of 3D Printed Medicine*, 3, 100021.
- [80] Heigel, J. C., Michaleris, P., & Reutzel, E. W. (2015). Thermo-mechanical model development and validation of directed energy deposition additive manufacturing of Ti-6Al-4V. *Additive manufacturing*, 5, 9-19.
- [81] Carroll, B. E., Palmer, T. A., & Beese, A. M. (2015). Anisotropic tensile behavior of Ti-6Al-4V components fabricated with directed energy deposition additive manufacturing. *Acta Materialia*, 87, 309-320.
- [82] Hayes, Brian J., Brian W. Martin, Brian Welk, Samuel J. Kuhr, Thomas K. Ales, David A. Brice, Iman Ghamarian et al. "Predicting tensile properties of Ti-6Al-4V produced via directed energy deposition." *Acta Materialia* 133 (2017): 120-133.
- [83] Kistler, N. A., Corbin, D. J., Nassar, A. R., Reutzel, E. W., & Beese, A. M. (2019). Effect of processing conditions on the microstructure, porosity, and mechanical properties of Ti-6Al-4V repair fabricated by directed energy deposition. *Journal of Materials Processing Technology*, 264, 172-181.
- [84] Tan, H., Guo, M., Clare, A. T., Lin, X., Chen, J., & Huang, W. (2019). Microstructure and properties of Ti-6Al-4V fabricated by low-power pulsed laser directed energy deposition. *Journal of Materials Science & Technology*, 35(9), 2027-2037.
- [85] Razavi, S. M. J., & Berto, F. (2019). Directed energy deposition versus wrought Ti-6Al-4V: a comparison of microstructure, fatigue behavior, and notch sensitivity. *Advanced Engineering Materials*, 21(8), 1900220.
- [86] Zhao, X., Li, S., Zhang, M., Liu, Y., Sercombe, T. B., Wang, S., ... & Murr, L. E. (2016). Comparison of the microstructures and mechanical properties of Ti-6Al-4V fabricated by selective laser melting and electron beam melting. *Materials & Design*, 95, 21-31.
- [87] Thijs, L., Verhaeghe, F., Craeghs, T., Van Humbeeck, J., & Kruth, J. P. (2010). A study of the microstructural evolution during selective laser melting of Ti-6Al-4V. *Acta materialia*, 58(9), 3303-3312.
- [88] Vilaro, T., Colin, C., & Bartout, J. D. (2011). As-fabricated and heat-treated microstructures of the Ti-6Al-4V alloy processed by selective laser melting. *Metallurgical and materials transactions A*, 42(10), 3190-3199.

- [89] Ahn, D. G. (2021). Directed energy deposition (DED) process: State of the art. *International Journal of Precision Engineering and Manufacturing-Green Technology*, 8(2), 703-742.
- [90] Plourde, R. (2004). Laser-based repair system reclaims high value military components. Optomec Design Co., Albuquerque, NM.
- [91] Saboori, A., Aversa, A., Marchese, G., Biamino, S., Lombardi, M., & Fino, P. (2019). Application of directed energy deposition-based additive manufacturing in repair. *Applied Sciences*, 9(16), 3316.
- [92] Blakey-Milner, B., Gradl, P., Snedden, G., Brooks, M., Pitot, J., Lopez, E., ... & du Plessis, A. (2021). Metal additive manufacturing in aerospace: A review. *Materials & Design*, 209, 110008.
- [93] Jariwala, S. H., Lewis, G. S., Bushman, Z. J., Adair, J. H., & Donahue, H. J. (2015). 3D printing of personalized artificial bone scaffolds. *3D printing and additive manufacturing*, 2(2), 56-64.
- [94] Hao, Y. L., Li, S. J., & Yang, R. (2016). Biomedical titanium alloys and their additive manufacturing. *Rare Metals*, 35(9), 661-671.
- [95] Łyczkowska, E., Szymczyk, P., Dybała, B., & Chlebus, E. (2014). Chemical polishing of scaffolds made of Ti-6Al-7Nb alloy by additive manufacturing. *Archives of Civil and Mechanical Engineering*, 14(4), 586-594.
- [96] Abate, K. M., Nazir, A., Jeng, J. Y., Abate, K. M., Nazir, A., & Jeng, J. Y. (2020). A Short Review on Cellular Structure Design and Selective Laser Melting using Bio-compatible Ti6Al4V Material. *Biomedical Journal of Scientific & Technical Research*, 27(1), 20519-20523.
- [97] Speirs, M., Humbeeck, J. V., Schrooten, J., Luyten, J., & Kruth, J. P. (2013). The effect of pore geometry on the mechanical properties of selective laser melted Ti-13Nb-13Zr scaffolds. *Procedia Cirp*, 5, 79-82.
- [98] Zhu, Y., Tian, X., Li, J., & Wang, H. (2015). The anisotropy of laser melting deposition additive manufacturing Ti-6.5 Al-3.5 Mo-1.5 Zr-0.3 Si titanium alloy. *Materials & Design*, 67, 538-542.
- [99] Ahmed, F. F. (2020). Development of an In-Situ Alloyed Microstructure in Laser Additive Manufacturing (Doctoral dissertation).
- [100] Saboori, A., Gallo, D., Biamino, S., Fino, P., & Lombardi, M. (2017). An overview of additive manufacturing of titanium components by directed energy deposition: microstructure and mechanical properties. *Applied Sciences*, 7(9), 883.

- [101] Hernandez, J., Li, S. J., Martinez, E., Murr, L. E., Pan, X. M., Amato, K. N., ... & Wicker, R. B. (2013). Microstructures and hardness properties for β -phase Ti-24Nb-4Zr-7.9 Sn alloy fabricated by electron beam melting. *Journal of Materials Science & Technology*, 29(11), 1011-1017.
- [102] Bermingham, M. J., Kent, D., Pace, B., Cairney, J. M., & Dargusch, M. S. (2020). High strength heat-treatable β -titanium alloy for additive manufacturing. *Materials Science and Engineering: A*, 791, 139646.
- [103] Shen, S., Wang, H., He, B., & Zhang, S. (2022). Microstructure Evolution and Phase Transformation Behavior of Ti17 and γ -TiAl Bimetallic Structure Fabricated by Directed Energy Deposition. *Journal of Alloys and Compounds*, 164571.
- [104] Lin, Z., Song, K., & Yu, X. (2021). A review on wire and arc additive manufacturing of titanium alloy. *Journal of Manufacturing Processes*, 70, 24-45.
- [105] Cai, C., Wu, X., Liu, W., Zhu, W., Chen, H., Qiu, J. C. D., ... & Shi, Y. (2020). Selective laser melting of near- α titanium alloy Ti-6Al-2Zr-1Mo-1V: Parameter optimization, heat treatment and mechanical performance. *Journal of Materials Science & Technology*, 57, 51-64.
- [106] Fan, H., & Yang, S. (2020). Effects of direct aging on near-alpha Ti-6Al-2Sn-4Zr-2Mo (Ti-6242) titanium alloy fabricated by selective laser melting (SLM). *Materials Science and Engineering: A*, 788, 139533.
- [107] Atwood, C., Griffith, M., Harwell, L., Schlienger, E., Ensz, M., Smugeresky, J., ... & Reckaway, D. (1998, November). Laser engineered net shaping (LENSTM): A tool for direct fabrication of metal parts. In *International congress on applications of lasers & electro-optics (Vol. 1998, No. 1, pp. E1-E7)*. Laser Institute of America.
- [108] Gibson, I., Rosen, D. W., Stucker, B., Khorasani, M., Rosen, D., Stucker, B., & Khorasani, M. (2021). *Additive manufacturing technologies (Vol. 17)*. Cham, Switzerland: Springer
- [109] Welsch, G., Boyer, R., & Collings, E. W. (Eds.). (1993). *Materials properties handbook: titanium alloys*. ASM international.
- [110] Peters, M., Kumpfert, J., Ward, C. H., & Leyens, C. (2003). Titanium alloys for aerospace applications. *Advanced engineering materials*, 5(6), 419-427.
- [111] Huang, S. H., Liu, P., Mokasdar, A., & Hou, L. (2013). Additive manufacturing and its societal impact: a literature review. *The International Journal of Advanced Manufacturing Technology*, 67(5), 1191-1203.

- [112] Walter, A., & Marcham, C. L. (2020). Environmental Advantages in Additive Manufacturing. *Professional Safety*, 65(01), 34-38.
- [113] Ezugwu, E. O., & Wang, Z. M. (1997). Titanium alloys and their machinability—a review. *Journal of materials processing technology*, 68(3), 262-274.
- [114] Martina, F., Colegrove, P. A., Williams, S. W., & Meyer, J. (2015). Microstructure of interpass rolled wire+ arc additive manufacturing Ti-6Al-4V components. *Metallurgical and Materials Transactions A*, 46(12), 6103-6118.
- [115] Saboori, A., Aversa, A., Marchese, G., Biamino, S., Lombardi, M., & Fino, P. (2019). Application of directed energy deposition-based additive manufacturing in repair. *Applied Sciences*, 9(16), 3316.
- [116] Welsch, G., Boyer, R., & Collings, E. W. (Eds.). (1993). *Materials properties handbook: titanium alloys*. ASM international.
- [117] Miracle, D. B., Donaldson, S. L., Henry, S. D., Moosbrugger, C., Anton, G. J., Sanders, B. R., ... & Scott Jr, W. W. (2001). *ASM handbook* (Vol. 21, pp. 107-119). Materials Park, OH: ASM international.
- [118] SAE International. (2019) "Titanium Alloy, High Temperature Applications, Powder for Additive Manufacturing, Ti - 6.0Al - 2.0Sn - 4.0Zr - 2.0Mo.", doi: 10.4271/ams7014.
- [119] Fan, H., & Yang, S. (2020). Effects of direct aging on near-alpha Ti-6Al-2Sn-4Zr-2Mo (Ti-6242) titanium alloy fabricated by selective laser melting (SLM). *Materials Science and Engineering: A*, 788, 139533.
- [120] Zhu, Z., Ng, F. L., Seet, H. L., & Nai, S. M. L. (2022). Tailoring the microstructure and mechanical property of laser powder bed fusion fabricated Ti-6Al-2Sn-4Zr-2Mo via heat treatment. *Journal of Alloys and Compounds*, 895, 162648.
- [121] Richter, K. H., Orban, S., & Nowotny, S. (2004, October). Laser cladding of the titanium alloy Ti6242 to restore damaged blades. In *International Congress on Applications of Lasers & Electro-Optics* (Vol. 2004, No. 1, p. 1506). Laser Institute of America.
- [122] Soundararajan, S. R., Vishnu, J., Manivasagam, G., & Muktinutalapati, N. R. (2018). Processing of beta titanium alloys for aerospace and biomedical applications. In *Titanium Alloys-Novel Aspects of Their Manufacturing and Processing*. IntechOpen.
- [123] Pellizzari, M., Jam, A., Tonon, V., Benedetti, M., & Lora, C. (2021). Ageing behavior of Beta-Ti21S produced by laser powder bed fusion. *La Metallurgia Italiana*, 42.

- [124] Macias-Sifuentes, M. A., Xu, C., Sanchez-Mata, O., Kwon, S. Y., Atabay, S. E., Muñoz-Lerma, J. A., & Brochu, M. (2021). Microstructure and mechanical properties of β -21S Ti alloy fabricated through laser powder bed fusion. *Progress in Additive Manufacturing*, 6(3), 417-430.
- [125] Yannetta, C. J. (2017). Additive Manufacturing of Metastable Beta Titanium Alloys. Masters Thesis, 4
- [126] ASM International. (1994). "Ti-6Al-2Sn-4Zr-2Mo-0.08Si", *Materials Properties Handbook: Titanium Alloys*, 337
- [127] ASM International. (1994). "TIMETAL 21s", *Materials Properties Handbook: Titanium Alloys*, 922
- [128] Metal Powder Industries Federation. (2019). "MPIF Standard 03 – Method for Determination of Flow Rate of Free-Flowing Metal Powders Using the Hall Apparatus"
- [129] Metal Powder Industries Federation. (2019). "MPIF Standard 48 – Method for Determination of Apparent Density of Metal Powders Using the Arnold Meter"
- [130] Metal Powder Industries Federation. (2019). "MPIF Standard 42 – Method for Determination of Density of Compacted or Sintered Powder Metallurgy Products"
- [131] ASTM International. (2018). "ASTM standard E8/E8M-21 – Standard Test Methods for Tension Testing of Metallic Materials"
- [132] Lewandowski, J. J., & Seifi, M. (2016). Metal additive manufacturing: a review of mechanical properties. *Annual review of materials research*, 46, 151-186.
- [133] TIMET. (2000). "TIMETAL 21S – High Strength, Oxidation Resistant Strip Alloy", <https://www.timet.com/assets/local/documents/datasheets/metastablebetaalloys/21S.pdf>
- [134] MatWeb Material Property Data. (2021). TIMET TIMETAL21S Titanium Alloy ST 843C + Aged at 538C"
- [135] Ulbrich Stainless Steels and Special Metals Inc., "Titanium Beta 21s UNS R58210", <https://www.ulbrich.com/alloys/ti-beta-21-s-uns-r58210/>
- [136] Donachie, M.J. (2000). "Titanium: A technical guide, 2nd ed.", ASM International, United States
- [137] GE Additive. (2021). "M2 Series 5 Titanium Ti-6242", 2021. https://www.ge.com/additive/sites/default/files/2021-04/M2SERIES5_Ti6242_CMDS_20210321.pdf

- [138] ASM International. (1990). "Metals Handbook, Vol.2 - Properties and Selection: Nonferrous Alloys and Special-Purpose Materials"